Centro de Investigación Científica y de Educación Superior de Ensenada, Baja California

Doctorado en Ciencias
Posgrado en Óptica
con orientación en Óptica Física

Photonic devices for a biomedical platform

Tesis

para cubrir parcialmente los requisitos necesarios para obtener el grado de

Doctor en Ciencias

Presenta:

Cecilia María Guerra Olvera

Ensenada, Baja California, México

2019

Tesis defendida por

Cecilia María Guerra Olvera

y aprobada por el siguiente Comité

Dr. Santiago Camacho López
Director de tesis

Dr. Anatoly Khomenko

Dr. Raúl Rangel Rojo

Dr. Guillermo Aguilar Mendoza

Dr. Israel Rocha Mendoza
Coordinador del Posgrado en Posgrado en Óptica

Dra. Rufina Hernández Martínez
Directora de Estudios de Posgrado

Resumen de la tesis que presenta Cecilia María Guerra Olvera como requisito parcial para la obtención del grado de Doctor en Ciencias en Posgrado en Óptica con orientación en Óptica Física.

Dispositivos fotónicos para una plataforma biomédica

Resumen aprobado por:

Dr. Santiago Camacho López

Director de tesis

En este trabajo se describen tres métodos para la inscripción de distintas configuraciones de guías de onda en cerámicas transparentes nc-YSZ. La fuente láser empleada fue un láser Yb de fibra (Satsuma HP2, Amplitude Systèmes) que produce pulsos de $400fs$ a una longitud de onda central de $1030nm$ y con frecuencia de repiteción variable. Distintos régimenes de frecuencias fueron seleccionados para cada tipo de guía de onda que fue escrita, demostrando que distintos mecanismos de interacción láser pueden llevar a la fabricación de guías de onda. La energía por pulso y la óptica necesaria para el procesamiento también fueron seleccionados cuidadosamente. Los resultados indican que las características de propagación de las guías de onda son altamente dependientes de varias condiciones tanto del material como del láser; éstas pueden ser vacancias de oxígeno inherentes de la cerámica y la tasa de repetición de los pulsos. Las propiedades ópticas de nc-YSZ y su relación con el origen de los mecanismos de la creación de guías de onda son discutidos. En el primer método, las muestras fueron irradiadas por arriba del umbral de ablación a $500kHz$ para crear dos canales paralelos de separación variable (10, 15, 20 y $30\mu m$). La luz es guiada entre cada par de canales, donde el material no ha sido modificado por interacción directa del láser de femto segundos. La caracterización óptica fue realizada a $633nm$, mostrando que el material no modificado por el láser presenta altas pérdidas, principalmente debido a esparcimiento. El segundo método consiste en irradiar la superficie de cerámicas transpatentes nc-YSZ a $1000kHz$ al escanear la muestra con respecto al rayo enfocado del láser. Para lograr una fabricación adecuada y las propiedades de guiado deseadas, varios escaneos deben realizarse sobre la misma área. Como consecuencia, se obtienen guías de onda planas en las que la luz es guiada por la region que fue modificada directamente con el láser de femto segundos. La caracterización óptica a 633 y a $810nm$, así como experimentos de recocido, develaron la resiliencia térmica que estas guías de onda poseen. El tercer método reporta la fabricación de guías de onda de *cladding* inscritas por irradiación directa de pulsos láser de femto segundos a $1kHz$ en cerámicas transparentes policristalinas nc-YSZ. Las guías de onda consisten en dos estructuras circulares distintas con diámetros de 30 y $100\mu m$ y de diferentes longitudes. La caracterización óptica se llevó a cabo a 633, 810 y $1568nm$. Los perfiles de los modos de propagación obtenidos muestran una dependencia con la estructura y el tamaño de las guías de onda. Se estima un contraste de índice de refracción de casi 10^{-2}, mayor a lo que puede ser explicado sólo con estrés residual inducido. La conjetura es que las interacciones con el láser conllevan a daño físico localizado (i.e. micro vacíos, rupturas y posiblemente un decremento del grado de cristalinidad) en las zonas procesadas con láser, lo cual es corroborado con mediciones de espectroscopía Raman. Los resultados sugieren el uso potencial de nc-YSZ en bio aplicaciones.

Adicionalmente, una técnica de inactivación total bacteriana por medio de irradiación directa con pulsos láser de femto segundos, que no requiere ningún agente externo, es demostrada. Pulsos láser de femto segundos, a una tasa de repetición de $89 MHz$, fueron utilizados para irradiar soluciones de agua destilada con una sepa silvestre de *E. coli* a una densidad $> 10^7 cell/ml$. Estos experimentos indican que las bacterias pueden ser inactivadas con fluencias por pulso tan bajas como $\sim 1 mJ/cm^2$.

Palabras clave: óptica, láser, materiales, bioaplicaciones, YSZ

Abstract of the thesis presented by Cecilia María Guerra Olvera as a partial requirement to obtain the Doctor of Science degree in Optics with orientation in Optics.

Photonic devices for a biomedical platform

Abstract approved by:

Dr. Santiago Camacho López
Thesis Director

In the present work, three different methods for inscribing different configurations of waveguides in transparent nanopolycrystalline yttria stabilized zirconia (nc-YSZ) ceramics are described. The laser source was an Ytterbium fiber laser (Satsuma HP2, Amplitude Systm̀es) producing 400 *femtosecond*-pulses at a central wavelength of 1030nm with variable repetition rate. A different laser frequency regime was selected for each type of waveguide being written, showing different mechanisms of laser interactions can lead to waveguides fabrication. The per pulse energy, and processing optics were also carefully selected. The present results indicate that waveguide propagation features are strongly dependent on several material and laser irradiation conditions, such as inherent oxygen vacancies in the nc-YSZ and pulse repetition rate, respectively. The optical properties of the nc-YSZ and its relation to the origin of the waveguide creation mechanisms are discussed. In the first method, samples were irradiated above the ablation threshold at 500kHz to create two parallel channels of varying separation (10μm, 15μm, 20μm, and 30μm). Light is guided in between every pair of channels where the material has not been modified by direct *femtosecond*-laser interaction. Optical characterization at 633nm was performed, showing that the unmodified material has high losses principally due to scattering. The second method consist in irradiating the surface of transparent nc-YSZ polycrystalline ceramics at 1000kHz by scanning the sample with respect to the focused laser beam. To achieve proper fabrication and the desired guiding features, several scans of the same area are needed. The outcome are planar waveguides in which light is guided by the direct *femtosecond*-laser modified region. Optical characterization at 633nm and 810nm, as well as annealing experiments, unveiled the unique thermal resilience these waveguides posses. The third method reports on the fabrication of depressed cladding waveguides inscribed by direct *femtosecond*-laser pulses irradiation at 1kHz in transparent nc-YSZ polycrystalline ceramics. The waveguides consisted of two different circular structures with diameters of 30μm and 100μm, and different lengths. Optical characterization at 633nm, 810nm, and 1568nm was performed. The obtained modal profiles show dependence on the structure and size of the waveguides. A laser-induced refractive index contrast (Δn) of nearly 10^{-2} is estimated, larger than can be explained by induced residual stresses alone. The conjecture is that laser interactions lead to localized physical damage (i.e. microvoids, cracks, and possibly a decreased degree of crystallinity) in the laser processed zones, which is supported by Raman measurements. The results suggest a promising potential use of nc-YSZ in photonic bio-applications. Additionally, a total bacterial inactivation technique by ultrashort pulse direct *femtosecond*-laser irradiation that does not require any external agent is demonstrated. Near-infrared *femtosecond*-laser pulses at 89MHz repetition rate were used to irradiate solutions of

distilled water with $> 10^7 cell/ml$ of a wild strain of *Escherichia coli* (E. coli), showing they can be inactivated with fluences per pulse as low as $\sim 1 mJ/cm^2$.

Keywords: optics, laser, materials, bioapplications, YSZ

Dedication

A mi madre.

Acknowledgements

Al Centro de Investigación Científica y de Educación Superior de Ensenada por haberme dado la oportunidad de realizar mis estudios de doctorado.

Al Consejo Nacional de Ciencia y Tecnología (CONACyT) por brindarme el apoyo económico para realizar mis estudios de doctorado. No. de becario: 273317.

Table of contents

Page

Table of contents (continue)

List of Figures

List of Tables

Chapter 1. Introduction

1.1 Waveguides

Guided-wave optics is defined with reference to three-dimensional or free-space optics. In this case, the obstacles met by the light rays are always made of surfaces that usually are orthogonal to the direction of propagation and there are no boundary conditions due to interfaces that would be parallel to the rays. The volume inside which electromagnetic energy is present extends indefinitely in a direction perpendicular to propagation. On the other hand, when the light is guided, boundary conditions are imposed, confining the energy in a restricted volume (Chartier, 2005).

The basic concept of optical confinement is as follows: a medium, called core, with one refractive index n_1 imbedded in a medium, called cladding, of lower refractive index n_0 acts as a light trap within which optical rays remain confined by multiple total internal reflections at the boundaries. Because this effect facilitates the confinement of light generated inside a medium of high refractive index, it can be exploited in making light guides that transport light. An optical waveguide is a light conduit consisting of a slab, strip, or cylinder of dielectric material surrounded by another dielectric material of lower refractive index. The light is transported through the inner medium without radiating into the surrounding medium (Saleh and Teich, 1991).

1.1.1 Guided modes

For total internal reflections to occur in the core-cladding interface, as depicted in Figure 1, the following condition must be satisfied:

$$\theta \leq \sin^{-1} \sqrt{n_1^2 - n_0^2} \equiv \theta_{max}, \tag{1}$$

where θ is the incident angle of the light beam being coupled to the waveguide, and θ_{max} is the maximum light acceptance angle of the waveguide known as numerical aperture (NA). The angle at which light travels within the core is $\phi = \theta / n_1$, but beams with arbitrary angles cannot propagate even when this angle is smaller than the maximum (Okamoto, 2010).

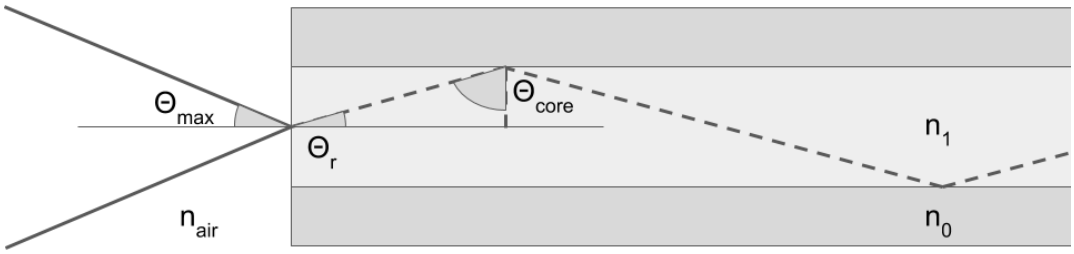

Figure 1. Propagation of light in an optical waveguide. θ_r is the refracted light beam angle at the air-core interface and θ_{core} is the reflected light beam angle at the core-cladding interface.

Waveguides have certain discrete optical field distributions that mantain the same transverse distribution and polarization at all distances along the waveguide axis. Such field distributions correspond to so-called waveguide modes, and in order for the traveling wave to reproduce itself after multiple reflections, the following self-consistency condition is required:

$$\sin\phi_m = \left(m + \frac{\varphi}{\pi}\right)\frac{\lambda}{2d}, \tag{2}$$

where d is the core diameter, m is an integer, and φ is a phase shift introduced by each internal reflection at the dielectric boundary. The mode that has minimum angle ϕ ($m = 0$) is the fundamental mode, whereas the other ones having larger angles are higher-order modes ($m \geq 1$). Each mode has a certain propagation constant β, specifying the phase change per unit length; the lowest order mode has the smallest β value (Paschotta, 2008).

Considering a plane wave propagating in the z-direction at an angle ϕ, its phase fronts are perpendicular to the rays, its wavelength in the core is λ/n_1, and its wavenumber is kn_1 ($k = 2\pi/\lambda$). The propagation constants in the z and x directions are:

$$\beta = kn_1\cos\phi, \tag{3a}$$

$$\kappa = kn_1\sin\phi. \tag{3b}$$

According to the z-components of the electric and magnetic fields, electromagnetic waves can be divided into: (1) Transverse Electric (TE) waves that contain no electric field component in the z-direction but the magnetic field does, and (2) Transverse Magnetic (TM) waves that contain no magnetic field component in the z-direction but the electric field does.

1.1.2 *fs*-laser waveguide writing

Waveguide fabrication techniques can be broadly classified into two main groups: thin film deposition and refractive index modification. The former includes both physical and chemical approaches, while the latter focuses only on physical material modifications (Righini and Chiappini, 2014). The second group comprises *fs*-laser writing for direct 3D microfabrication of optical waveguides, and it comprises some of the most efficient techniques (Osellame *et al.*, 2012).

Since the first demonstration of ultrafast laser inscription for the fabrication of waveguides in a transparent material (Davis *et al.*, 1996), this kind of processing has been widely tested, mainly on glasses and single crystals, due to its potential of creating 3D structures giving place to a number of possible photonic applications, such as enhanced non-linear responses, waveguide lasers, and photonic lanterns, among others (Jia *et al.*, 2012; Siebenmorgen *et al.*, 2009; Calmano *et al.*, 2011; Salamu *et al.*, 2014a; Zhang *et al.*, 2011; Okhrimchuk *et al.*, 2005; Torchia *et al.*, 2008; Birks *et al.*, 2015; Chen and de Aldana, 2014).

The *fs*-laser waveguide writing process mainly depends on the material properties and on the *fs*-laser pulse characteristics. Ultrafast laser inscription is performed by scanning a focused laser beam along a transparent material, creating a localized modification within the focal volume and/or its close proximity.

The scanning velocity (v) regulates the number of pulses (N) that affect certain area of the material being processed as:

$$N = \frac{d \times f}{v}, \tag{4}$$

where d is the beam-waist of the laser beam and f is the pulse repetition rate, which establishes two processing regimes: nonthermal and thermal for low and high repetition rates ($> 200 kHz$ for transparent glasses (Eaton *et al.*, 2005)), respectively. Modification on the structures of crystals have been attributed to heat accumulation and thermal annealing mechanisms when processing with *fs*-lasers at high repetition rates (Nejadmalayeri and Herman, 2007). When working at low repetition rates, cumulative heat effects are not allowed.

fs-laser material processing allows the energy of the pulses to be absorbed through non-linear processes (i.e. two-photon or multiphoton absorption) inducing avalanche ionization in a very short time, causing optical breakdown. If the ionized electrons transfer enough energy to the lattice, the induced material modification can be permanent (Gattass and Mazur, 2008). Such modification can be classified as Type I or Type II if working below or above the optical damage threshold of the irradiated sample, respectively (Gross *et al.*, 2015). The use of ultrashort laser pulses for direct laser writing (DLW) enables increased precision of the written structures (Schaffer *et al.*, 2001), and collateral damage can be avoided with the use of low repetition rate laser pulses (Eaton *et al.*, 2005).

The earliest reports on ultrashort pulse laser inscribed waveguides were all related to waveguides written in glasses (Davis *et al.*, 1996; Eaton *et al.*, 2008; Righini and Chiappini, 2014). Later waveguide inscription with a refractive index contrast of $\sim 4\%$ was achieved in polymers, opening the door to integrated lab on a chip devices (Ding *et al.*, 2008; Shane *et al.*, 2012). Waveguides based on Type I and Type II modification, as well as lasers based on depressed cladding waveguides in single crystals are widely reported (Okhrimchuk *et al.*, 2005; Thomson *et al.*, 2006; He *et al.*, 2013a), while laser induced lattice change mechanisms in ceramic materials have been recently explored (Ródenas *et al.*, 2009; Macdonald *et al.*, 2010; Benayas *et al.*, 2011).

A vast majority of laser-induced structures have been demonstrated in glasses and single crystals, although more recently some laser structures have been written in polycrystalline YAG. Ceramic materials offer high temperature resistance and chemical stability, superior mechanical toughness as well as greater fabrication flexibility when compared to single crystals.

1.1.3 Waveguide configurations

The modifications induced in the materials depend on the *fs*-laser irradiation parameters as well as on the material properties. In general, for a laser pulse to cause material damage in the form of an elongated track, its power P must be enough to allow self-focusing within the bulk:

$$P = \frac{3.77\lambda^2}{8\pi n_a n_b}, \tag{5}$$

where λ is the wavelength in free space, n_a is the linear refractive index and n_b is the non-linear refractive index of the material (Fibich and Gaeta, 2000). P is directly related to the pulse energy and duration, which are the most important parameters since they determine the size and the type of the induced modification. It is known widely that whereas an increase in the pulse energy causes the damage track to elongate in the propagation direction, as the pulse duration becomes shorter the damage track becomes weaker because the non-linear absorption before the focus is stronger.

Therefore, controlling these different parameters, the damage tracks can be shaped as needed to fabricate *fs*-laser inscribed waveguides with different configurations and characteristics.

A Type I waveguide is located inside the *fs*-laser induced tracks. In this configuration, the *fs*-laser will induce positive refractive index changes (Δn) in the irradiated focal volume, which serves as the waveguide core as seen in Figure 2(a). In addition, Type I waveguides in glasses and crystals are usually not stable or even completely erased under high temperature, therefore these Type I waveguides in principle cannot be used in high-power applications (Chen and de Aldana, 2014).

Type II waveguides are formed by at least a couple of parallel *fs*-laser induced tracks, causing expansion of the lattices in the focal volume and hence negative refractive index changes ($\Delta n < 0$) in the directly irradiated region (Figure 2(b). This dilation is accompanied with refractive index reduction, and the surrounding regions may possess a relatively high index through the stress-induced effects. If there are two parallel tracks, the waveguide core is located in the region between them (Burghoff *et al.*, 2007).

Type III waveguides, illustrated in Figure 2(c), are formed by a core that consists of an unexposed area, and a depressed index cladding formed by a number of separate parallel tracks. The refractive index change is negative ($\Delta n < 0$) in the central area of a track. Writing parallel tracks around the unmodified central volume of material produces a depressed cladding with the central volume serving as the core of a waveguide (Okhrimchuk *et al.*, 2005).

Generally, in order to fabricate the 2D ridge waveguides or Type IV waveguides, it is required the ridge construction on base of a planar waveguide layer. A second processing with other technique, like laser ablation, on the planar waveguide may be implemented to remove selected sections of the planar waveguide, thus constructing the ridge waveguides (Figure 2(d)). Here, the waveguide core is formed with lateral confinement by the laser-ablated grooves (Li *et al.*, 2017).

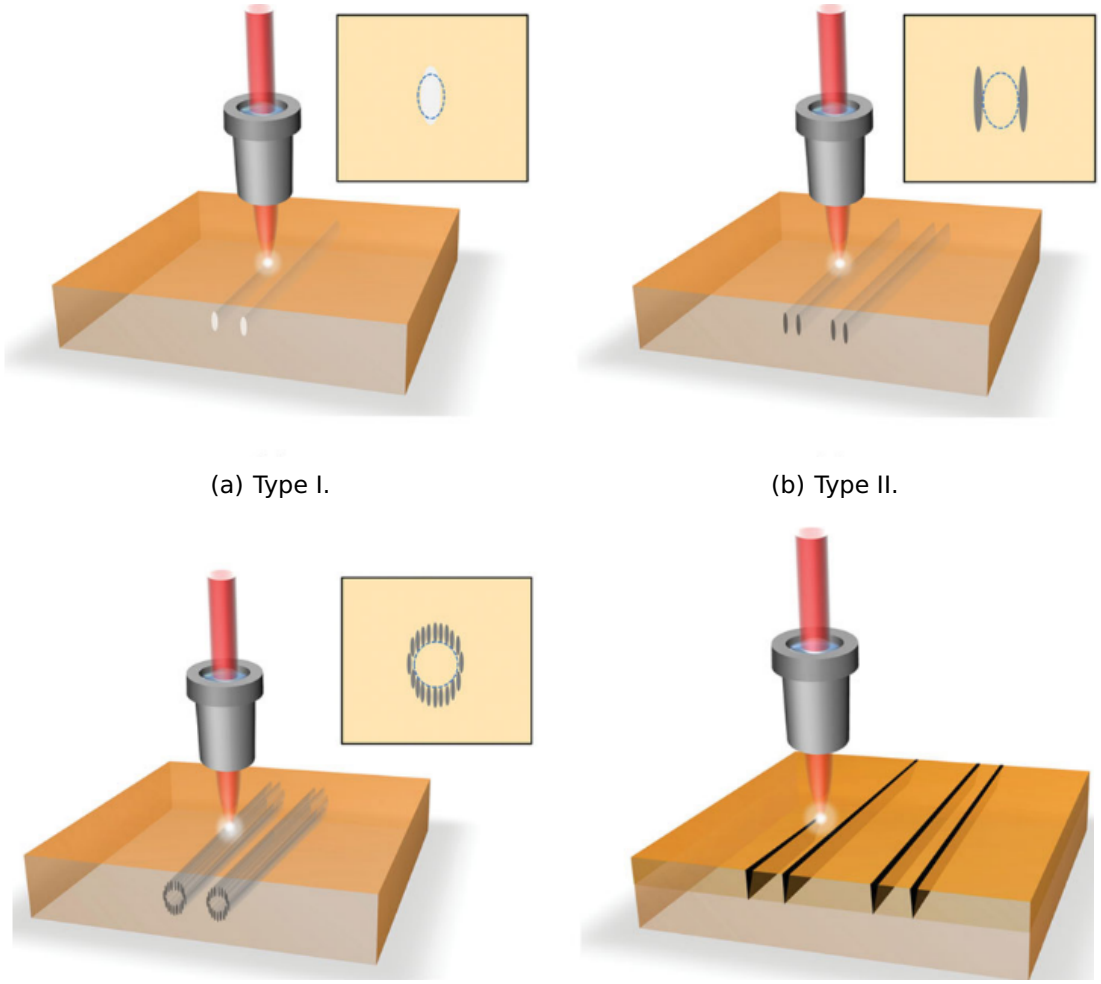

(a) Type I. (b) Type II.

(c) Type III. (d) Type IV.

Figure 2**.** Schematic of the fabrication procedure of *fs*-laser micromachined waveguides in crystals: (a) Type I, (b) Type II, (c) Type III, and (d) Type IV configurations. The insets indicate the cross-sectional sketches of the waveguides. The shadows represent the *fs*-laser-induced tracks and the dashed lines indicate the spatial locations of the waveguide cores (Chen and de Aldana, 2014).

1.2 YSZ ceramic

Polycrystalline yttria stabilized zirconia (YSZ) is broadly recognized as one of the most useful high temperature structural materials due to its favorable ionic conducting properties (Tuller, 2000), high-temperature stability (Zambrano *et al.*, 2018), record toughness (Casolco *et al.*, 2008), and proven biocomptability (Damestani *et al.*, 2013); properties of tetragonal YSZ ceramic used in surgical implants are listed in Table 1.

While these properties make YSZ a promising material for extreme integrated photonic applications, it is largely overlooked. This is because YSZ is not generally considered an optical material, owing to the poor/extant optical quality of conventionally produced YSZ polycrystals.

Table 1**.** Properties of tetragonal YSZ used in surgical implants (Hench, 2013).

Property	**Unit**	**Tetragonal YSZ**
Purity	%	97
Density	gr/cm^3	6.05
Grain size (average)	μm	0.2-0.4
Bending strength	MPa	1000
Compressive strength	MPa	2000
Young's modulus	GPA	150
Hardness	HV	1200
Fracture toughness	$MN/m^{3/2}$	7

1.2.1 YSZ structure

Pure ZrO_2 can be found in monoclinic, cubic, and tetragonal phase. The monoclinic phase is stable at room temperature but tetragonal and cubic phases are stable only above $1100°C$ and $2400°C$, respectively (Hemberger *et al.*, 2016). To stabilize them at a lower temperature, distinct stabilizers, such as Y_2O_3, have to be incorporated into the ZrO_2 lattice. The resultant phase of zirconia is dependent on the degree of stabilizing dopant (see Appendix A).

A concentration of 3% of Y_2O_3 will produce partially stabilized zirconia (PSZ) single phased tetragonal. Increasing the concentration to 8% produces fully stabilized

zirconia (FSZ) single phased cubic; this phase is particularly interesting for the fabrication of heating elements. And a middle concentration of 6% will produce YSZ double phased (tetragonal and cubic) (Ingel and Lewis III, 1986).

The increase in Y_2O_3 content causes an increase in the lattice constant and thus in the $Zr-O$ distance due to the increasing amount of oxygen vacancies which concentrate next to the Zr ions. These vacancies are added as compensation, and are generated because of the different valence states of Zr^{+4} and Y^{+3}.

There are two major outcomes of oxygen vacancies generation. First, since they have a positive charge in zirconia, they can trap electrons and form a color center that absorbs light in the visible; this kind of vacancies are classified as point defects (Ingel and Lewis III, 1986). An oxygen vacancy with a trapped electron can be represented in the Kröger-Vink notation (Kröger and Vink, 1958) as:

$$V_{\ddot{o}} + e' \rightarrow V_{\dot{o}}. \tag{6}$$

But also, as the Y_2O_3 content is increased and the oxygen vacancies are generated, the density of nc-YSZ decreases (Hardin *et al.*, 2013):

$$Y_2O_3 \rightarrow 2Y'_{Zr} + 3O_O^X + V_{\ddot{o}}, \tag{7}$$

where Y'_{Zr} stands for a Zr lattice site replaced by a Y species, leaving a negative charge; O_O^X for an oxygen site replaced by an oxygen species with no change in the charge; and $V_{\ddot{o}}$ for a generated oxygen vacancy with double positive charge.

1.2.2 YSZ for optical applications

Recently, a process that produces bulk YSZ ceramics with nanocrystalline (nc) grain sizes and low porosity has been developed, resulting in an optical grade nc-YSZ with record fracture toughness (Figure 3). In this process, Current-Activated Pressure-Assisted Densification (CAPAD) of high-purity precursor nanopowders is used to consolidate the ceramic optical wafers with $< 1mm$ thickness used in this study (for a detailed report of the processing please refer to Casolco *et al.* (2008)).

In a scattering medium such as nc-YSZ, the trasmittance is expected to decrease exponentially with thickness. Hence, thicker samples are possible in theory but transparent ceramics would not be achieved, ending up with an opaque medium instead. This trend would be expected to be the same across all three mentioned compositions, and more pronounced in the 3% composition due to the non-cubic crystal structures.

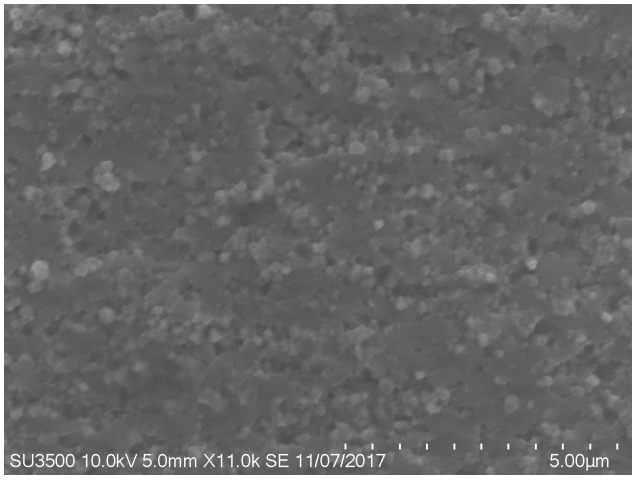

Figure 3**.** %8YSZ SEM micrograph.

Growing the YSZ grains large enough to minimize the number of scattering interfaces would improve the transparency of the samples, creating transparent micrograin YSZ. Nonetheless, this would compromise the mechanical integrity of the ceramics, rendering them more susceptible to failure under modest mechanical loads, since their strength, fatigue response, and fracture toughness are a function of grains size and purity.

ISO standards for ceramics materials used in implants represent another restriction for large grain sizes. For the case of the well-studied and implemented Al_2O_3, the standard average grain size is $< 7\mu m$ (proposed to be $< 4.5\mu m$) (Hench, 2013). For YSZ, this size range further renders the ceramic susceptible to low temperature degradation as water is much easier absorbed between the grains, leading to sudden failure of the implants.

Annealing related tunable optical properties is another feature obtained through a rapid and relatively efficient fabrication method of nc-ceramics (Casolco *et al.*, 2008) as compared to glasses and single crystals. Their use in waveguide fabrication has

not been widespread yet although with amplified pulses, the necessary power to induce permanent optical changes is similar for both crystals and ceramics. However, a method for writing waveguides, in transparent biocompatible nc-YSZ ceramics, using *fs*-laser pulses with very low laser fluence has been already proposed (Castillo-Vega *et al.*, 2012).

Thermal treatment of *fs*-laser written waveguides has been proven to improve the guiding properties of a waveguide, quantified with an increase of the induced refractive index change (Δn) or waveguide losses reduction (He *et al.*, 2013b; Martínez De Mendívil *et al.*, 2015; Nguyen *et al.*, 2017; Piromjitpong *et al.*, 2019). Nonetheless, these studies report on both reduction the of Δn and higher measured losses after the annealing times exceed only 2-4 hours at a maximum temperature of $700°C$.

Waveguides fabricated in conventional materials as glasses, single crystals and polymers generally do not stand high annealing temperatures. On the contrary, ceramic materials are characterized by a high temperature resilience; therefore written waveguides in this kind of materials can be expected to be resilient to high annealing temperatures. Thermally resilient waveguides become very relevant for photonic devices meant to operate in extreme temperature environments in industrial applications.

The addition of annealing induced optical transparency makes nc-YSZ a model system for pursuing DLW photonic structures for unconventional applications. Although the optical losses of nc-YSZ are higher than glasses and single crystals, this new material can be used in more extreme environments (high temperature or impact resistant), allowing photonic structures and devices that simply are not available today.

One such application where biocompatible and optical grade nc-YSZ is being deployed, is as a Window-to-the-Brain (WttB), a new platform (Hernández-Cordero *et al.*, 2018) that enables non-invasive delivery and/or collection of light from the brain, on demand, over large areas, and on a chronically- recurring basis without a need for repeated craniotomies. Optical grade nc-YSZ ceramics meet all requirements for this extreme environment application and also serve as a model system for DLW 3D photonic structures in optical ceramics.

Laser written waveguides in nc-YSZ are a key component to biomedical photonic technology, because they will allow precise delivery of light to locations where therapy is needed within tissues with specific spatial intensity distributions or without any wavefront distortion for mono-mode propagation. In an earlier communication, it was shown that Type I waveguide-like structures could be DLW into transparent nc-YSZ ceramics using *fs*-laser pulses with record low laser energies (2*nJ*) (Castillo-Vega *et al.*, 2012).

The ability to DLW waveguides that retain the coupled modal profile in an optical grade nc-YSZ ceramic that possesses superior chemical, mechanical, and biocompability properties to conventional optical polymers, glasses, and single-crystals is very useful for the development of optical devices for harsh/demanding environments. For example, by providing a non-invasive means for optically accessing the brain on a chronically-recurring basis, i.e. an optical WttB; sensing and spectrometry, in particular for applications in the infrared (Stoian *et al.*, 2016) where nc-YSZ ceramics have their higher transmittance (discussed below); or for the fabrication of highly sensitive waveguide based temperature sensors (Teigell Benéitez *et al.*, 2016; Saha and Kumar, 2018). This work holds considerable potential as a platform for enhancing and/or enabling a wide variety of light-based diagnostic and therapeutic applications not currently possible.

1.3 Windows to the brain

While a number of synthetic materials have been evaluated for use in calvarial reconstruction (e.g., titanium, alumina, and acrylic (Spetzger *et al.*, 2010; Lach *et al.*, 2006; Casolco *et al.*, 2008)), none provides the requisite combination of transparency and toughness required for clinically-viable transparent cranial implants. It has been proven that nc-YSZ represents an attractive alternative (Damestani *et al.*, 2013), because of its high toughness (Lach *et al.*, 2006), its newly imparted transparency (Alaniz *et al.*, 2009), but also due to its proven biocompatibility in dental and orthopedic applications.

By providing non-invasive means for optically accessing the brain, this work holds considerable potential as a platform for enhancing and/or enabling a wide variety of light-based diagnostic and therapeutic applications. Laser written waveguides in nc-YSZ are a key component within Windows to the Brain (WttB), an international partnership to synthesize, characterize, and test a new generation of ceramic materials that will be used to develop a new platform.

Although the nc-YSZ is transparent over a wide wavelength range, some applications may require for light to be delivered in a more concentrated way. Directional light coupling through the window will be explored with direct waveguide *fs*-laser fabrication on the YSZ. Using *fs*-laser pulses, the optical properties of the nc-YSZ ceramics can be readily modified to fabricate different types of waveguides with positive or negative induced refractive index changes and varying sizes.

Bacterial adhesion to the implant and biofilm formation may limit the use of WttB for optical imaging and therapy. Nevertheless, implant transparency may provide an unique opportunity for non-invasive laser-based treatment of infection *in vivo*.

1.4 Bacterial inactivation

With the quick spread of antibiotic resistant bacteria, photodynamic therapy (PDT), and the use of nanoparticles are among the most popular emerging bacterial inactivation strategies. Nonetheless, mechanisms of PDT resistance similar to those in drug resistance have been found by several authors (Casas *et al.*, 2011), and there exists a toxicity concern over the use of certain metallic nanoparticles (Johnston *et al.*, 2010).

Although the use of lasers to reduce bacterial growth *in vitro* was previously reported (Kim *et al.*, 2013; Nussbaum *et al.*, 2003; Sennhenn-Kirchner *et al.*, 2007), their proposed use *in vivo* is entirely novel. Initial *in vitro* studies proposed in this work will use a bacterial culture while monitoring the temperature during laser treatment to optimize the laser parameters. In this context, it is aimed to develop a technique that does not require any external agent to prevent bacterial cells, specifically *Escherichia coli*, from growing.

Escherichia coli or *E. coli*, as normally abbreviated, are a big group of Gram negative bacteria that actually live in the intestines of people and animals. However, some *E. coli* are pathogenic and a specific strain is reported to cause $73,000$ illnesses in the United States, annually (Rangel *et al.*, 2005). *E. coli* cells are rod shaped and each one measures around $1 \times 3 \mu m$, so they can easily be observed under several microscopy techniques for the purpose of assessing their viability prior and after treatment.

In this work a detailed study of three methods for inscribing different configurations of waveguides in transparent nc-YSZ polycrystalline ceramics and a total bacterial inactivation technique by ultrashort pulse direct *fs*-laser irradiation is presented. The thesis is constituted by four Chapters. In Chapter 1 an introduction is presented; Chapter 2 establishes the research methodology; the results and discussion are presented in Chapter 3, and Chapter 4 is dedicated to the conclusions.

Chapter 2. Methodology

This chapter describes the methodology and experimental techniques used for waveguide writing and characterization. The foremost elements of the different setups are a *fs*-laser operating at $\lambda \sim 810nm$, a *fs*-laser operating at $\lambda \sim 1030nm$, and a He-Ne laser operating at $\lambda \sim 633nm$. The samples on which the different types of waveguides were written are all 8% doped Yttria Stabilized Zirconia (%8YSZ).

Direct *fs*-laser bacteria inactivation experiments are also described in this chapter. They were performed to assess the viability to combat infections that are common in patients who underwent neurosurgeries. This kind of infections are usually treated by exposing the brain to drain abscesses or infected tissue. Here, it is proposed to study a minimum invasive technique applying *fs*-laser pulses to a wild strain of growing *E. coli* bacteria —such strain was chosen owing the fact that is one of the most frequent causes of bacterial infections. The main goal is to obtain cellular destruction as consequence of laser-induced stress, but without reaching the temperature threshold for irreparable damage of healthy tissue.

2.1 Sample preparation

The first step in preparing a material for microstructural analysis or processing is sectioning the specimen to expose the area of interest. Desirable effects of this procedure include obtaining a flat surface while minimizing microstructural damage. Common undesirable effects are heat affected zones, excessive surface damage, and pull-outs. The sectioning technique employed for all the samples used in this work is low speed diamond saw, which is classified under the abrasive cutting section of the mechanical techniques (Gunter, 1978).

Except when the specimens are considerable small and thus difficult to hold for sectioning, mounting follows sectioning. Mounting specimens in a holding device is necessary when preparing irregular surfaces. To ensure good adhesion and mechanical stability, a natural resin was used to glue the specimens to a flat metallic holder when a large area ($\sim 1cm^2$) was going to be polished. For the case of thin areas ($< 1mm$ in length) being polished, a hollow metallic holder was used to insert the

specimen letting exposed only the area of interest. This approach utilizes gypsum to keep the specimen in place as displayed in Figure 4.

Figure 4**.** %8YSZ specimen laterally mounted with the help of gypsum. The thin layer in the center is the sectioned sample; the two wider layers at its sides are stabilizing glass; and the yellowish area is gypsum covered with resin. The resin prevents, during the polishing process, residual gypsum to fall on the polishing pads.

2.1.1 Polishing protocol

The final step in the specimen preparation for analysis is recovering the surface microstructural integrity that was damaged with sectioning. For special applications, such as laser processing of materials, it is of vital importance to achieve a flat and clean surface.

Essential polishing products are abrasive, polishing pad, lubricant, and polisher. To obtain the required surface of %8YSZ samples, the directions in Table 2 (Zipperian, 2011) were followed using an automatic polisher. The main unfavorable result of this process was a significant number of pull-outs on the surfaces. To address this issue, manual polishing was implemented with the same products but optical micrography steps were inserted to corroborate the polishing progress instead of setting a determined polishing time.

Table 2. PACE Technologies® polishing directions for engineered ceramics (Zipperian, 2011).

Abrasive/Surface	**Lubrication**	**Force**	**Speed (Head/Base)**	**Time**
30μm DIAMAT diamond on CERMESH metal mesh cloth		$5-10 lbs$	$200/200 rpm$	Until plane
6μm DIAMAT diamond on TEXPAN polishing pad	SIAMAT colloidal silica	$10 lbs$	$200/200 rpm$	$5 min$
1μm DIAMAT diamond on GOLDPAD polishing pad	SIAMAT colloidal silica	$10 lbs$	$200/200 rpm$	$5 min$
SIAMAT colloidal silica on TEXPAN polishing pad		$10 lbs$	$100/100 rpm$	$5 min$

2.2 Waveguide writing experimental setup

The main experimental setup in this work is that of direct *fs*-laser waveguide writing, whose principal components are a pulsed *fs*-laser and a μ-processing lens. This optical array is portrayed in Figure 5, where the optical path of the *fs*-laser pulses are indicated by red and yellow lines. Starting from bottom right to left in red, the *fs*-laser pulses travel through a computer controlled shutter (not pictured), an iris diaphragm set for alignment purposes, a cube polarizer, and a $\lambda/2$ plate. A 45° angled mirror sends the *fs*-laser pulses to a second mirror and to a 90/10 beam splitter. The beam passing through the beam splitter hits a third mirror that redirects the *fs*-laser pulses to the chosen processing lens (tagged L1). After the incidence of the beam on a sample, it is reflected back through the same optical path now indicated in yellow. However, when the beam hits the beam splitter, it will now take a different course: the *fs*-laser pulses get to a fourth mirror and to a second lens (tagged L2) that focuses the *fs*-laser pulses onto a CCD camera. This technique is known as “equivalent target plane".

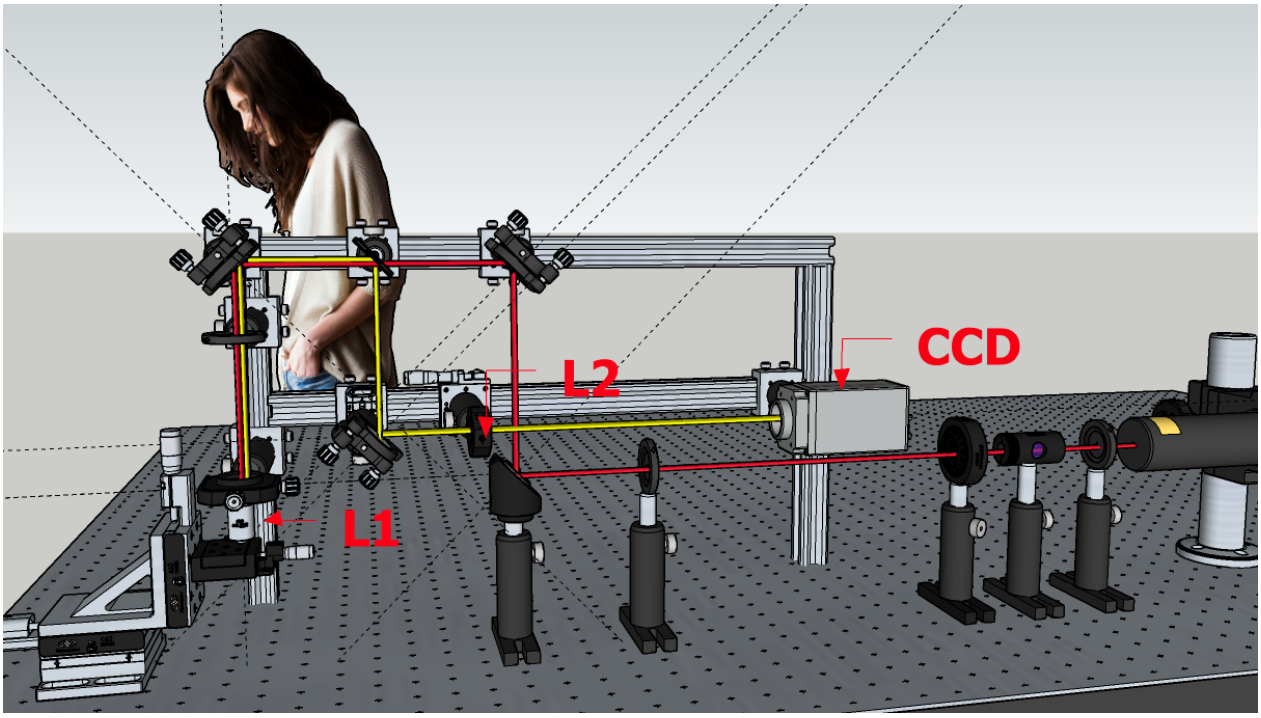

Figure 5. Experimental setup for direct *fs*-laser waveguide writing.

No matter the waveguide configuration being written, the sample was positioned on computer controlled XYZ translation stage system with submicron spatial resolution. The stage includes a tip-tilt platform for plane adjustment and assured normal incidence.

The laser source employed to inscribe all the waveguides studied in this work was an Yb fiber laser (Satsuma HP2, Amplitude Systèmes) producing $270fs$ pulses at a central wavelength of $1030nm$. This laser system possesses the unique feature of pulse energy, pulse duration, and repetition rate tunability. The ranges at which the Satsuma laser operates, as well as other relevant parameters are listed in Table 3. The M^2 and beam diameter were measured at installation in 2016. Pulse energy is at its highest at a $500kHz$ and below.

Table 3**.** Satsuma specifications.

Parameter	**Value**
Pulse energy	$> 40\mu J$ at $500kHz$
Pulse duration	$250fs - 10ps$
Repetition rate	0 to $2MHz$
Polarization	Linear
M_x^2	1.17
M_y^2	1.09
Beam diameter$_x$	$2.63mm$
Beam diameter$_y$	$2.44mm$

For each type of written waveguide (channel, planar or cladding) the tunable parameters were carefully selected. These are stated in each corresponding waveguide fabrication section and are summarized in Appendix B. Nonetheless, it is worth noting that for the channel and planar waveguides fabrication, the laser beam was focused on the surface of the sample during the entire irradiation process. Whereas for the cladding waveguides fabrication, it was focused hundreds of microns below the surface during fabrication.

When it was relevant to assure a superficial interaction, the focused laser beam size and shape were monitored during the entire irradiation process. Figure 6(a) shows the beam size acquired with the equivalent target plane technique, and Figure 6(b) dis-

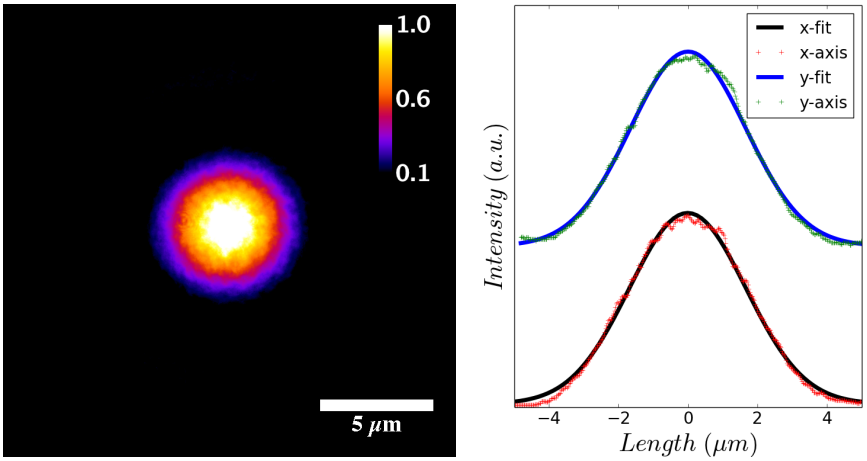

(a) 1030nm focused laser beam. (b) 1030nm focused laser beam Gaussian fit.

Figure 6**.** 1030nm laser beam shape and size when focused with a $f = 4mm$ aspherical lens on the surface of a nc-YSZ polished sample.

plays a Gaussian fit to two orthogonal axes of the beam. A FWHM value was obtained for every fit, which were then used to calculate the beam FWHM with:

$$FWHM = (FWHM_X \times FWHM_Y)^{1/2}. \tag{8}$$

2.3 Channel waveguides

2.3.1 Waveguide fabrication

Three channel waveguides with different separation were inscribed by laser ablation across the surface of a polycrystalline %8YSZ sample (Alaniz *et al.*, 2009), which was polished to optical quality (2.1.1) with diamond abrasive of grain size down to 1μm.

The per pulse energy was set to $\sim 2.6\mu J$ with the help of a half-wave plate and a cube linear polarizer; the selected repetition rate was 500kHz, and the scanning speed was kept constant at 500$\mu m/s$.

Using a computer controlled XYZ translation stage system with submicron spatial resolution and an aspheric lens with $f = 4mm$ and numerical aperture (NA) of 0.75, laser inscription was executed by translating the nc-YSZ sample with respect to the focused laser beam right on the surface. The focused beam FWHM was $\sim 3.8\mu m$, size

that was monitored during the inscription to assure a superficial interaction.

The separations of the channel waveguides were 15, 20, and 30μm. Each pair of channels was separated from the next one by 100μm, measured from center to center, to avoid the creation of extra waveguides in between.

2.3.2 Optical waveguide characterization

To characterize the dimensions of the ablation channels, atomic force microscopy (AFM) measurements were carried out on the surface of the sample. The topographical scans of several $\sim 40\mu m^2$ regions were perform on contact mode. Due to limitations of the AFM scanning depth, scanning electron microscopy (SEM) was used to measure the input and end-faces of the ablated channels. Images of large areas where all the channel waveguides are visible were also obtained.

Supported spatial propagation modes of the waveguides, their insertion losses, and their polarization dependence were obtained by coupling a He-Ne laser into the waveguides.

To couple the beam, a 20X microscope objective was focused on the input-face of the sample and positioned into each waveguide with the help of a XYZ submicron positioning system. At the end-face, a 10X microscope objective and a CCD camera were used to retrieve the propagating modes.

The polarization analysis of the waveguides was carried out employing a half-wave plate to control the polarization of the incident He-Ne laser beam and recording the output power at every position of the plate. This technique allows to verify if the guiding features are input polarization independent.

2.4 Planar waveguides

2.4.1 Waveguide fabrication

Two planar waveguides were inscribed on the surface of custom made $0.8mm$ thickness polycrystalline %8YSZ samples (Alaniz *et al.*, 2009), which were polished to optical quality with diamond abrasive of grain size down to $1\mu m$.

The per pulse energy was set to $2\mu J$ with the help of a half-wave plate and a cube linear polarizer; the selected repetition rate was $1000kHz$, and the scanning speed was kept constant at $500\mu m/s$.

Using a computer controlled XYZ translation stage system with submicron spatial resolution and an aspherical lens with numerical aperture (NA) of 0.75, laser inscription was executed by translating the nc-YSZ sample with respect to the focused laser beam ($FWHM \sim 4\mu m$) on the surface of the sample. This creates waveguides $\sim 30\mu m$ below surface. For the first waveguide (A) a set of 200 lines separated $10\mu m$ between each other was inscribed along the $4500\mu m$ side of the sample; every line consists of 10 laser scans. The second waveguide (B) was made up in the same manner but containing only 100 lines. This technique forms $2000 \times 4500\mu m$ and $1000 \times 4500\mu m$ squares with a positive Δn in the beam focal volume.

2.4.2 Annealing

Transmittance measurements of the processed and unprocessed regions of the nc-YSZ samples were carried out before and after an in-air annealing procedure. Post-waveguide fabrication thermal annealing treatments at $750°C$ for $24hours$ were carried out to test the resilience of the waveguides, to increase the transmittance of the nc-YSZ samples, and to improve the optical performance of the waveguides by removing color centers. It is well known that the so-called Type I modification waveguides, where direct laser written tracks are formed, are weak modifications which usually vanish at high temperatures (Chen and de Aldana, 2014); the induced refractive index change can be either positive or negative according to the material properties. However, our waveguides are thermally resilient at the mentioned record temperature and

for a prolonged period of $24 hours$ —as compared with only $2-4 hours$ at a maximum temperature of $700°C$ for different studies.

- Ramp up from ambiance temperature to $750°C$ at a rate of $10°C/min$.
- Temperature plateau at $750°C$ for $24 hours$.
- Ramp down from $750°C$ to $25°C$ at a rate of $6°C/min$.

2.4.3 Optical waveguide characterization

Supported spatial propagation modes of the waveguides, their insertion losses, together with the polarization dependence, were obtained by coupling a He-Ne laser into the waveguides.

To couple the beam, a $10X$ microscope objective was focused on the input-face of the sample and positioned into the waveguide with the help of a XYZ submicron positioning system. At the end-face, a $20X$ microscope objective and a CCD camera were used to retrieve the propagating modes. Likewise, a $810 nm$ Ti:sapphire laser was used to acquire modal profiles and propagation losses of the waveguides. Only the modal profiles and insertion losses at $\lambda \sim 633 nm$ were measured before and after annealing for comparison purposes; the remaining characterization was performed after annealing.

A polarization analysis of the waveguides was carried out in the same way as with the channel waveguides. A second analysis was performed, only this time adding a polarizer as an analyzer at the waveguides' output. Again, the output power at every position of the plate was recorded to verify if propagation through the waveguides modifies the polarization state of the incident beam. These measurements were taken after annealing.

2.4.4 Micro-Raman measurements

In order to obtain information about the effects that ultrahigh irradiance *fs*-laser pulses have on the crystal phase of the nc-YSZ ceramic, μ-Raman measurements across the laser processed region were carried out. Spectra from two distinct zones

were recorded to identify any laser-induced modification to the crystalline structure of the nc-YSZ ceramic: measurements were taken on the unprocessed region, and in the guiding zone.

2.5 Depressed cladding waveguides

2.5.1 Annealing

Transmittance measurements of the sample were carried out before and after an in-air annealing procedure –750 degrees Celsius in a furnace for 24 hours– to induce transparency into the nc-YSZ sample by removing oxygen vacancies by the thermal diffusion of oxygen into the material (Casolco *et al.*, 2008). Annealing induced transparency gives place to an improved non-linear waveguide writing process, since reaching deeper regions inside the bulk sample with lower laser fluence is now permitted, as a consequence of the reduced linear absorption, i. e. the increased transmittance at the processing wavelength ($1030nm$). With such sample preprocessing, cladding waveguides with two different geometries and diameters were inscribed and characterized.

2.5.2 Waveguide fabrication

Depressed cladding waveguides were inscribed across a custom made $0.8mm$ thickness polycrystalline YSZ sample (Alaniz *et al.*, 2009), which was polished to optical quality (2.1.1) with diamond abrasive of grain size down to $1\mu m$.

The laser source was an Yb fiber laser producing $270fs$ pulses at a central wavelength of $1030nm$ at $1kHz$ repetition rate.

Using a computer controlled XYZ translation stage system with submicron spatial resolution and a $50X$ microscope objective with numerical aperture (NA) of 0.75, laser inscription was executed by translating the nc-YSZ sample with respect to the focused laser beam $150\mu m$ below the surface. This technique forms filaments by a self-focusing effect, which cause catastrophic damage in the focal volume (Salamu *et al.*, 2014a; Ródenas *et al.*, 2009; Benayas *et al.*, 2011; Castillo-Vega *et al.*, 2016).

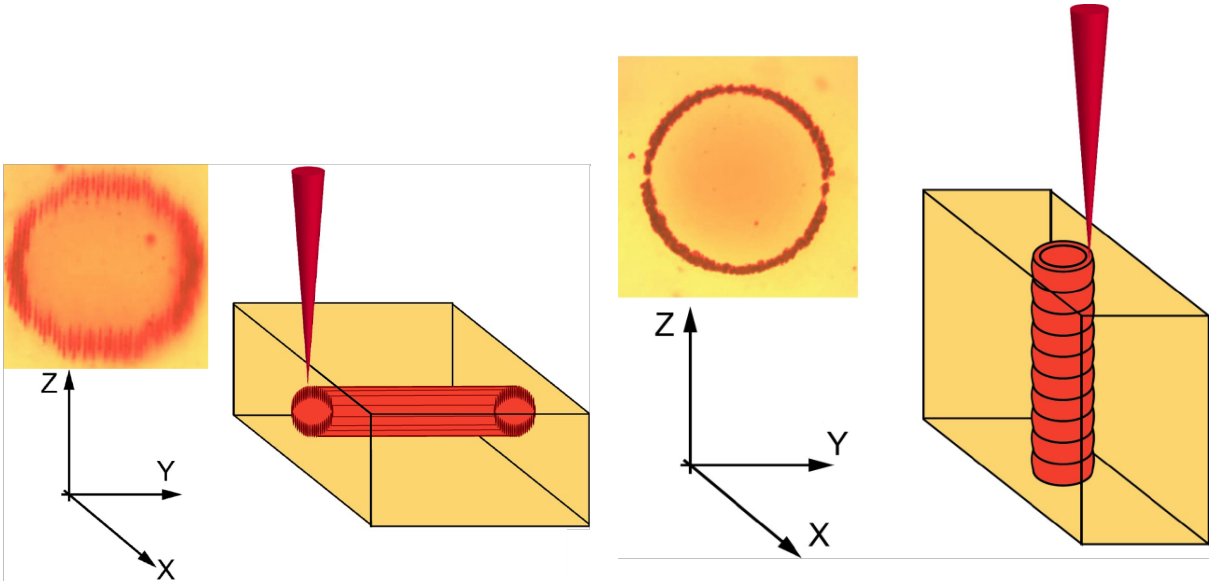

(a) Discrete writing (b) Continuous writing

Figure 7. Diagram of the *fs*-laser direct cladding waveguides writing and their cross sections.

Damage tracks with different scanning speeds, and per pulse energy were inscribed 150μm below surface. The latter in order to find the most suitable writing parameters to create well defined filaments, without collateral damage in between tracks, while avoiding sample fractures.

The per pulse energy was set to 3μJ with the help of a half-wave plate and a cube linear polarizer; the selected repetition rate was 1kHz, and the scanning speed was kept constant at 500$\mu m/s$.

Two depressed cladding waveguide structures with the same dimensions ($\varnothing = 100$-μm) but different geometry were fabricated. In the first configuration, the nc-YSZ sample was translated along a transverse Y-axis to the laser propagation. After a complete scan all across the sample's width, the two remaining X and Z-axes were repositioned and a further scanning was conducted (Figure 7(a)). This formula was repeated until the cross section view of the filaments formed a discrete circular cladding of decreased refractive index enclosing an unmodified bulk region; see cross section of Figure 7(a).

In the second approach, the nc-YSZ sample was turned 90 degrees so the waveguide guiding direction was parallel to the writing laser beam (Z-axis), which was focused on the end surface of the sample.

With a continuous circular displacement on the XY plane, the end-face of the waveguide was written, followed by a Z-step and another XY plane circular movement. The said Z-step was chosen accordingly to take advantage of the inscribed filaments length. This procedure was run through again until the other face was reached. In this manner, multiple cylinders overlapped by a couple of microns to form a single cylinder (Figure 7(b)).

As before, an encircled bulk region remains undamaged, which is now the guiding region; see cross section of Figure 7(b). Additionally, a circular trajectory type waveguide with smaller diameter ($\varnothing = 30\mu m$) was fabricated.

For the well-known discrete circular cladding waveguide, tracks were inscribed with a separation of $3\mu m$ to avoid undesired damage, such as fractures in the material in between tracks. On the other hand, $10\mu m$ Z-step was chosen for the continuous circular cladding waveguide.

The alternative approach for the continuous cladding writing process was implemented in order to reduce propagation losses (Salamu *et al.*, 2014a; Peng *et al.*, 2015), caused otherwise by the discrete nature of the cladding when inscribing circular waveguides as the one shown in Figure 7(a).

2.5.3 Optical waveguide characterization

Supported spatial propagation modes of the waveguides (Figures 31 and 32), their insertion losses (Tables 9,10), together with their polarization dependence were obtained by coupling a He-Ne laser into the waveguides.

To couple the beam, a $20X$ microscope objective was focused on the input-face of the sample and positioned into each waveguide with the help of a XYZ submicron positioning system. At the end-face, a $10X$ microscope objective and a CCD camera were used to retrieve the propagating modes.

Likewise, a 1568*nm* laser diode coupled with a single mode fiber was used to acquire modal profiles and insertion losses of the waveguides.

The polarization analysis of the waveguides (Figure 34) was carried out employing a half-wave plate to control the polarization of the incident laser beam, a second polarizer as analyzer was placed at the waveguides output to verify if propagation through the waveguides modifies the polarization state of the incident beam, and recording the output power at every position of the plate.

2.5.4 Micro-Raman measurements

In order to obtain information about the effects that ultrahigh irradiance *fs*-laser pulses have on the crystal phase of the nc-YSZ ceramic, μ-Raman measurements across the laser processed regions were carried out. Spectra from three distinct zones were taken to identify any laser-induced modification to the crystalline structure of the nc-YSZ ceramic: measurements on the damaged tracks, on a spot far from the laser-irradiated region (bulk), and in between the damaged tracks, i. e. the center of the guiding zone.

2.6 Bacterial inactivation

Prior to any treatment for laser-induced damage, an *E. coli* curve of growth was obtained to understand how cells behave under normal circumstances. To achieve this, a known amount of cells was cultured in a nutritious medium and at an ideal temperature during 12*hours*. Cell counting was carried out every hour to monitor the rate at which bacteria replicate.

Understanding of bacteria growth under ideal conditions is imperative so the laser-induced damage can be assessed by directly comparing normal cells and treated cells.

Furthermore, an *E. coli* absorbance spectrum was acquired. This is specially relevant since thermal effects are undesired due to medical constrains, thus it is important to assure low absorption at the wavelength of treatment laser.

2.6.1 Cell culture

Every sample at which laser treatment was applied was taken from a previously prepared cell culture. The samples were conceived in liquid state with distilled water to avoid laser light absorption of anything but the bacteria. The cultures consisted in lysogeny broth (LB) mixed with agar in sterile Petri dishes. LB is the medium of choice for bacteria growth due to its highly nutritious content, while the use of agar facilitates the isolation of individual colonies and relocation to liquids.

Table 4. Ingredients of $500mL$ of LB agar.

Ingredient	**Amount**
Tryptone	$5g$
Yeast extract	$2.5g$
Sodium chloride	$5g$
Agar	$7.5g$
Distilled water	$475mL$

LB agar media can be prepared by mixing and sterilizing the ingredients in Table 4 or can be found in powder form ready to only mix with water. The following procedure was followed to transfer a strain from a plate culture or tube to a sterile plate culture. This has to be done only the first time that cells are growing in the current laboratory and repeated when there are no more stored sterile Petri dishes.

Procedure to transfer a stain to a sterile plate culture:

1. Prepare $500mL$ of LB agar mixing the ingredients in Table 4. Use a graduated cylinder to make a total of $500mL$ and autoclave it in a Pyrex® bottle for $15min$ at $121°C$.
2. Let the LB medium cool down to room temperature. If the bottle reaches the LB medium solidification temperature, it has to be heated again. This can be done in a water bath if the bottle has not been open.
3. If some undissolved powder is present, put the bottle on a magnetic stirrer until there is a homogeneous substance.
4. Unpack Petri dishes inside a disinfected laminar air flow hood and put them next to each other carefully opening them without touching the inside. Around 15 dishes can be filled up with $500mL$ of liquid LB medium.
5. If available, turn on the UV lamp inside the hood and let rest for $15-20min$.
6. Fill up the Petri dishes to obtain a $\sim 0.5cm$ layer of LB medium in each one and let them open until the LB medium is completely solid. Close them and turn off the laminar air flow.
7. Incubate the Petri dishes at $37°C$ for $24hours$. This will allow to see if they are contaminated, usually with common strains of fungus. Discard contaminated dishes.
8. Those Petri dishes that are not going to be used right away, can be stored up to a couple of weeks inside a $4°C$ refrigerator.
9. Inside a disinfected laminar air flow hood, use a sterile inoculating loop to scrape off a small amount of a colony of the strain to inoculate, which can be in another Petri dish or in a well preserved Eppendorf tube®.
10. Open the Petri dish to inoculate, insert the loop and inoculate the dish by gently moving the loop through the entire surface in order to disperse the cells. *Open every container only partially, just enough to put the inoculation loop inside and outside.
11. Incubate the culture at $37°C$ for $24hours$. *Every new culture has to be tagged prior to inoculation.

The following procedure was implemented every time a new sample was needed, and it takes into account a viable previously grown cell culture on a Petri dish. The number of cells per volume water was varied in several laser treatments to find the optimum value. The density of the samples was measured using the standard optical density at $600nm$ (OD600), which is a linear scale where a value of 1 corresponds to $8 \times 10^8 cells/mL$. Once it is completed, the initial control from the day before can be used to prepare a new sample.

Procedure to prepare for irradiation a strain from a plate culture to a cuvette:

1. Inside a disinfected laminar air flow hood, use a sterile inoculating loop to scrape off a small amount of a colony of the strain to inoculate.
2. Dissolve the cells into a spectrophotometer cuvette with distilled sterile water.
3. Use a vortex at moderate speed to mix the solution.
4. Measure the OD600 of the solution in a cell spectrometer.
5. Repite the previous steps to adjust the desired OD600 value by adding cells or water as needed.
6. Prepare 1/100 and $1/1,000$ dilutions in two Eppendorf tubes® with sterile pipettes.
7. Use sterile pipettes to put the same amount of each dilution in Petri dishes.
8. Use an inoculation loop to disperse the cells by gently moving the loop through the entire surface.
   *Open every container only partially, just enough to put the inoculation loop inside and outside.
9. Incubate both cultures, which will serve as initial control, at $37°C$ for $24hours$.
   *Every new culture has to be tagged prior to inoculation.
10. Let only the volume to irradiate in the cuvette, and put the same amount on a different container which will serve as irradiation control.
11. Seal both containers. Subject the cuvette to treatment and keep the control next to the cuvette but without being irradiated.

2.6.2 Laser treatment

A Ti:Saphire pulsed *fs*-laser was used to irradiate several $300\mu L$ samples, which consisted of distilled sterile water and $\sim 10^7 cell/mL$ solutions. Treatment parameters varied to get optimal and most efficient inactivation conditions while some others like beam diameter ($\sim 15.6\mu m$), wavelength ($\lambda \sim 810nm$), pulse duration ($\sim 100fs$), repetition rate ($89MHz$) and a constant magnetic stirring remained unchanged.

Since during the treatment process cells are not immersed in bacterial growth media, a replica of the sample –which served as irradiation control– was kept aside the laser beam in order to have a count of possible dead cells due to lack of nutritional requirements or ambiance conditions. The temperature of both sample and its control was monitored throughout the *fs*-laser irradiation to discard bacterial damage caused by thermal effects. For this matter, a FLIR® thermal camera was employed during the treatment.

In addition, treatments with a *ns*-laser operating at $532nm$ and a second *fs*-laser operating at $1030nm$ were implemented. Since it was found that the *E. coli* aqueous solutions augmented their temperature in matter of seconds under $1030nm$ treatment, the temperature was recorded in time to identify the longest possible treatment at such wavelength without reaching $40°C$.

2.6.3 Damage assessment

Right after treatment is completed, the irradiated sample and its irradiation control have to be inoculated into Petri dishes. Once the cells had have enough time to grow macroscopically, colony counting is performed to compare both cultures and assess the laser-induced damage.

To grow the sample and the irradiation control to a Petri dish, their $1/100$ and $1/1,000$ dilutions were also obtained and inoculated in the same way as the initial control. After $24hours$, there will be two dilutions of initial control, two of irradiation control, and two of the sample.

Another useful way to assess damage in cells is the use of stains in combination with fluorescence microscopy. Popular selective stains used in fluorescence microscopy for membranes, genetic material, and other specific regions of cells are not designed to be used with bacteria, and considering a lot of them may act according to morphology, one cannot rely on the dye's indications when applied to *E. coli*.

A double staining protocol (Appendix C) was developed to examine *E. coli* viability before any treatment was applied and to identify possible laser induced membrane damage. Using adequate two or more stains in one sample helps to recognize different cell structures because each one of them binds to different cellular content. The best combination that has been found so far is Acridine Orange (AO) and Propidium Iodide (PI). They have excitation maximums at 500*nm* and 530*nm* and emission maximums at 526*nm* and 620*nm*, respectively. AO is indicated to be combined with DNA, while PI interacts with the nucleus of dead cells.

Using this mixture, fluorescence microscopy observations of viable cells and negative controls were carried out. Negative controls are intentionally killed cells, usually by heat, to have a proof of how dead cells should react to different dyes.

As a complement, three dimensional images of stained *E. coli* before and after laser treatment were taken using confocal microscopy.

Chapter 3. Results and discussion

This chapter presents the results obtained for polishing of the nc-YSZ, the *fs*-laser processing for the formation of three different types of waveguides, and their characterization including: structural measurements, allowed propagating modes, polarization dependence, and induced refractive index change.

The last section describes the results concerning the bacterial inactivation experiments, which assess the hypothesis of inactivating bacteria through a non-linear optical mechanism, leveraging the inherent high peak irradiance of an ultra-short laser pulse. To achieve this, two *fs*-lasers with different wavelengths were tested (810 and 1030*nm*), as well as a third Nd:YAG operating at a central wavelength of 532*nm* for comparison purposes.

3.1 Polishing

Figure 8 illustrates the different polishing steps taken to achieve the desired surface quality of all the nc-YSZ samples used in this work. Each step was performed with a different abrasive as indicated in Table 2. Although this series depicts only the polishing process of one side of one sample, the other side, its surface, and those of the other samples were polished until equivalent results were obtained.

The voids at the sides of the sample are produced while sectioning the sample and cannot be avoided. For cladding waveguide inscription, this is not an issue since the edges are not processed. Nevertheless, for superficial processing (like channel or planar waveguide writing), edges with defects most be avoided or substantially reduced by rough polishing.

3.2 Channel waveguides

Monitoring of the laser beam during the writing of the waveguides was not possible due to the ablation process. When the focused beam scanned each channel on the surface of the sample, ablation was instant and thus the beam could not be reflected to the CCD camera. Nonetheless, appropriate focusing was corroborated before and

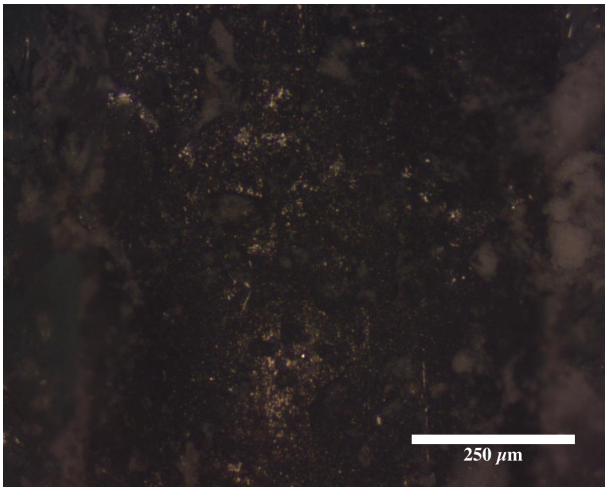

(a) Sample after being cut and mounted.

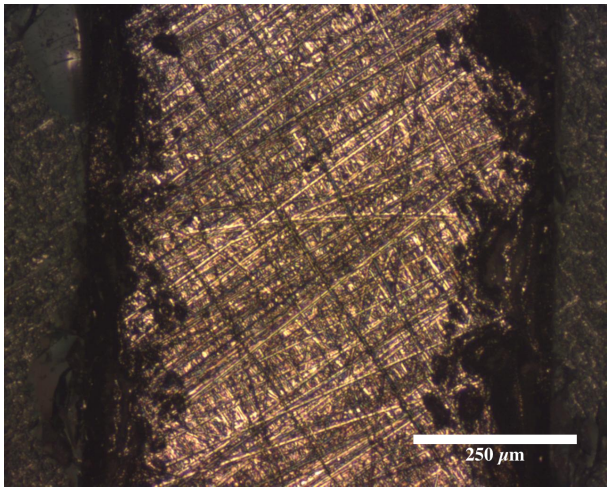

(b) Sample after polishing with 30μm abrasive.

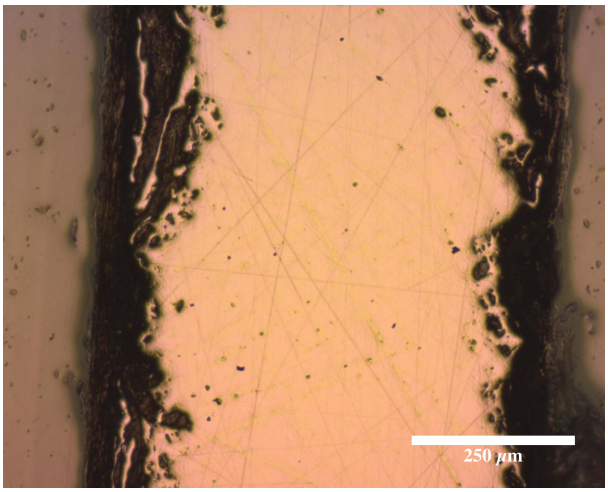

(c) Sample after polishing with 6μm abrasive.

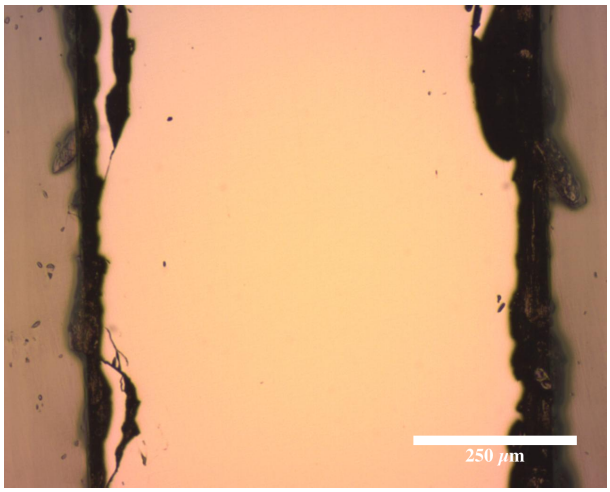

(d) Sample after polishing with 1μm abrasive.

Figure 8**.** nc-YSZ side view after each step of the used polishing procedure. This images correspond to the sample where the cladding waveguides were inscribed and were taken using confocal reflection microscopy with a 10X objective.

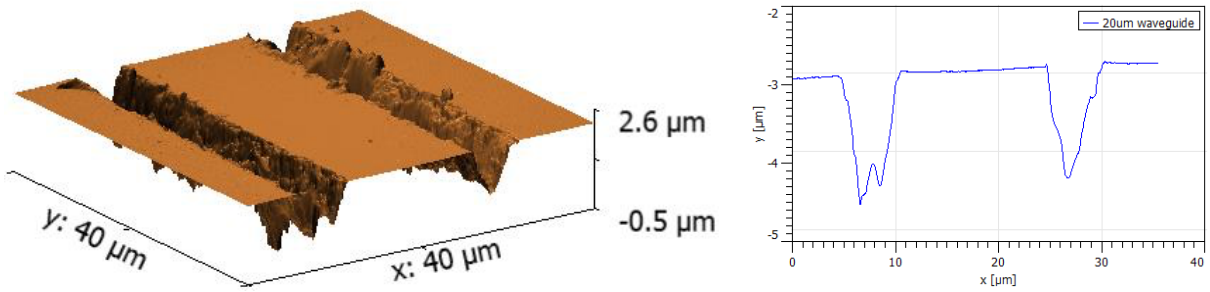

(a) Three dimensional AFM micrograph. (b) Cross section measurement.

Figure 9. AFM micrograph of the 20μm channel waveguide in nc-YSZ.

after the waveguides writing at different positions with irradiation conditions below the ablation threshold. It was found that focusing the 1030nm laser beam with an aspherical lens of 4mm in focal length, the $FWHM$ was 3.91μm. This value was calculated using Equation 8 and the measured values $FWHM_X = 3.94\mu m$ and $FWHM_Y = 3.90\mu m$.

The surface morphology of the channel waveguides inscribed on a nc-YSZ sample was analyzed using both AFM and SEM techniques. The three dimensional AFM topography of the waveguide with 20μm in width is shown in Figure 9(a) —this image was obtained with a scanning area of $40 \times 40\mu m$. As can be seen, 20μm correspond to the width from center to center of the ablation channels, leaving trapezoidal waveguide with a base of 20μm, 15μm at the top, and a height measured with SEM of $\sim 9\mu m$.

Several cross section measurements were taken from this area to investigate the shape and depth of the channels. As can be seen in Figure 9(b), which shows a representative AFM cross section measurement of the 20μm waveguide, the ablation channels present a triangular cross-section that has $\sim 6.5\mu m$ in width and $1.3 - 1.5\mu m$ in depth. The same result was obtained from the 15μm and the 30μm waveguides. Despite that, as discuss below, these results are not completely accurate since the actual depth of the ablation channels overrides the AFM capacity.

Larger mapping was obtained with SEM images. Figure 10(a) is a top view map of the three channel waveguides. Although the far left channel is slightly wider than the others, this is attributed to the sample being inhomogeneous. The average width of ablation channels was measured to be 6μm, which is consistent with AFM measurements.

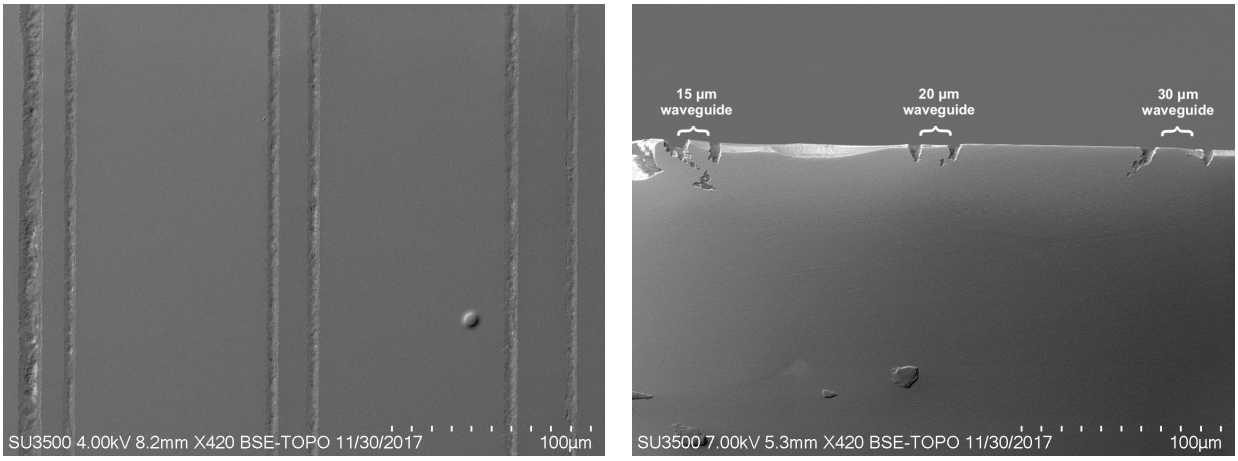

(a) Top view. (b) Side view.

Figure 10. Channel waveguides SEM micrographs. From left ro right: 15μm, 20μm, and 30μm waveguides.

Figure 10(b) is a side view, corresponding to the input-face of the waveguides. Sectioning defects were found near the waveguides but not on their cores, yet the 30μm channel waveguide end-face was chipped. The average depth of the ablation channels was 8.9μm, which is by far greater than depths measured with AFM.

Concerning the wave-guiding properties of the channel waveguides, end-face viewing setup reveals that the near field intensity distributions are true to shape and size of the waveguides boundaries for the 15 and 20μm waveguides, which indicates a good optical confinement of the written structures. Regardless of the existence of weak guiding properties even on the areas between waveguides –channels separated $75-80\mu m$–, the 30μm did not present any propagation mode. This is attributed to the mentioned chipped region on its end-face.

From the results it was found that the 15μm waveguide displays an angled monomode propagation, while a multi-mode triangular shape was observed for the 20μm waveguide. Figures 11 and 12 show the guided TE and TM spatial propagating modes at 633nm of the channel waveguides in nc-YSZ ceramic. Both waveguides support TE and TM spatial modes, albeit they do not appear exactly the same. This points out that light confinement is polarization dependent, as it could be expected because of the geometry of the inscribed waveguides.

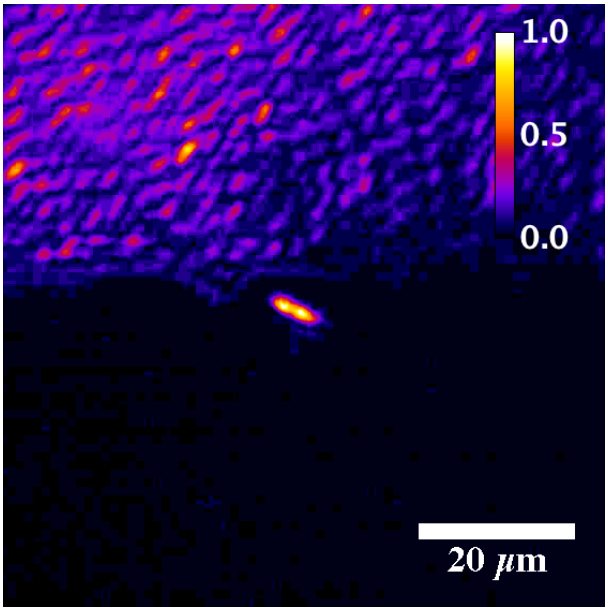

(a) 15μm channel waveguide TE propagation.

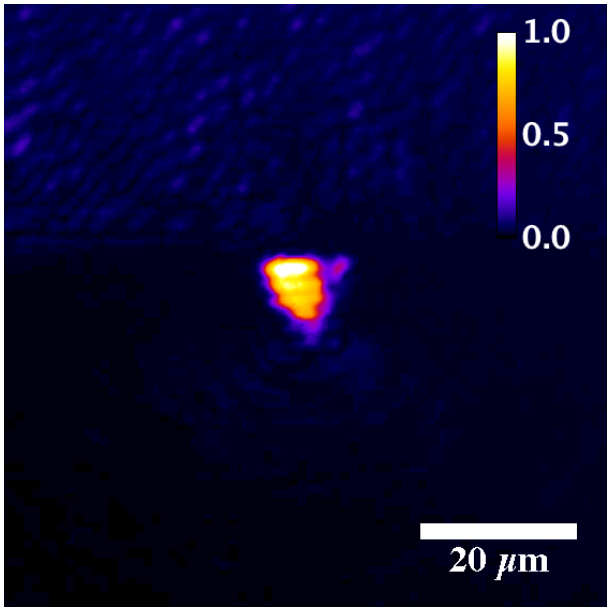

(b) 20μm channel waveguide TE propagation.

Figure 11**.** Channel waveguides TE propagating modes at 633nm.

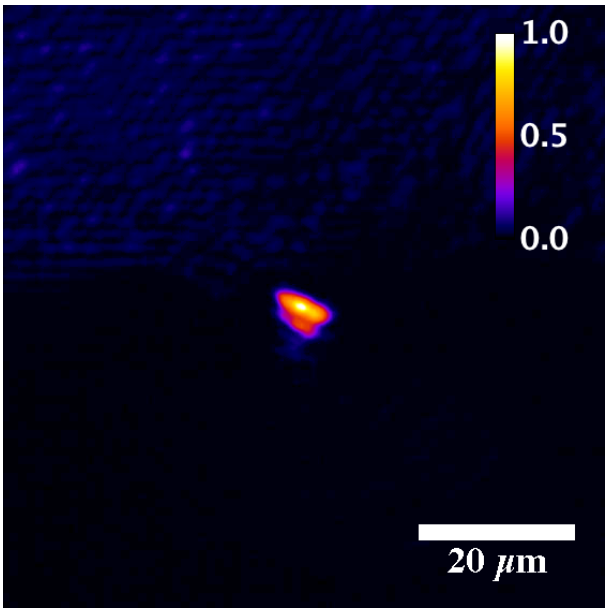

(a) 15μm channel waveguide TM propagation.

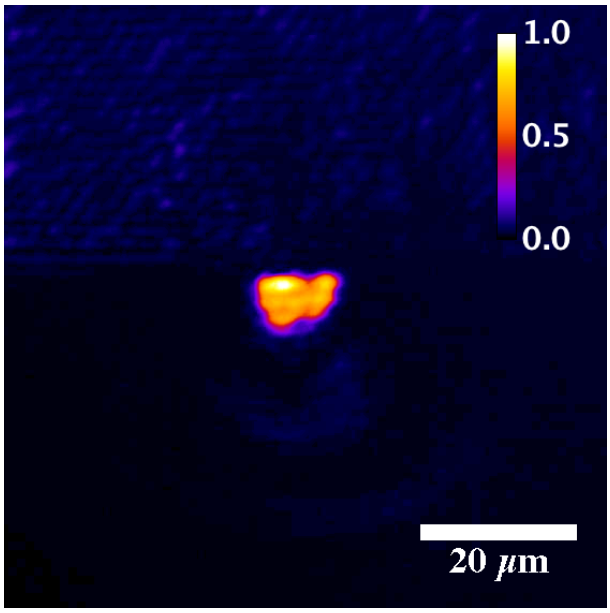

(b) 20μm channel waveguide TM propagation.

Figure 12**.** Channel waveguides TM propagating modes at 633nm.

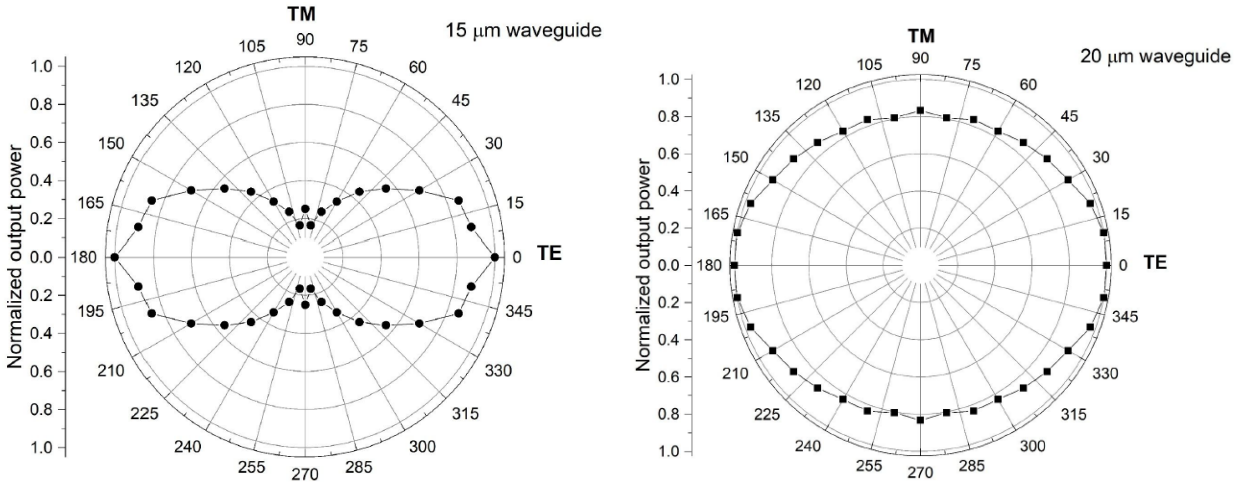

(a) 15μm waveguide polarization dependence. (b) 20μm waveguide polarization dependence.

Figure 13**.** Channel waveguides output power (normalized) dependence on the polarization of the incident light at 633nm.

The polarization analysis denotes that this dependence is sharper for the 15μm waveguide than for the 20μm waveguide. Figure 13 displays the analysis for both waveguides, where the dots in the polar map correspond to measured power at the output face of the waveguide for every input polarization angle, normalized to the maximum output value, and 0° corresponds to TE polarization.

Regarding the insertion losses, presented in Table 5, they were estimated by collecting the output of the waveguides with the coupling experimental setup. Current high losses are attributed to linear optical absorption caused by oxygen vacancies inherent to the sample fabrication. When compared with the insertion losses for the planar and cladding waveguides, it was found that high losses are also due to this configuration, which turned out to be the most inefficient.

Table 5**.** Measured insertion losses at 633nm of the channel waveguides for TE and TM polarized incident light.

Waveguide	**TE**	**TM**
15μm	40dB	46dB
20μm	39dB	40dB

3.3 Planar waveguides

On the subject of the processed region, it appears as a light color well defined squared zone with no ruptures or fractures neighboring it (Figure 14). This is likely generated as a result of a linear optical process, like *fs*-laser induced thermal annealing, that removes oxygen vacancies within the irradiated region. A non-linear optical process where the material is optically excited by the transferred pulse energy could also be possible (Apostolopoulos *et al.*, 2004). A third possibility is the color centers suppression due to decoupling of trapped electrons within the oxygen vacancies, a process that would be stimulated by the high intensity electric field of *fs*-pulses —this is an ongoing research in the Ultrashort Pulse Lasers and Processing of Materials Laboratory.

Monitoring of the laser beam revealed that it was appropriately focused on the surface of the nc-YSZ sample during the entire inscription process. For the second planar waveguide, this process lasted $\sim 4.5 hours$ and involved a surface area of $\sim 4.5 \times 10^{-2} cm^2$.

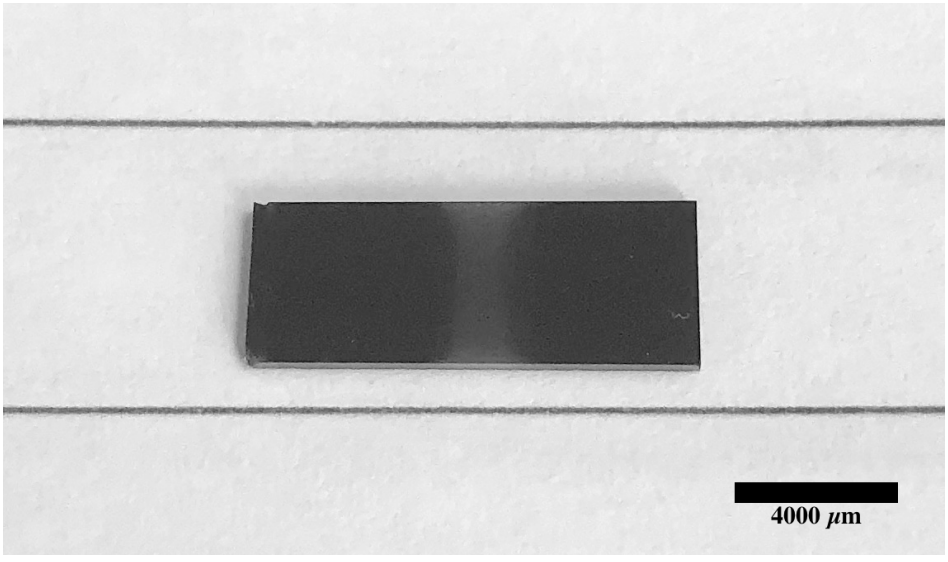

Figure 14**.** Planar waveguide on the surface of a nc-YSZ ceramic before annealing.

There is a significant difference in the appearance of the samples after annealing in air. The samples were dark gray color when sinterized, but after annealing they became lighter due to oxygen diffusion into the material, which suppresses color centers. It is well known for the particular case of nc-YSZ that as the annealing time is increased, its optical transmission enhances while the absorption coefficient decreases (Alaniz *et al.*, 2009). Transmittance measurements denote that after 24 hours of annealing the transmission of the processed and unprocessed regions increases (Figures 15 and 16), and that this increment is wavelength dependent. The latter is illustrated in Figure 17, where a significant transmittance improvement is seen for the planar waveguide region at wavelengths greater than $\lambda \sim 900nm$.

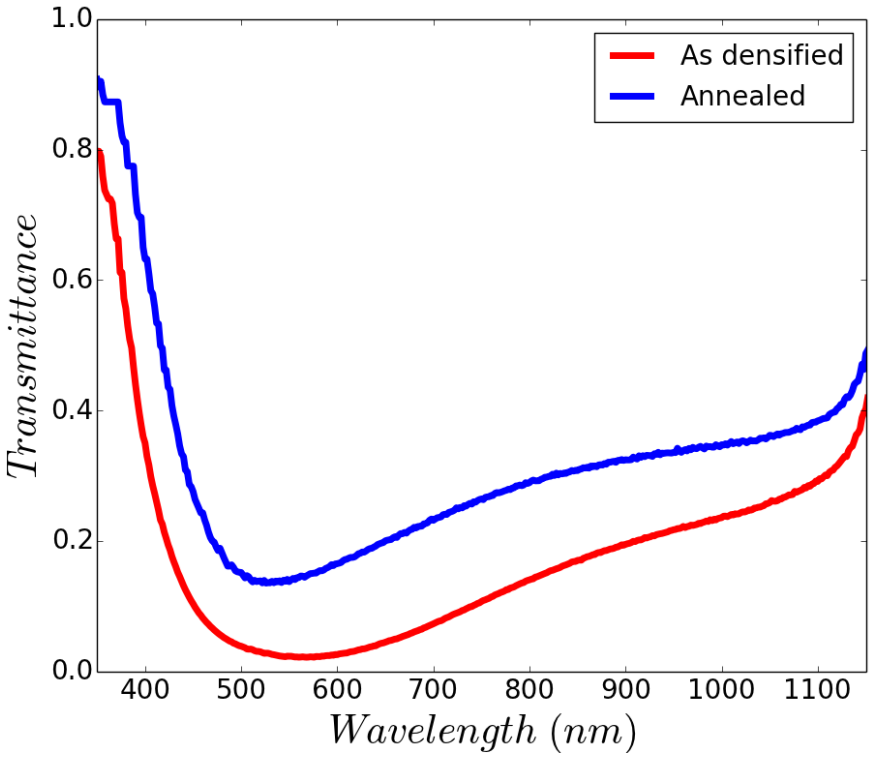

Figure 15. As densified and 24 hour annealed transmittance of a planar waveguide.

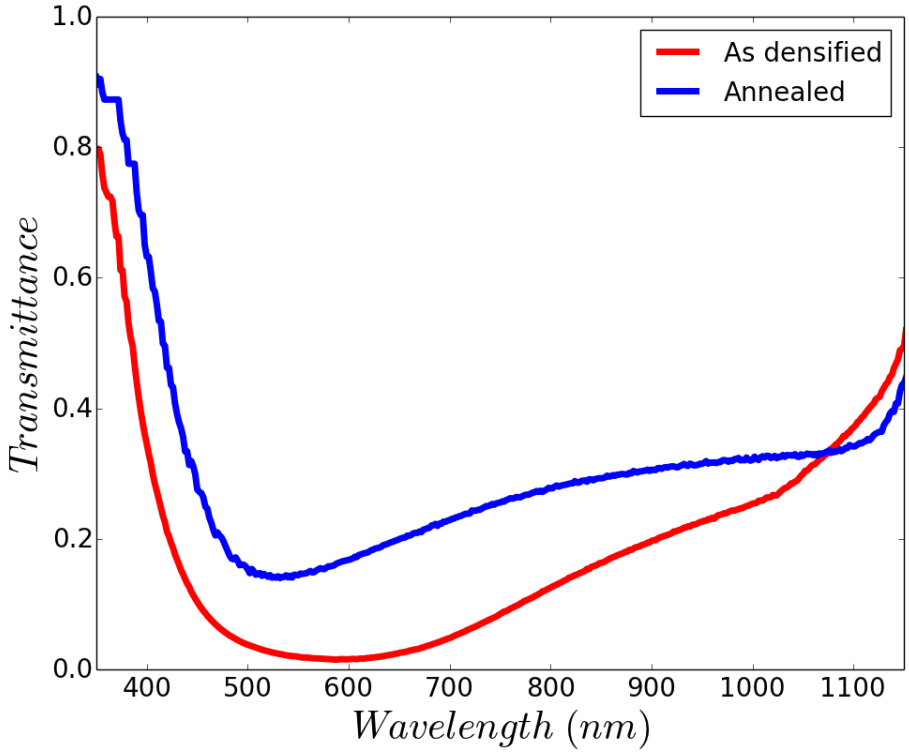

Figure 16. As densified and 24 hour annealed transmittance of a nc-YSZ ceramic.

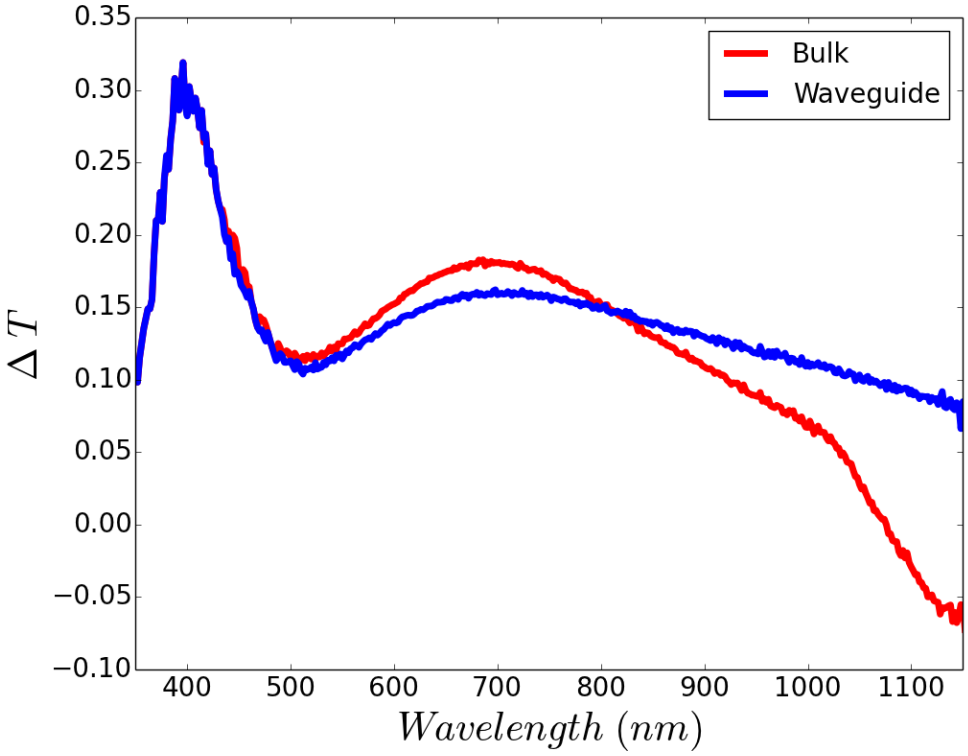

Figure 17. Transmittance increment after 24 hour annealing of a region of the nc-YSZ ceramic that was not laser processed and of a planar waveguide.

Annealing experiments of the planar waveguides were performed so that transmittance of nc-YSZ is raised. Type I modifications are weak modifications which generally disappear when subjected to high temperatures. Both planar waveguides visually vanished since the entire samples became clearer and transparent as seen in Figure 18. In spite of this, the direct *fs*-laser written waveguides remained and even their optical properties are improved (discussed below). Such temperature stability suggest that Δn is caused not only by cumulative laser irradiation thermal effects which lead to structural modification of the lattice or densification, but by physical processes that are not dependent on temperature. For instance, color center suppression, which depends either on photon energy or electric field intensity.

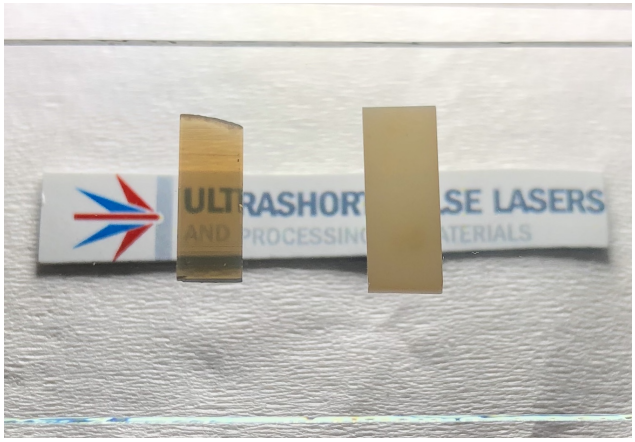

Figure 18**.** Planar waveguides on the surface of nc-YSZ ceramics after annealing.

Thermal annealing has been previously found to diminish the waveguides propagation losses and to increase the laser induced Δn by several studies, some of which are summarized in Table 6. It is worth noting that although the waveguides optical properties have been demonstrated to improve with thermal treatments, none of these studies have reached the temperature at which our waveguides underwent, nor for as long.

Table 6. Temperature values ($°C$) and their respective treatment time (in hours) at which *fs*-laser written waveguides start to vanish according Δn decrease or increasing losses. All three crystals correspond to single crystals, while the ceramic is a polycrystalline ceramic. * cumulative $1-hour$ treatments; ** cumulative $3-hour$ treatments; *** this work.

Material	Type	Temperature	Time	Waveguide type	Criteria
crystal	$Bi_4Ge_3O_{12}$	260	2*	cladding	higher losses[He *et al.* (2013b)]
glass	$CaSio_3 - Ca_3(PO_4)_2$	650	0.5	cladding	higher losses[Martínez De Mendívil *et al.* (2015)]
crystal	$LiNbO_3$	300	6**	cladding	Δn decrease[Nguyen *et al.* (2017)]
crystal	$LiNbO_3$	700	3	cladding	Δn decrease[Piromjitpong *et al.* (2019)]
ceramic	YSZ***	750	24	planar	unaffected waveguide optical features

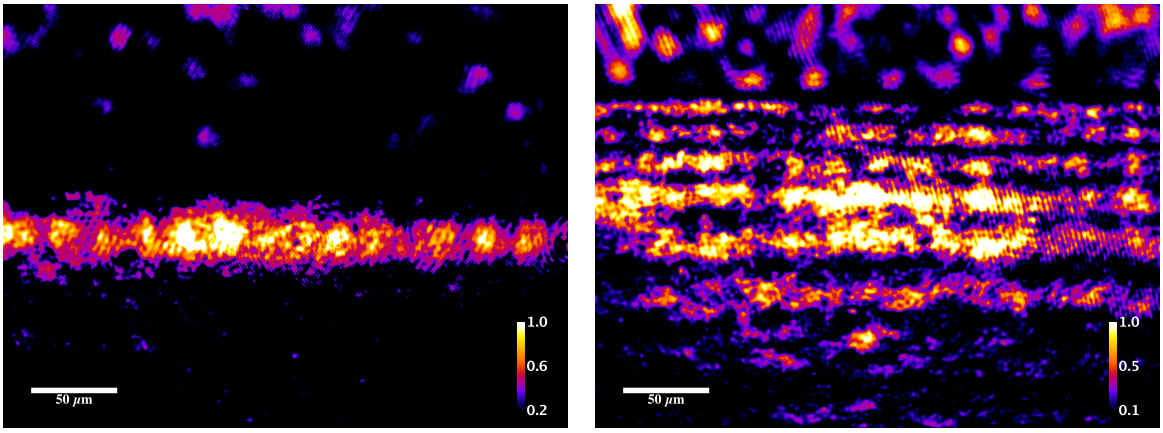

(a) TE polarization monomodal propagation. (b) TE polarization multimodal propagation.

Figure 19. Spatial propagating modes at 633*nm* of the second planar waveguide in nc-YSZ ceramic before annealing.

Furthermore, end-face viewing setup reveals that the near field intensity distribution is consistent with planar waveguides, that the waveguides can be excited to mono-mode or multi-mode propagation according to the depth of the coupled beam, and that guidance is supported for both TE and TM incident polarized light. Figures 19 and 20 depict the propagating modes before and after annealing, respectively. Guidance in mono-mode and multi-mode was also observed at 810*nm*; Figure 21 corresponds to TE single-mode propagation.

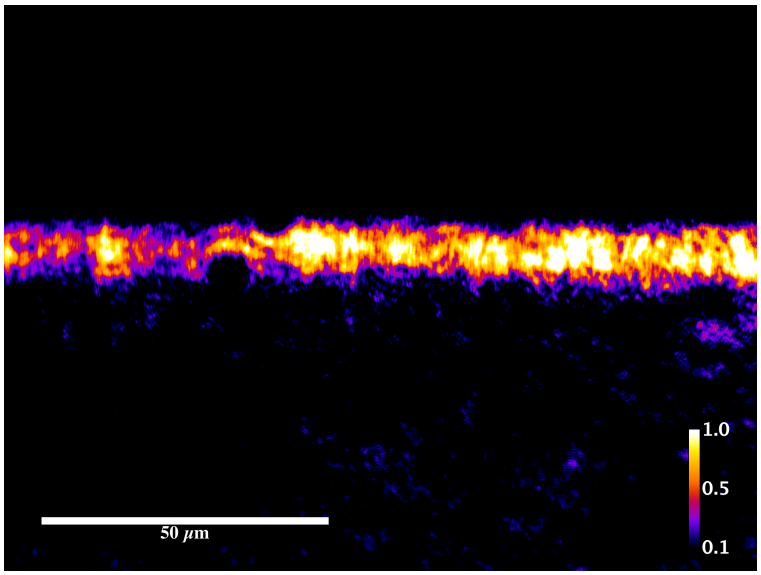

Figure 21. TE spatial propagating mode at 810*nm* of the second planar waveguide in nc-YSZ ceramic after 24 hours of annealing in air.

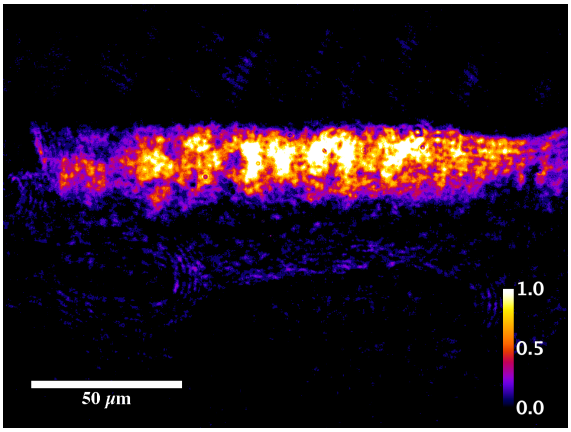

(a) TE polarization monomodal propagation.

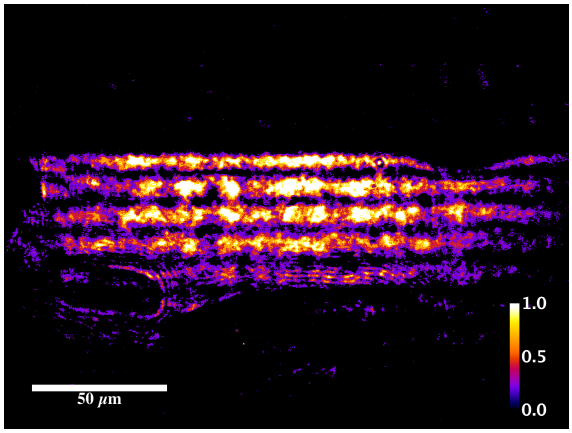

(b) TE polarization multimodal propagation.

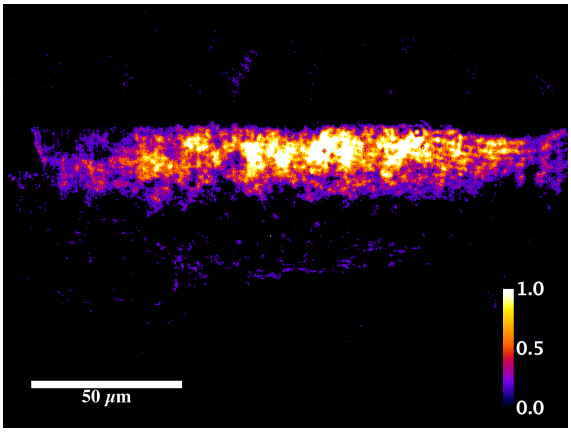

(c) TM polarization monomodal propagation.

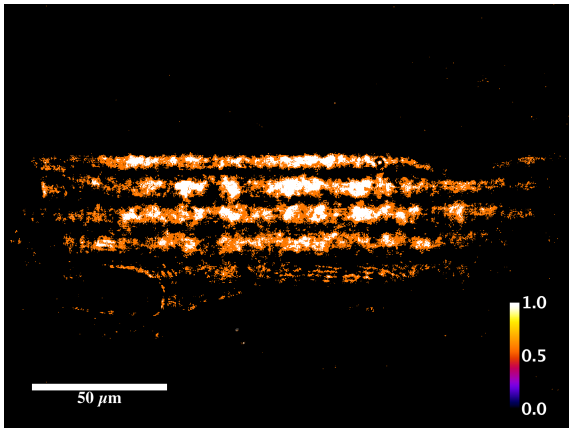

(d) TM polarization multimodal propagation.

Figure 20**.** Spatial propagating modes at 633*nm* of the first planar waveguide in nc-YSZ ceramic after 24 hours of annealing in air.

Concerning the refractive index contrast between the unmodified region and the irradiated zone, a finite-element time-domain method in COMSOL® software was applied to quantify the refractive index contrast of the planar waveguides using a $n = 2.2$ for the bulk material. This was accomplished by comparing the theoretically allowed propagating spatial modes, assuming different Δn values, with those observed experimentally. Chosen Δn values correspond to previously measured Δn induced by *fs*-laser irradiation in ceramic materials (Siebenmorgen *et al.*, 2009; Okhrimchuk *et al.*, 2005; Ródenas *et al.*, 2009; Liu *et al.*, 2012).

The results, depicted in Figure 22, indicate a contrast of $\Delta n \sim 10^{-4}$ between the written waveguides and the unprocessed material, magnitude which is in good agreement with other previously reported *fs*-laser induced refractive index changes in ceramic materials (Siebenmorgen *et al.*, 2009; Okhrimchuk *et al.*, 2005; Ródenas *et al.*, 2009; Liu *et al.*, 2012).

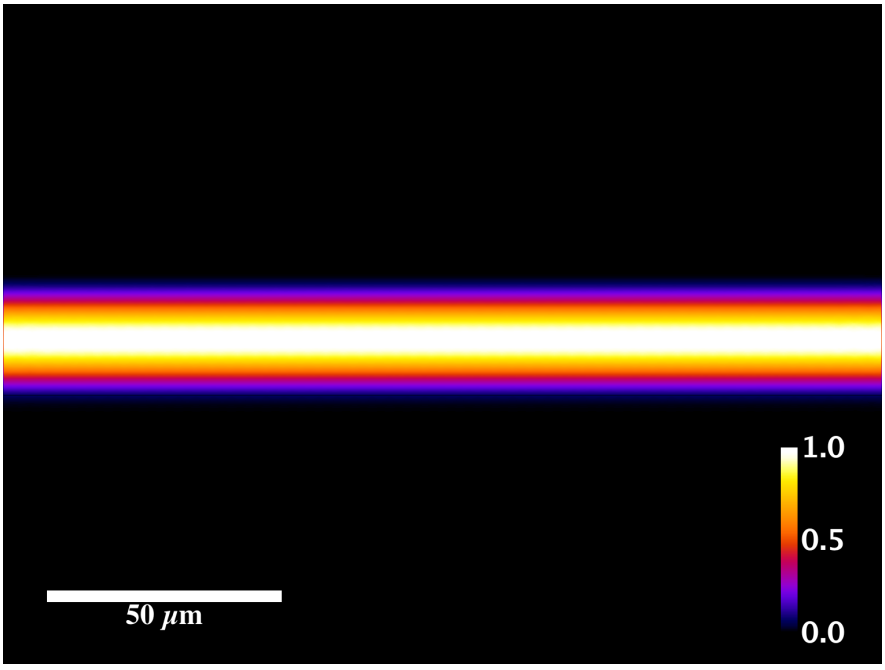

Figure 22. Intensity distribution obtained with a finite-element time-domain simulation assuming a step refractive index increase along the planar waveguide.

With respect to the insertion losses, presented in Table 7 for both waveguides, they were estimated by collecting the output of the waveguide with the coupling experimental setup. Current high losses are attributed to linear optical absorption caused by oxygen vacancies inherent to the sample fabrication, as discussed earlier. Nonetheless, it is possible that these losses can be mitigated by putting the sample through an extended annealing procedure in air or by tuning the fabrication parameters to cause fewer defects (oxygen vacancies).

Table 7**.** Measured insertion losses at $633nm$ of planar waveguides before and after 24 hours of annealing in air for TE and TM polarized incident light.

	1st waveguide		**2nd waveguide**	
	Before	**After**	**Before**	**After**
TE	$27.21 \pm 1dB$	$15.68 \pm 1dB$	$25.91 \pm 0.03dB$	$14.13 \pm 0.03dB$
TM	$29.58 \pm 1dB$	$16.02 \pm 1dB$	$26.75 \pm 0.03dB$	$14.80 \pm 0.03dB$

Assuming a coupling efficiency of unity, calculated Fresnel reflection losses, and taking into account the measured insertion losses, the propagation losses at $633nm$ were found with Equation 9:

$$Propagation\ loss\ (dB/cm) = \frac{L_{in} - \eta - F_{loss}}{d}, \tag{9}$$

$$L_{in}\ (dB) = -10\log(T), \tag{9a}$$

$$\eta\ (dB) = -10\log(overlap\ integral), \tag{9b}$$

$$F_{loss}\ (dB) = -10\log\left(1 - \left(\frac{n_0 - n_1}{n_0 + n_1}\right)^2\right), \tag{9c}$$

where L_{in} is the insertion loss, η is the coupling loss, F_{loss} is the Fresnel loss all in dB, and d is the wavelength length in cm. The results are listed in Table 8. The propagation losses were also measured applying the scattered light imaging method (Wang *et al.*, 2008; Jenkins *et al.*, 2011), giving $11.5dB/cm$ and $9.5dB/cm$ for 633 and $810nm$, respectively; indicating our waveguides are more efficient for longer wavelengths.

Table 8**.** Calculated propagation losses after 24 hours of annealing in air for TE and TM polarized incident light at 633nm.

	633nm
TE	$28.36 \pm 0.03 dB/cm$
TM	$29.84 \pm 0.03 dB/cm$

Regarding the polarization analyses of the planar waveguides, it was found that although the intensity of guided light is polarization dependent, the planar waveguides are able to guide light in either TE or TM polarization. As seen in Figure 23, where the measured power depends only on the polarization of the incident light, the planar waveguides present an anisotropic behavior.

The second analysis was performed by varying the position of the analyzer placed at the output of the waveguides in 10° for every 5° step of the $\lambda/2$ plate placed at the input of the waveguides. It was also found that the waveguides exhibit an anisotropic behavior, as the polarization of incident light is not preserved as it travels through the waveguides. Figures 24 and 25 indicate this behavior is yet more pronounced than that shown in the dependence on only the polarization of the incident light. In both figures, 0° and 90° correspond to TE and TM polarized incident light, respectively.

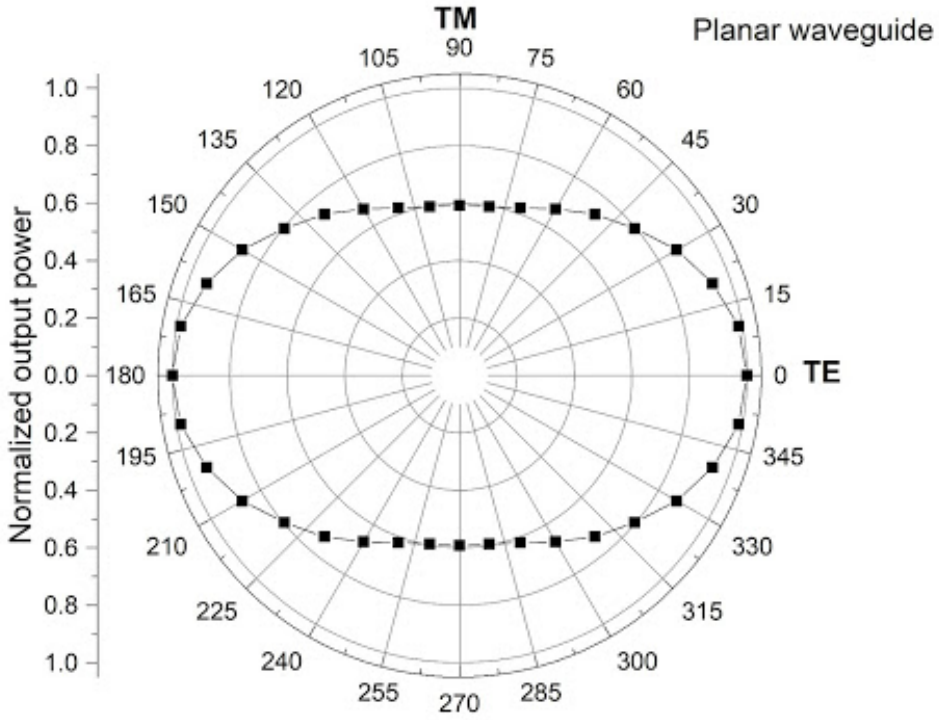

Figure 23**.** Planar waveguide output power (normalized) dependence on the polarization of the incident light at 633*nm*.

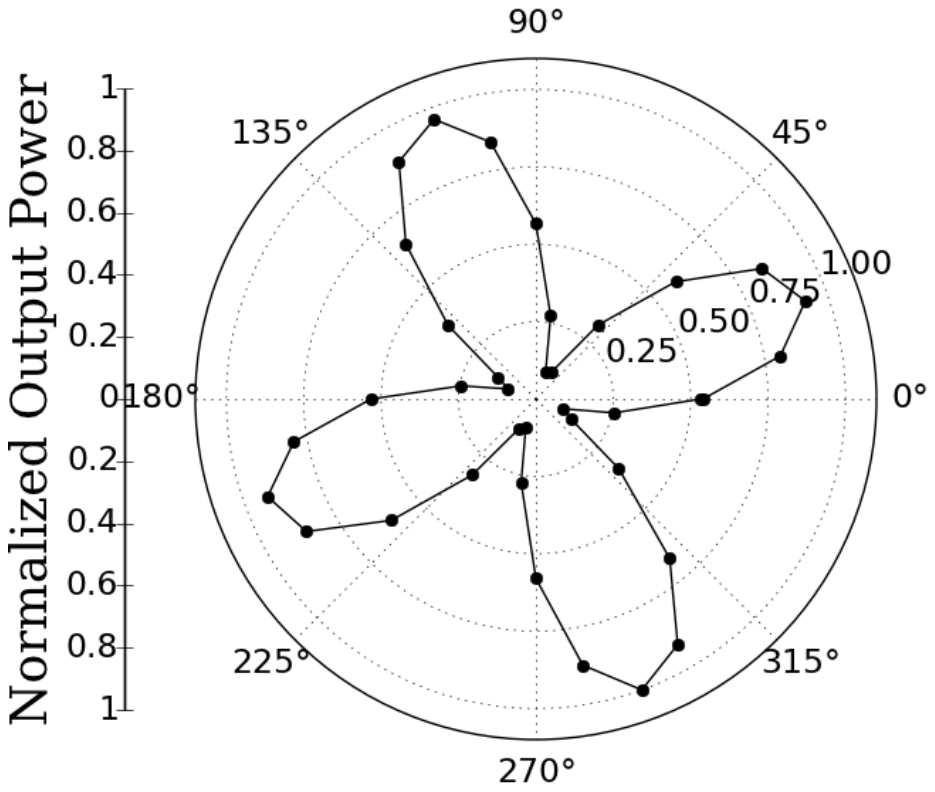

Figure 24**.** Output power (normalized) dependence on the polarization change that incident light suffers through the first planar waveguide at 633*nm*.

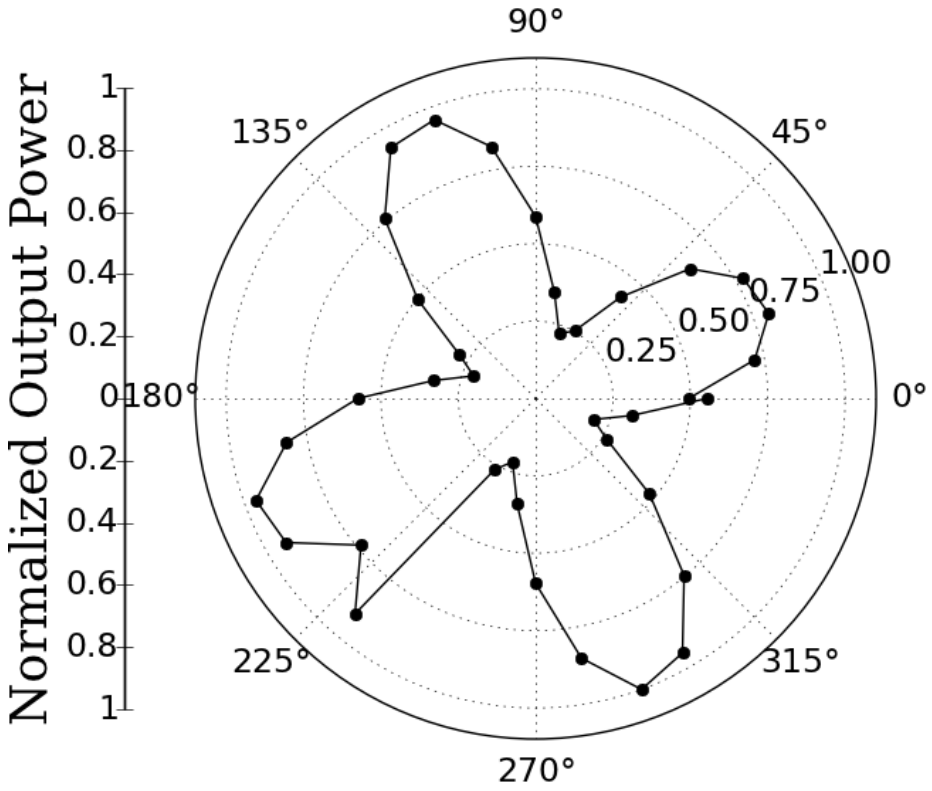

Figure 25**.** Output power (normalized) dependence on the polarization change that incident light suffers through the second planar waveguide at 633*nm*.

In respect of the Raman analysis, to determine whether the laser processing induces chemical phase changes and/or decreased crystallinity, μ-Raman spectroscopy was implemented. Figures 26 and 27 show the Raman spectra for the native nc-YSZ in an unprocessed part of the sample, compared to the collected spectra within the laser written waveguide core before and after annealing, respectively. The spectra are normalized and stacked by an offset for better appreciation, while in the inset figure they are seen without normalization to show the spectrum of the waveguide has an increased intensity. Comparison of these spectra show no significant softening in the Raman breathing modes (F_{2g}, E_{2g}, A_{1g}) for nc-YSZ (Ghosh *et al.*, 2009), which suggest that the laser processing does not induce chemical phase changes. This is expected as nc-YSZ is well known for its chemical stability.

Recently, it was demonstrated that heat treatments up to 700°*C* of depressed cladding waveguides in Lithium Niobate increases the Δn of tracks generated with *fs*-laser pulses (Piromjitpong *et al.*, 2019). Since Δn varies with the annealing temperature, it is suggested the bulk and the modified material act as two different materials

whose dilation coefficients differ from each other. However, for the nc-YSZ case, μ-Raman spectroscopy indicates that *fs*-laser processing does not modify the crystalline structure and hence the bulk material and the guiding region cannot be seen as different materials from a thermal point of view.

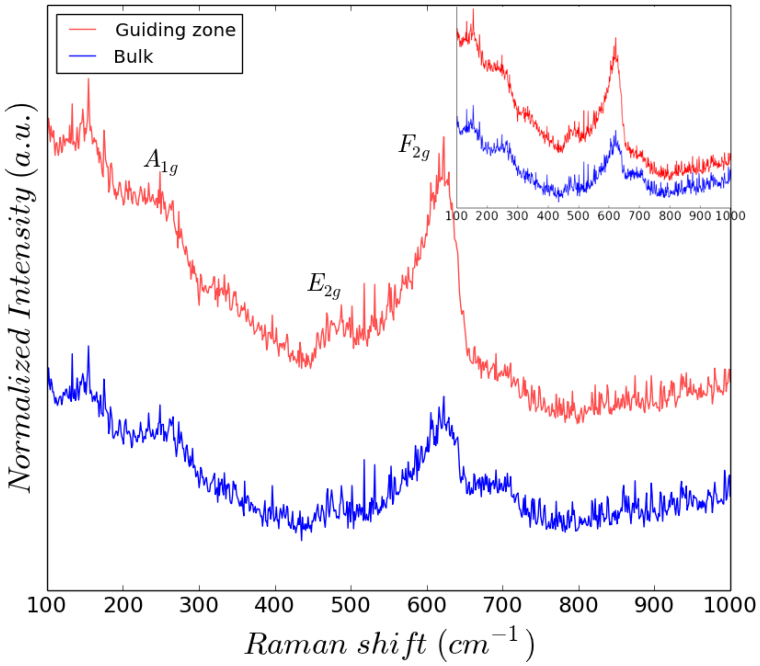

Figure 26. μ-Raman spectra of a planar waveguide in nc-YSZ before annealing.

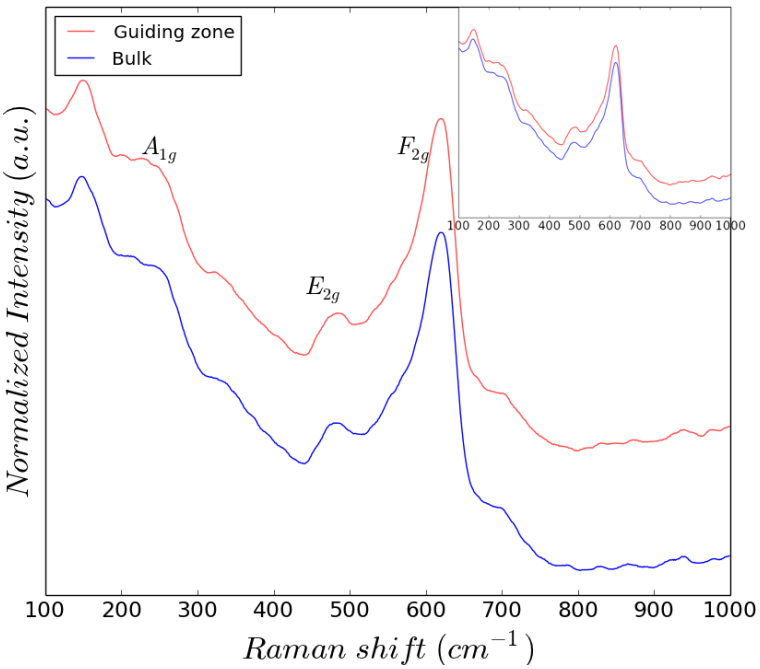

Figure 27. μ-Raman spectra of a planar waveguide in nc-YSZ after annealing.

3.4 Depressed cladding waveguides

Firstly, it is important to point out that, there is a significant difference in the appearance of the nc-YSZ sample after annealing in air. The sample was dark gray color after CAPAD, but became lighter after annealing due to oxygen diffusion into the material, which removes color centers. It is well known for the particular case of nc-YSZ that as the annealing time is increased, its optical transmission increases due to the removal of oxygen vacancy color centers (Alaniz *et al.*, 2009). Transmittance measurements denote that after 24 hours of annealing the transmission of the sample increased by a factor of ten at $633nm$ ($\sim 19\%$), and by a factor of two at $1030nm$ ($\sim 52\%$), as can be quantitatively seen in Figure 16.

About the morphology of the damage tracks caused by laser irradiation in the material were found to be $12\mu m$ long and $0.7\mu m$ wide when produced with $3\mu J$ per pulse; see Figure 28. Higher pulse energy induces more elongated and wider tracks, and a faster scanning speed causes shorter tracks.

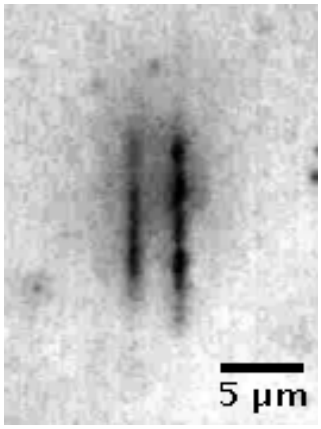

Figure 28**.** Optical micrograph in transmission of damage tracks across the nc-YSZ ceramic.

These modified regions appear as dark, well defined damage tracks with no macroscopic ruptures or fractures neighboring them, and are generated as a result of a non-linear optical process (self-focusing) where the material is optically excited by the transferred pulse energy (Apostolopoulos *et al.*, 2004). In contrast to glasses, where guiding features take place within the irradiated volume after melting and resolidification, crystalline materials have been shown to undergo amorphization and the laser-induced microdamage results in a decrement of the lattice order, or a lower density

region (Gorelik *et al.*, 2003) and therefore a refractive index decrement —recall that free-space, i.e. microvoids or cracks, have a refractive index of 1.

Another possibility to explain refractive index change is that the laser irradiation caused regions with significant residual stress. Balzaretti and da Jornada (1995) have measured the pressure dependence of the refractive index of cubic nc-YSZ and found the following relationship:

$$\frac{1}{n}\frac{\Delta n}{\Delta P} = -1.1 \times 10^{-4} GPa^{-1}, \tag{10}$$

where n is the refractive index of the material, Δn the induced refractive index contrast, and ΔP the pressure change. Δn in these waveguides was estimated to be 9.7×10^{-3} (to be discussed below). Using this and Balzaretti's relationship, it was found that residual stresses of $\sim 4 - 5 GPa$ would be necessary to cause this magnitude of Δn; stress values that are higher than seen in ceramic materials. Therefore, it is likely that other mechanisms are present such as the formation of microvoids/cracks, chemical phase changes, and/or a localized decrease in crystallinity that causes a decreased refractive index in the laser processed regions.

To determine whether the laser processing induces chemical phase changes and/or decreased crystallinity μ-Raman spectroscopy was implemented. Figure 29 shows the Raman spectra for the native nc-YSZ in regions far from any laser processing compared to the collected spectra within a laser damage track and within the waveguide core. The spectra are normalized and stacked by an offset for better appreciation, while in the inset figure they are seen without normalization to show the spectrum of the damage tracks has a decreased intensity. Comparison of these spectra show no significant softening in the Raman breathing modes (F_{2g}, E_{2g}, A_{1g}) for nc-YSZ (Ghosh *et al.*, 2009), which suggest that the laser processing does not induce chemical phase changes. This is expected as nc-YSZ is well known for its chemical stability. Nevertheless, the decreased intensity of the Raman spectra for the observed damaged track zone is lower compared to the intensity of the spectrum of the non-irradiated region. This effect has been observed before in other oxide materials and it has been generally attributed to defect formation and it is indicative of a localized decrease in the

material crystallinity (Silva *et al.*, 2010). It is essential to note here that this decreased intensity of Raman spectra is consistent for all the fabricated cladding waveguides in the present study. These findings support the conjecture that laser induced residual stresses are not solely responsible for the refractive index contrast obtained with laser processing.

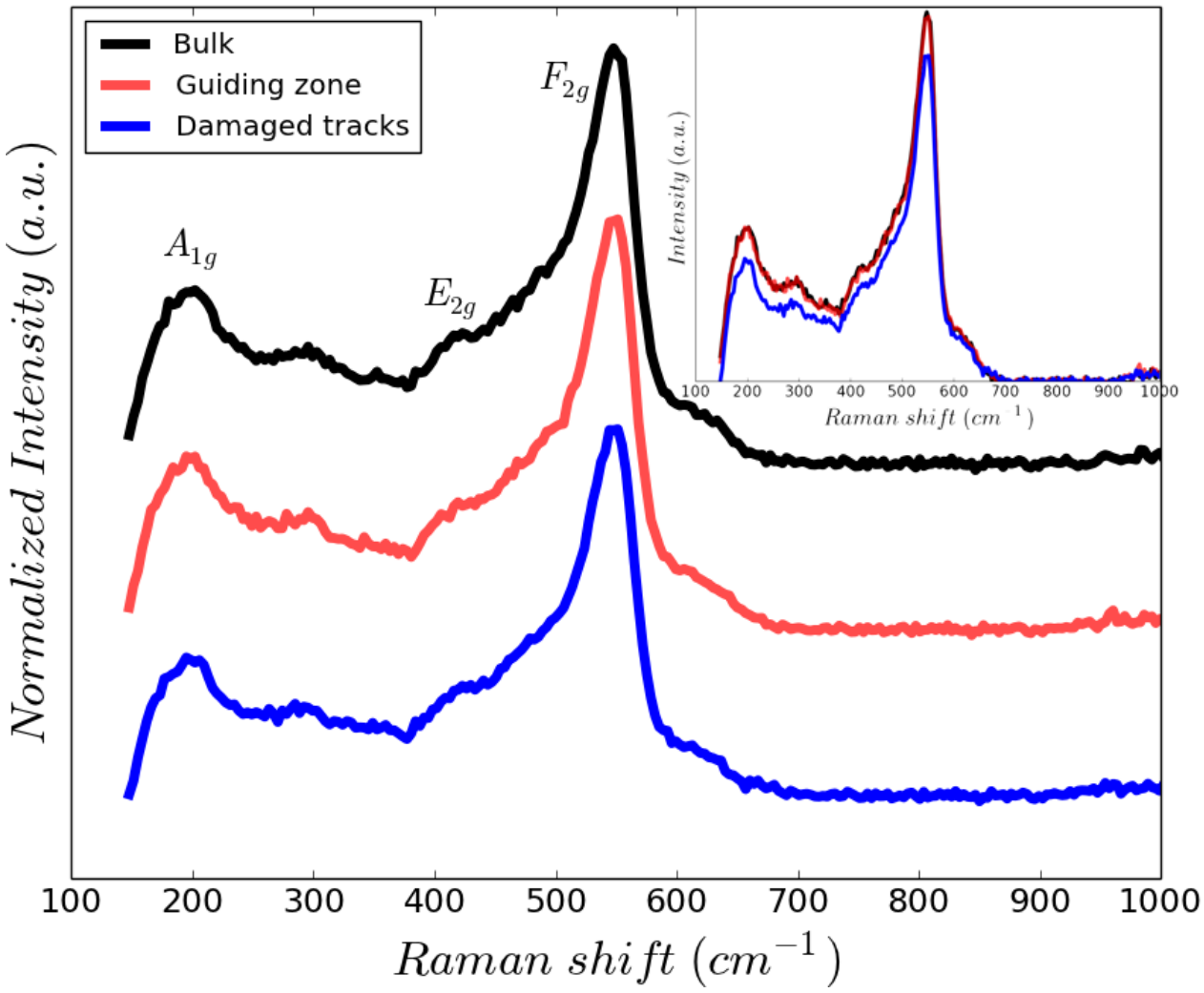

Figure 29. μ-Raman spectra of the discrete cladding waveguide in nc-YSZ.

Optical transmission microscope images of the waveguides cross sections written at the threshold energy of 3μJ are depicted in Figure 30. In this depressed cladding configuration, light is guided by the unprocessed region surrounded by the inscribed tracks with a lower refractive index (Okhrimchuk *et al.*, 2005).

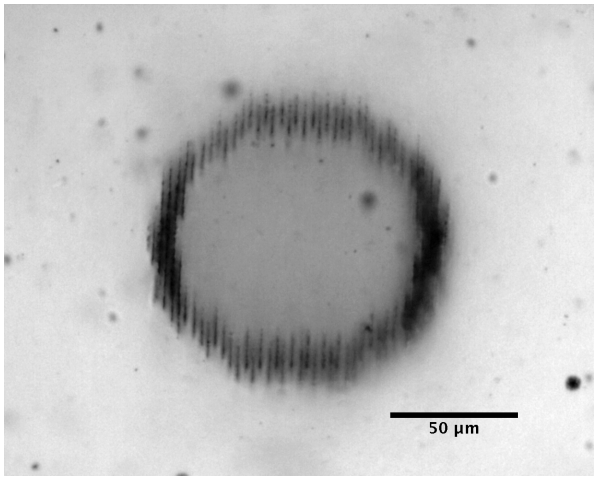

(a) Optical micrograph of the classically written waveguide.

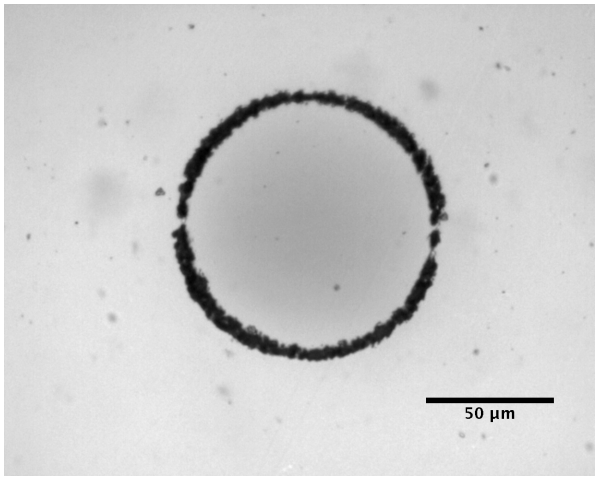

(b) Optical micrograph of the continuous waveguide.

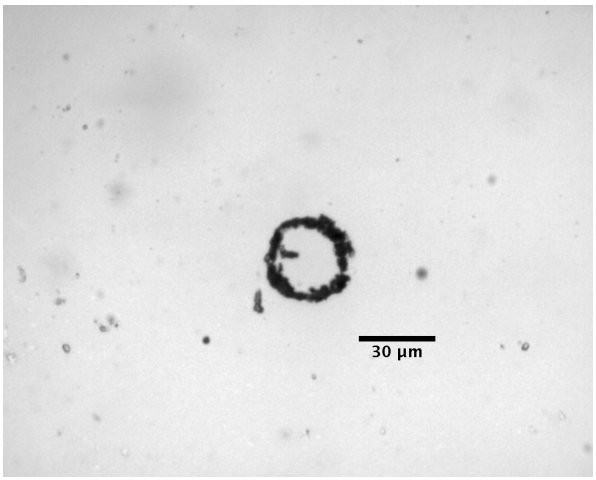

(c) Optical micrograph of the small continuous waveguide.

Figure 30**.** Optical micrographs in transmission of the depressed cladding waveguides cross sections in nc-YSZ ceramic.

Concerning the wave-guiding properties of the fabricated waveguides, end-face viewing setup reveals that the near field intensity distributions are true to shape and size of the waveguides boundaries, which indicates a good optical confinement of the written structures.

On the one hand, the waveguide written with a discrete cladding displays a circular striped propagation mode; while for the case of the continuous circular cladding waveguides concentric rings shaped modes are propagated. Figures 31, 32, and 33

show the guided TE and TM spatial propagating modes at 633nm of the depressed cladding waveguides in nc-YSZ ceramic, and the supported modes at 1568nm, respectively. All three waveguides support TE and TM spatial modes, and they appear exactly the same. This points out that light confinement is polarization independent, as it could be expected because of the circular geometry of the inscribed waveguides and because the centrosymmetric nc-YSZ crystal lattice results in isotropic optical properties.

While the discrete cladding waveguide presents a stripped propagating mode, the 100μm core continuous waveguide propagates a high-order single transverse mode, as observed in large mode area (LMA) optical fibers (Ramachandran *et al.*, 2006). Large guiding regions have been explored as a good option for photonic applications, such as sensing and spectrometry, in particular for applications in the infrared (Stoian *et al.*, 2016). Conversely, the smaller core continuous waveguide allows propagation of a lower order mode.

These differences are valid for both coupled wavelengths, being $\lambda = 1568nm$ the one propagating modes with fewer stripes and circles for the discrete and continuous cases, respectively. Furthermore, the possibility of coupling wavelengths in the IR range where nc-YSZ ceramics are more transparent and the propagation losses are smaller (discussed below), is promising for uses in telecommunications and bioapplications. Waveguiding in the IR is important as it opens the possibility for developing “eye-safe" devices (Ter Gabrielyan *et al.*, 2008) near 1.5μm and takes advantage of the higher transparency of the nc-YSZ ceramics in this region of the optical spectrum, resulting in lower propagation losses.

With regard to the insertion losses, presented in Tables 9 and 10, those were estimated by collecting the output of the waveguides with the coupling experimental setup. The propagation losses are attributed to linear optical absorption caused by oxygen vacancies inherent to the sample fabrication, as discussed earlier. It is possible that these losses can be mitigated by subjecting the sample to an extended annealing procedure in air or by tuning the fabrication parameters to cause fewer defects (oxygen vacancies). While these losses are high for optical communications applications, they are acceptable for unconventional applications as the WttB platform and others as discussed above.

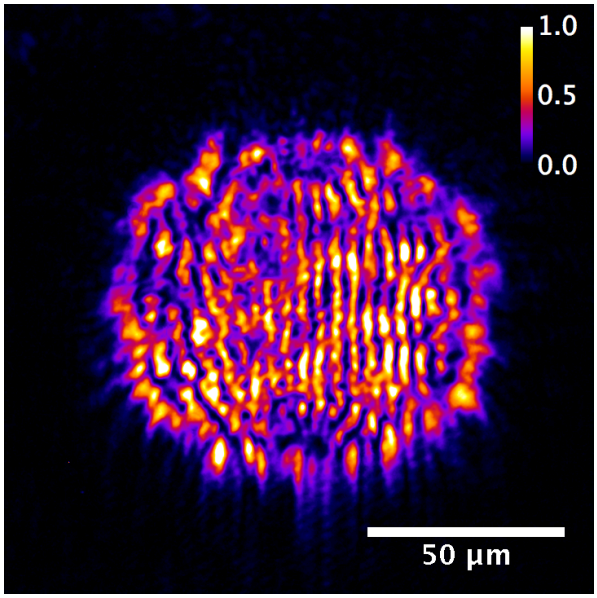

(a) Discrete cladding with $\varnothing = 100\mu m$.

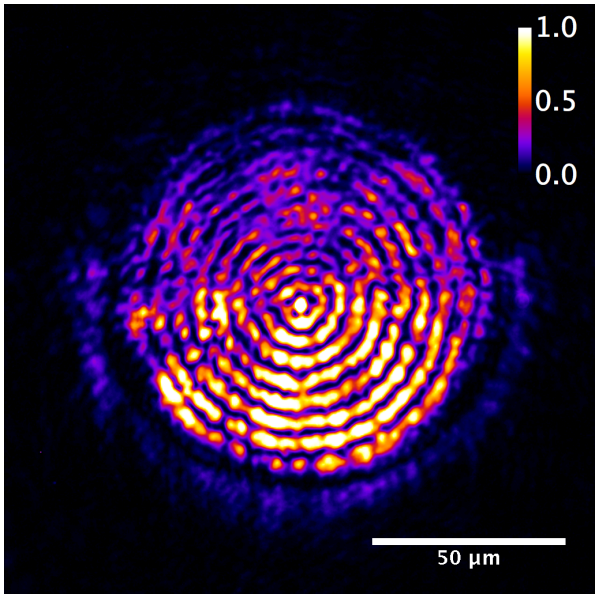

(b) Continuous cladding with $\varnothing = 100\mu m$.

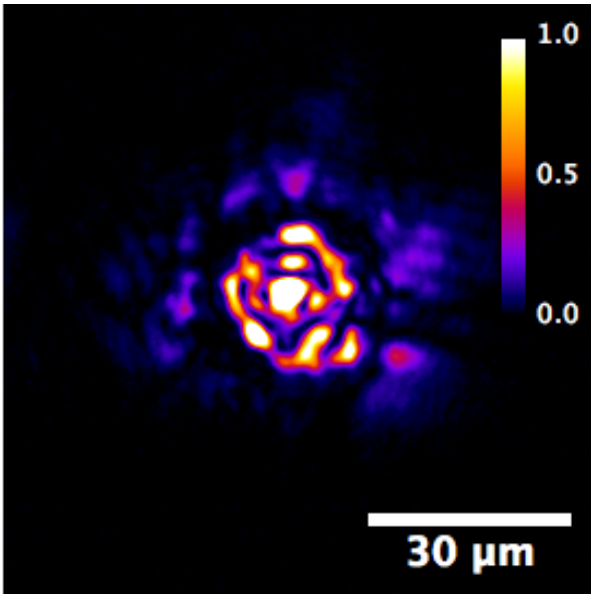

(c) Continuous cladding with $\varnothing = 30\mu m$.

Figure 31**.** Propagating modes at 633*nm* of the depressed cladding waveguides in nc-YSZ ceramic for vertically polarized incident light.

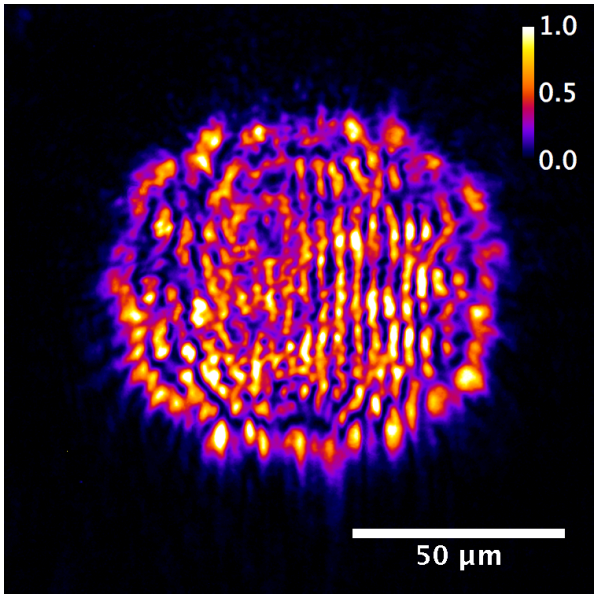

(a) Discrete cladding with $\varnothing = 100\mu m$.

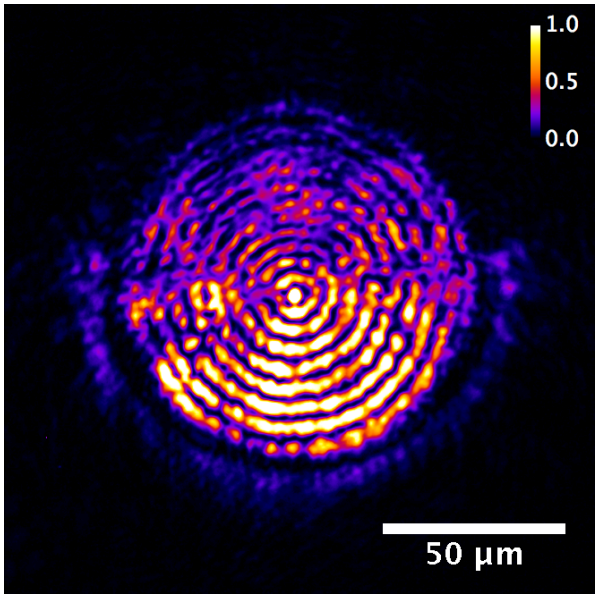

(b) Continuous cladding with $\varnothing = 100\mu m$.

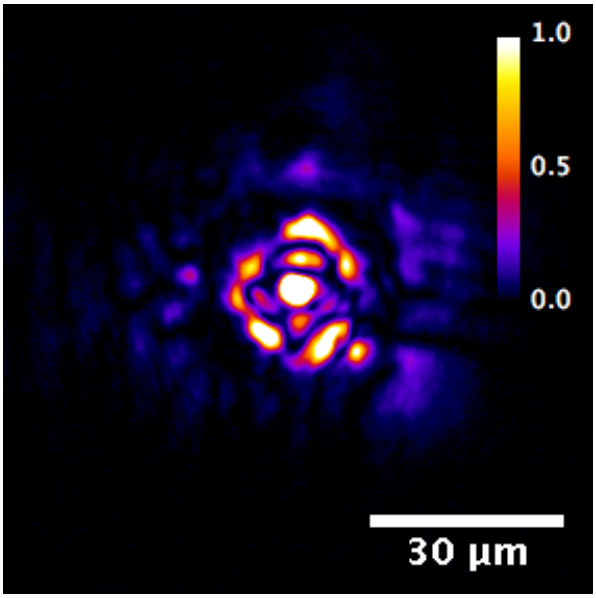

(c) Continuous cladding with $\varnothing = 30\mu m$.

Figure 32. Propagating modes at $633nm$ of the depressed cladding waveguides in nc-YSZ ceramic for horizontally polarized light.

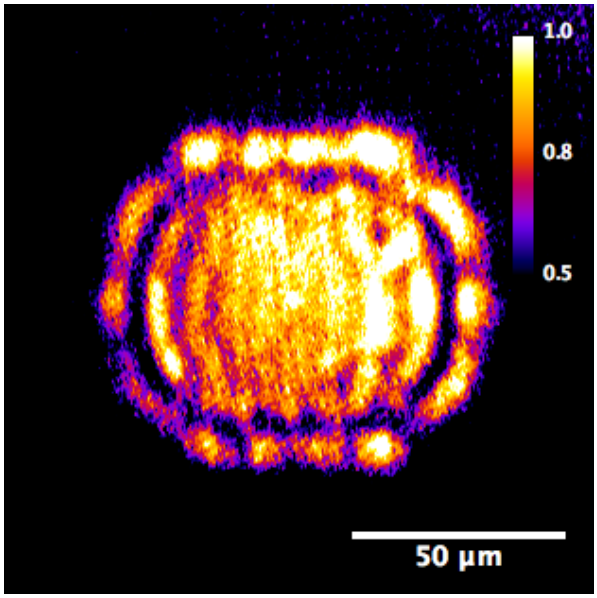

(a) Discrete cladding with $\varnothing = 100\mu m$.

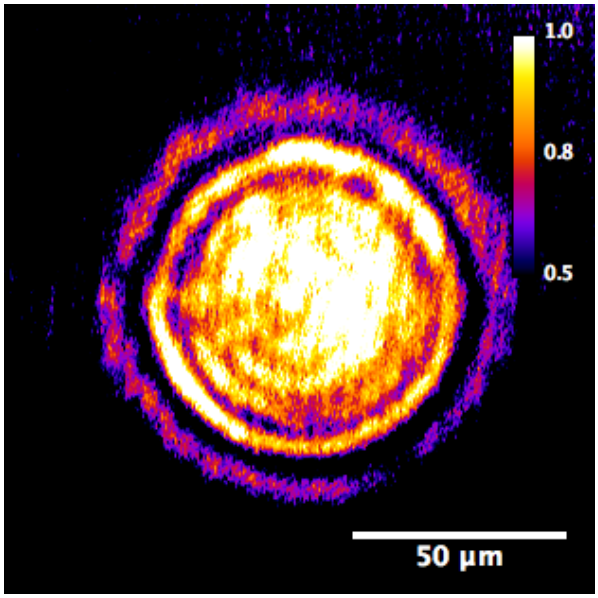

(b) Continuous cladding with $\varnothing = 100\mu m$.

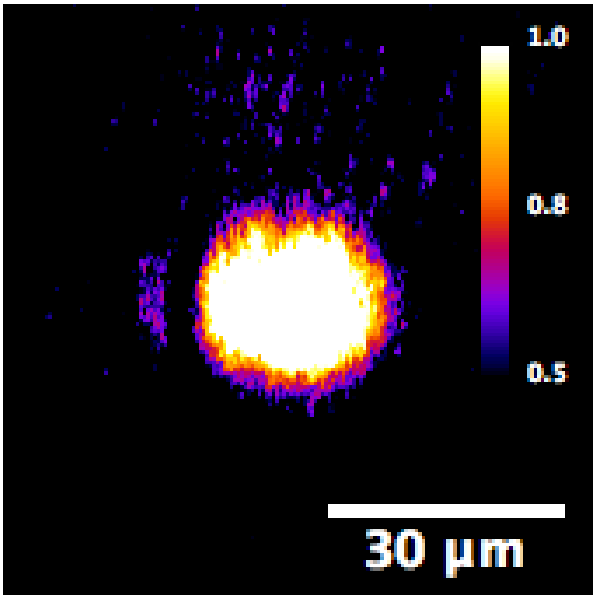

(c) Continuous cladding with $\varnothing = 30\mu m$.

Figure 33**.** Propagating modes at 1568*nm* of the depressed cladding waveguides in nc-YSZ ceramic.

Table 9. Measured insertion losses for horizontally and vertically polarized incident light modes at $\lambda = 633nm$. A = Discrete cladding with $\varnothing = 100\mu m$, B = Continuous cladding with $\varnothing = 100\mu m$, and C = Continuous cladding with $\varnothing = 30\mu m$.

	Horizontal	**Vertical**
A	$8.67 \pm 0.03dB$	$8.75 \pm 0.03dB$
B	$8.48 \pm 0.03dB$	$8.56 \pm 0.03dB$
C	$9.03 \pm 0.04dB$	$9.07 \pm 0.04dB$

Table 10. Measured insertion losses at $1568nm$. A = Discrete cladding with $\varnothing = 100\mu m$, B = Continuous cladding with $\varnothing = 100\mu m$, and C = Continuous cladding with $\varnothing = 30\mu m$.

	Insertion loss
A	$1.96 \pm 0.11dB$
B	$1.96 \pm 0.11dB$
C	$2.34 \pm 0.14dB$

Additionally, a second nc-YSZ sample with $2mm$ in length was used to inscribe discrete and continuous waveguides with $\varnothing = 100\mu m$ to verify the near field modes in Figures 31 and 33 are not generated from diffraction of the damaged traces. In this case, optical characterization was performed using $\lambda = 810nm$ and, as before, the stripped and circular propagating modes were replicated. Propagation losses were measured in both of them applying the scattered light imaging method (Wang *et al.*, 2008; Jenkins *et al.*, 2011), giving $37.8 \pm 0.1dB/cm$ for the discrete waveguide and $26.3 \pm 0.1dB/cm$ for the continuous one; indicating the continuous cladding waveguides are more efficient. This is consistent with previous results reported for similar waveguides (Salamu *et al.*, 2014a; Peng *et al.*, 2015).

In order to verify that the propagating modes are preserved over longer distances, another discrete cladding waveguide with $\varnothing = 100\mu m$ was inscribed but along a different direction of the sample, which is $7.2mm$ long. The stripes present in the $0.8mm$ long discrete waveguide were also seen in this one, corroborating the images taken at the end-face correspond to coupled and guided light.

Regarding the polarization analysis of the waveguides, pictured in Figure 34 for the discrete waveguide, it was found they exhibit an isotropic behavior, showing the polarization of incident light is preserved; results are similar for the three cladding waveguides. The dots in the polar map correspond to measured power at the output face of the waveguide after having passed through the analyzer for every input polarization angle, normalized to the maximum output value, and 0° corresponds to TE polarization.

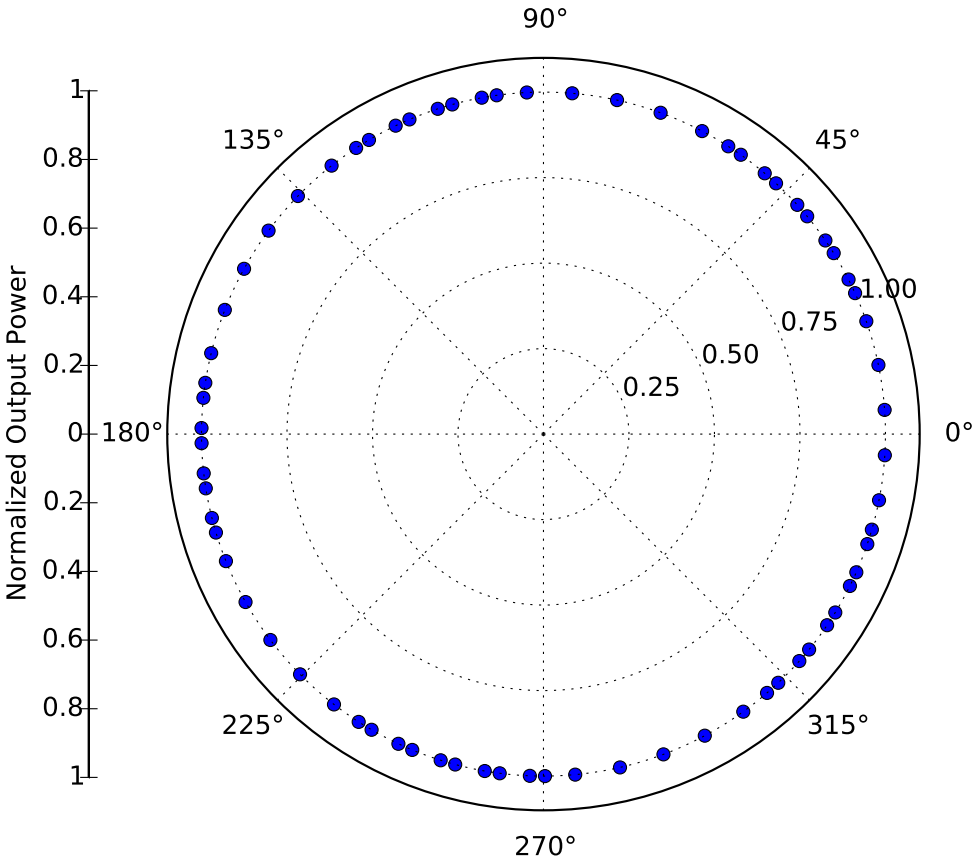

Figure 34**.** Output power (normalized) dependence on the polarization change that incident light suffers through the discrete written cladding waveguide at 633*nm*.

Concerning the refractive index contrast between the undamaged region and the irradiated zone, 9.7×10^{-3} at 633*nm* was obtained for the continuous waveguide. This value was determined by experimentally measuring the numerical aperture of the waveguide and using the Equation 11 (Castillo *et al.*, 2017):

$$\Delta n = \frac{\sin^2 \theta_m}{2n}, \tag{11}$$

where θ_m is the maximum incident angle at which the transmitted power occurs without significant changes, while n is the refractive index of the bulk material. It should be pointed out that, in this case, Δn was estimated under the assumption of a step index profile of the waveguide, however, the magnitude is in good agreement with previously reported Δn in ceramic materials (Siebenmorgen *et al.*, 2009; Okhrimchuk *et al.*, 2005; Ródenas *et al.*, 2009; Liu *et al.*, 2012).

To better understand the cladding waveguides, a finite-difference time-domain method was applied to quantify the refractive index contrast (Δn) of the depressed cladding waveguides relative to a $n = 2.2$ of the bulk material. This was accomplished so by using the experimentally obtained Δn and corroborating how the resulting propagating spatial mode goes in accordance with the measured one. Figure 35 shows the simulated propagating mode for vertically polarized incident light at $633nm$ for the continuous cladding waveguide. By directly comparing this figure with Figure 31(b), it is possible to observe a good agreement between the simulated and the experimentally measured mode. From this, it can be concluded that the experimentally determined Δn used for the reconstruction of the refractive index contrast profile of the waveguide, which is the one experimentally determined, leads to the same shape of the propagating mode, validating the experimental measurements.

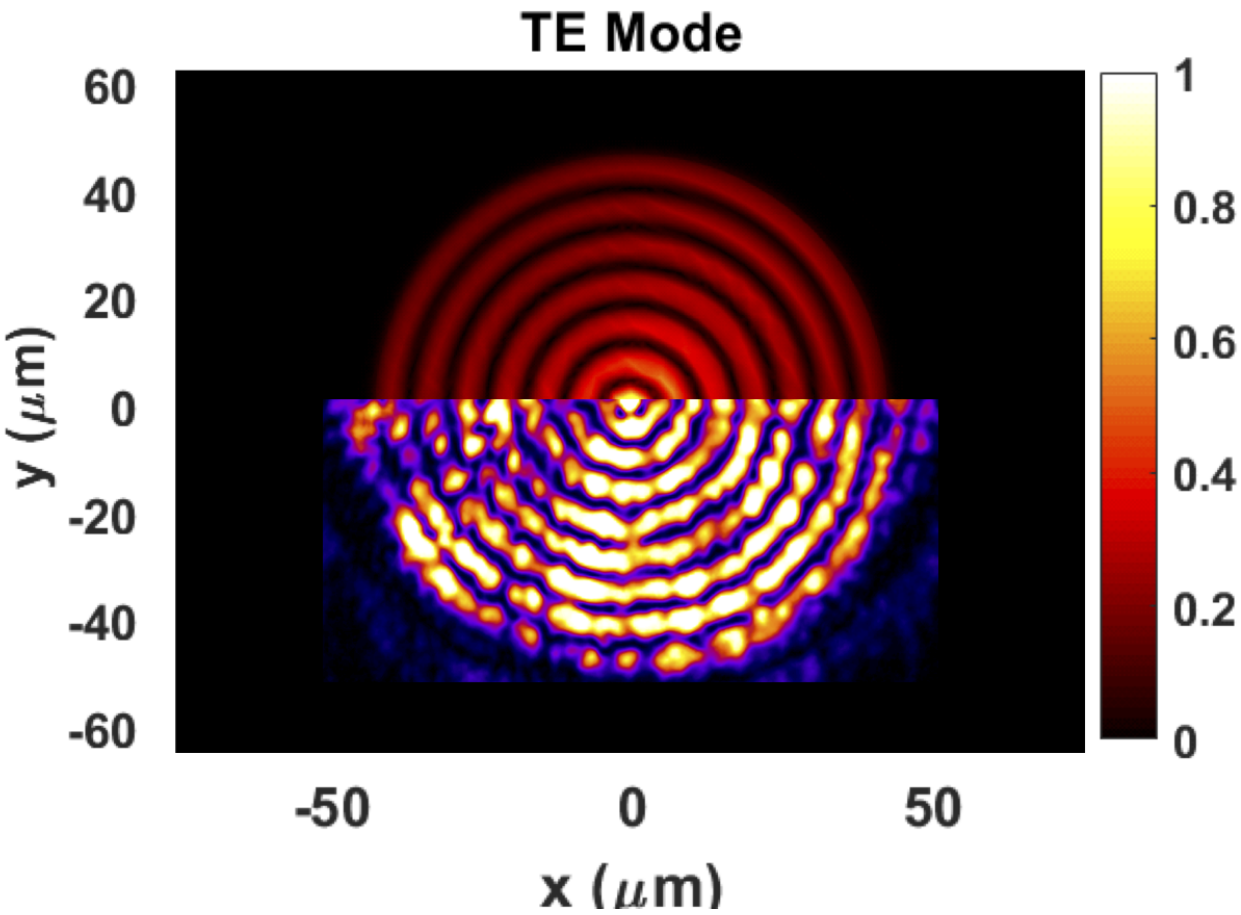

Figure 35. Calculated modal profile of circular continuous waveguide at 633*nm* with a superposition of the measured modal profile at the same wavelength.

For the purpose of liken the optical characteristics of the circular cladding structures, direct comparison with a double line waveguide previously fabricated through Type II modification (Castillo, 2017) was performed. It is worth noting that in double line waveguides, besides the laser-induced negative refractive index changes in the directly irradiated region, the regions surrounding damage tracks may possess a relatively high index through the stress-induced effects caused by the expansion of the lattices in the focal volume (Chen and de Aldana, 2014).

For the fabrication of the double line waveguide, parallel tracks separated by 15μm were inscribed to form a 2.2*mm* long waveguide. The sample was translated perpendicularly to the laser beam. Figure 36 shows a near-field image of the mode at 633*nm* for the double line waveguide, which portrays a single-mode behavior. The insertion loss in the double line waveguide was found to be 21.2*dB*, while its propagation loss is about 50*dB/cm* at 633*nm* —both of them were measured with the method described above.

Comparing these values with those obtained for the circular cladding waveguides, it can be seen there are no major differences between the losses of the different configurations. Further, the double line waveguide has even higher losses.

Ultimately, these results suggest that the discrete and continuous cladding waveguide structures are superior designs as they also support single mode operation but with significantly improved losses. While it is clear that for traditional optocommunications applications, these insertion and propagation losses are high, for extreme applications such as biomedical photonics technologies, they are acceptable as the chemical, mechanical, and biocompatibility properties take precedence and traditional materials do not meet functional requirements. Also, propagation losses can be lowered by either further post *fs*-laser processing annealing or by tuning the nc-YSZ ceramic synthesis parameters to minimize oxygen vacancies.

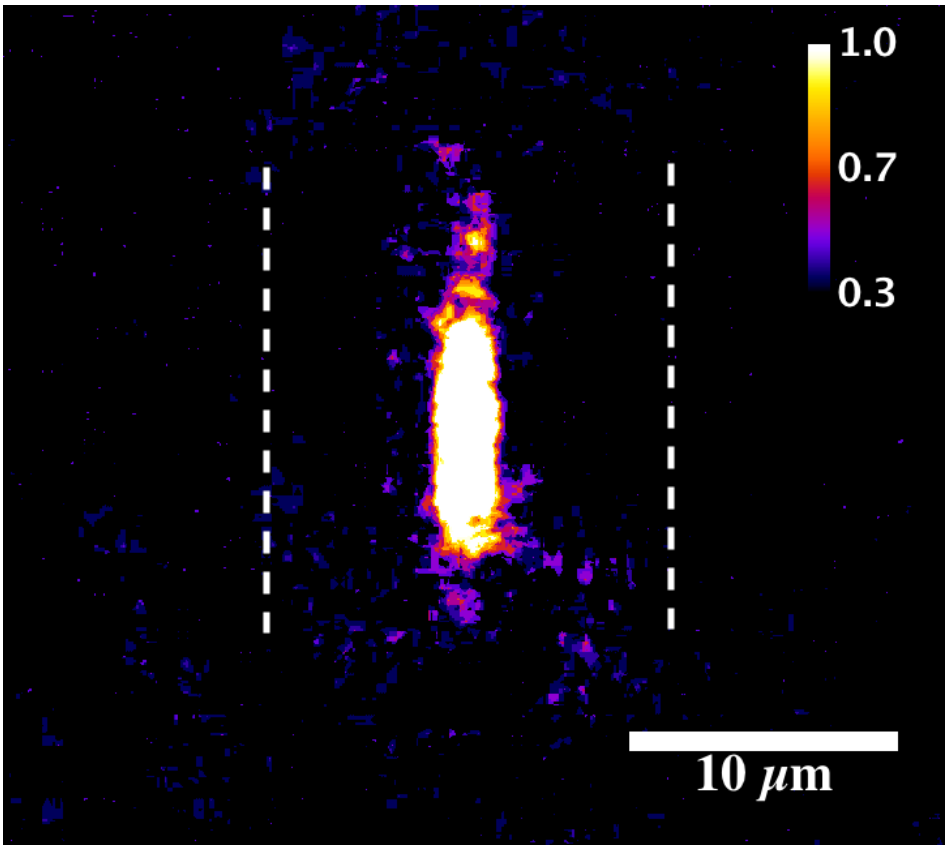

Figure 36. Near-field image of the double line waveguide propagating at 633*nm*. The dashed lines indicated the position of the damage tracks (Castillo, 2017).

3.5 Bacterial inactivation

As mentioned in Section 2.6, bacterial experiments begun with understanding the normal growth or cell division rate of *E. coli* cells. Figure 37 illustrates the rate at which three different samples change their OD600 value (meaning the amount of cells) with time. The initial OD600 values were 0.061, 0.040, and 0.060 for samples 1, 2, and 3, respectively.

It can also be seen that after $12 hours$ of incubation, the samples have reached what is known as *stationary phase*, where cell division cannot longer take place usually because of a lack of nutrients –on the curve, this is identified by the fourth slope or the region from 9 to $12 hours$. The medium slopes ($2-6 and 6-9 hours$) represents the *log phase*, named after the exponential growth of the cells during this period. The first slope ($0-2 hours$) is the *lag phase*, where most of the initial inoculated cells are not fully grown yet and hence cell division has not started (Zwietering *et al.*, 1990).

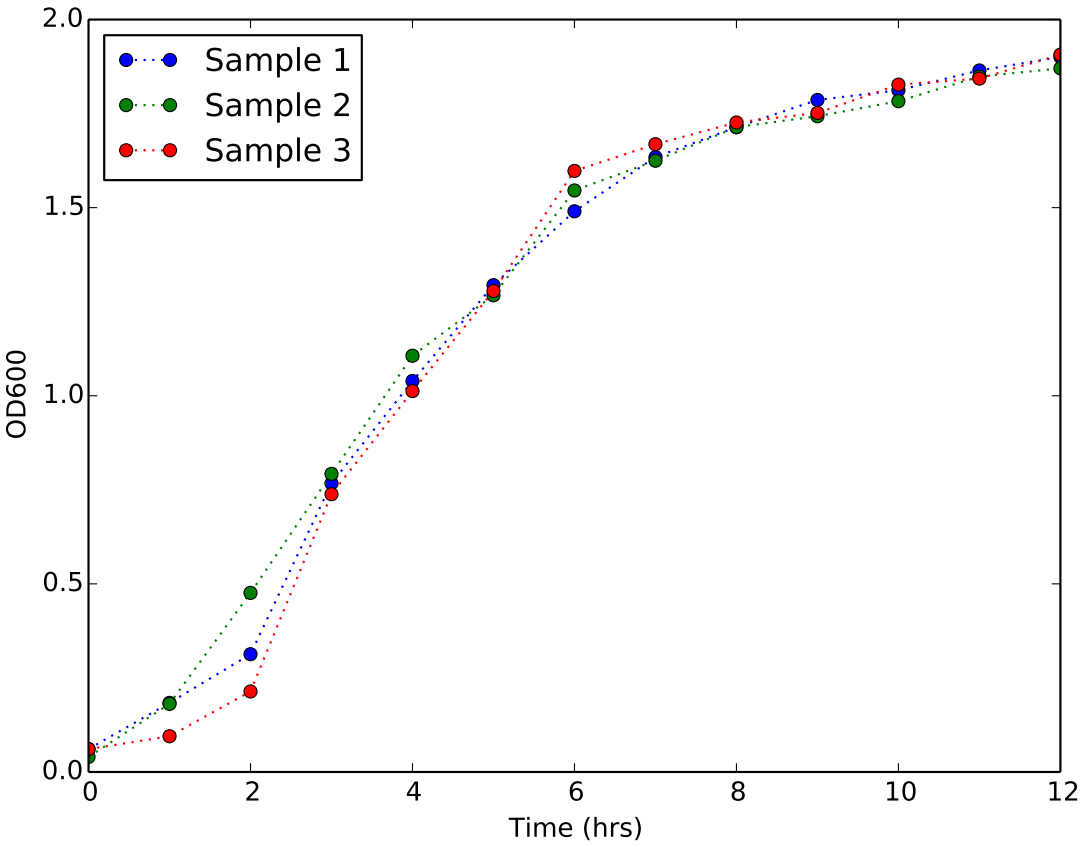

Figure 37. *E. coli* curve of growth in liquid LB broth at 37°*C*.

Figure 38 shows the *E. coli* absorbance spectrum in the visible range. It is clear that at the treatment wavelength, illustrated as a red mark in the plot, the absorbance is almost at its lowest value. The latter has been reported to occur at around 920*nm* (Quigley, 2008). This result points out there should not be significant laser-induced heating within the bacteria when treated with 810*nm*.

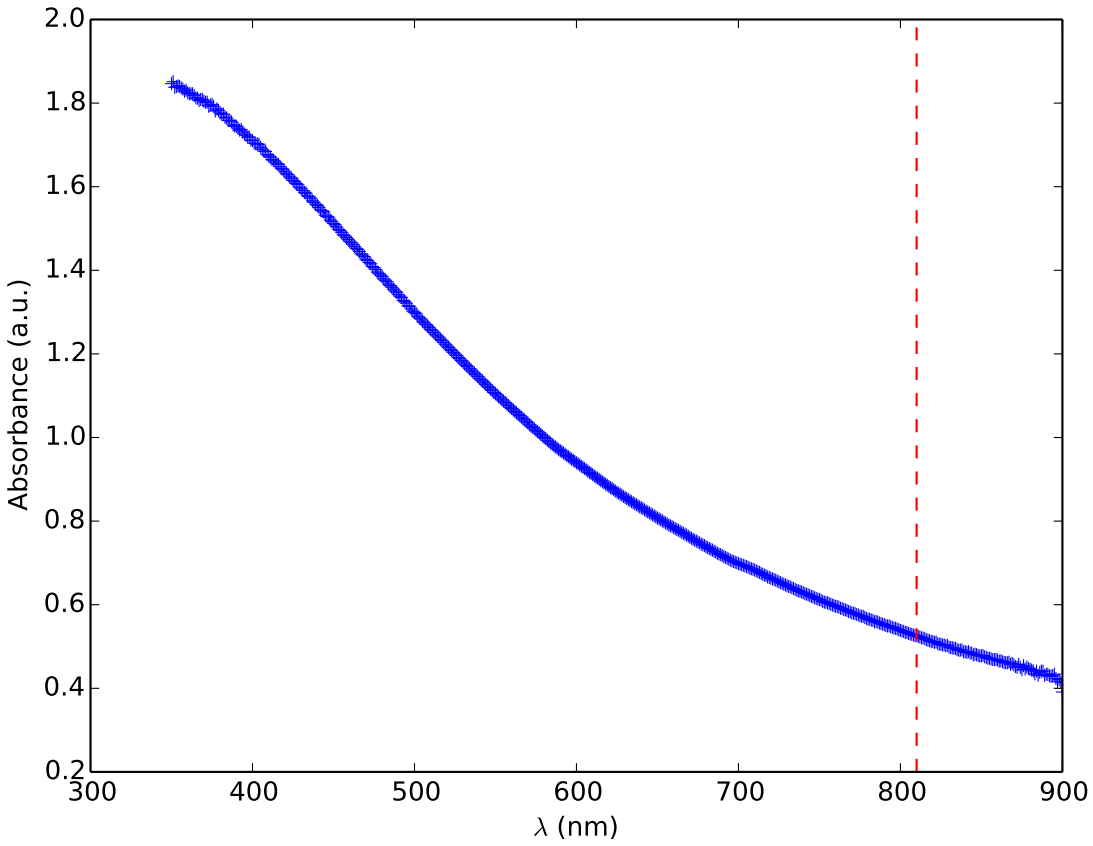

Figure 38**.** *E. coli* absorbance spectrum in the visible range.

The density of samples, measured in number of cells per unit volume, was varied from 0.03 to 0.25 OD600, and then they were irradiated from minutes to hours. This practice allows to find the optimum combination of treated cells per time, since the hypothesis for direct *fs*-laser bacteria inactivation resides in how many cells are being targeted by a laser pulse. The selected OD600 was ~ 0.08 for irradiation times ranging from $0.5 hours$ to $3.5 hours$, and with pulsed laser average power from 100 to $\sim 350 mW$. This results in energy and fluence per pulse variations from 1.12 to $3.93 nJ$ and from 0.71 to $2.51 \mu J$, respectively.

An initial control plate is depicted in Figure 39. The upper side of the plate corresponds to $10\mu L$ of a certain sample, while the lower part corresponds to $10\mu L$ of the same sample but diluted by a factor of 100. The difference in size of the colonies is caused by the amount of nutrients and physical space that each colony, and hence each cell, has access to.

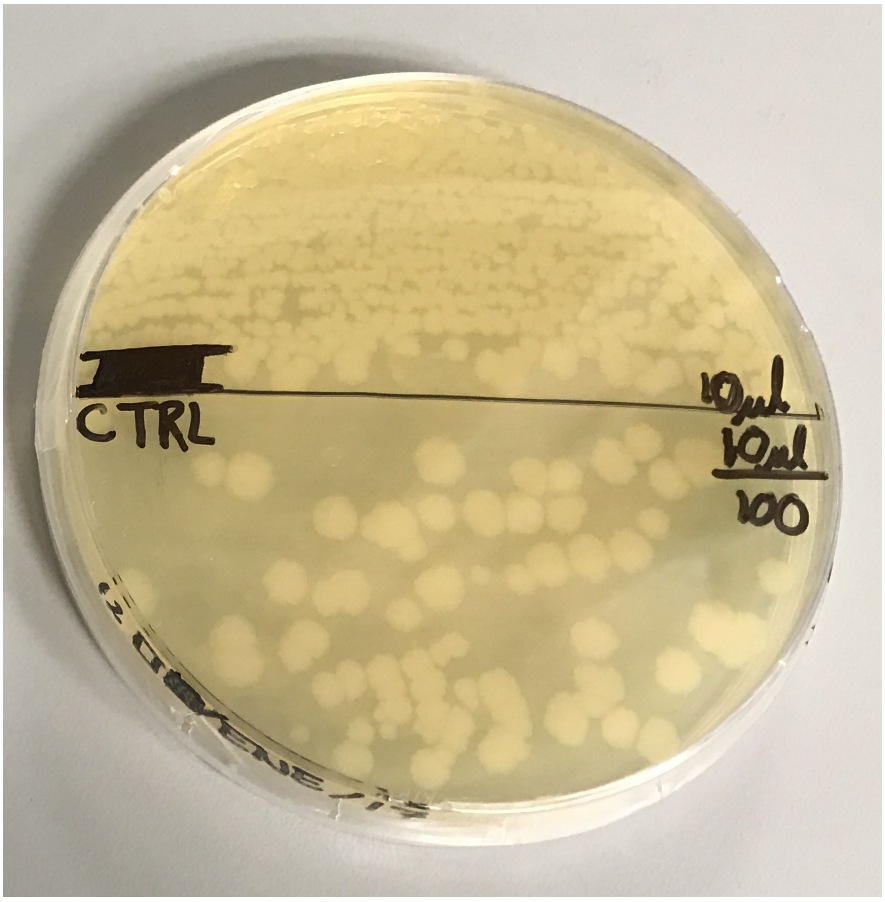

Figure 39. *E. coli* control plate containing one as prepared control and one diluted by a factor of 100.

Thermal imaging (see Figure 40) indicates that samples go from $\sim 24.2°C$ to a maximum of $\sim 38.3°C$ during treatment with the $810nm$ *fs*-laser treatment, whereas controls reach a maximum of $\sim 26.5°C$. The small difference in temperature changes strongly imply that heating is not being induced by the *fs*-laser treatment and thus does not interfere with the bacteria growing or survival rate post-treatment.

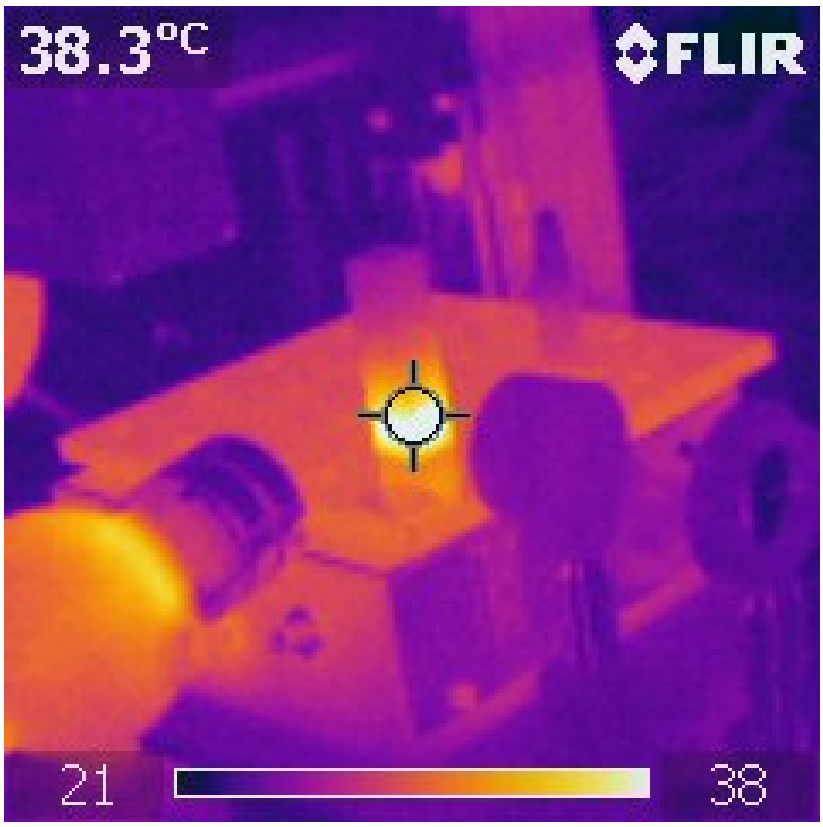

Figure 40**.** Thermal monitoring of an *E. coli* sample during 810*nm fs*-laser treatment.

A temperature of 38°*C* is still considered ideal for *E. coli* proper growth, whereas temperatures higher than ∼ 43°*C* are considered survival threatening. Furthermore, laser-induced heating of the samples from 26°*C* to 38°*C*, should be beneficial for bacteria replication.

Treatment at 1030*nm* could not be performed because of the high temperatures reached owing to the distilled water absorption at such wavelength. Figure 41 reveals a temperature higher than 44°*C* is reached in less than 5*minutes*.

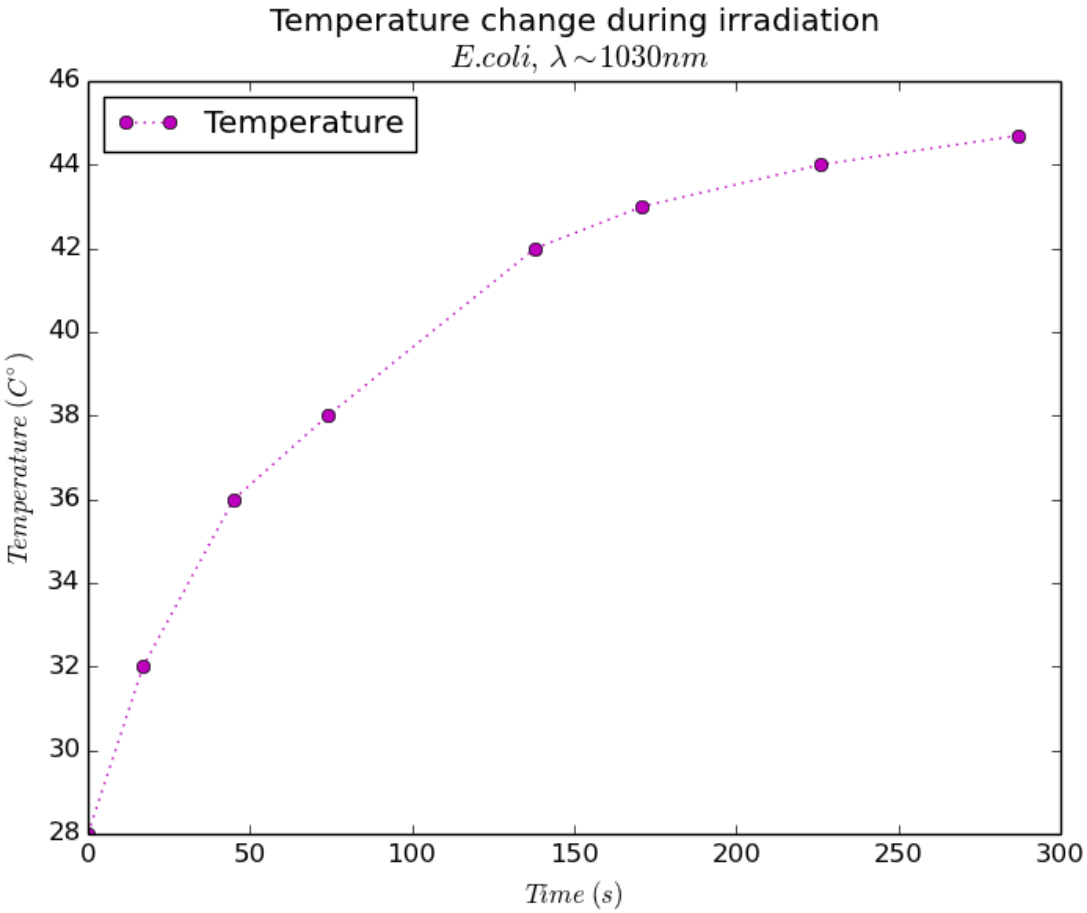

Figure 41**.** Thermal monitoring of an *E. coli* sample during 1030*nm fs*-laser treatment.

Damage assessment conducted by cell counting showed there are inactivation when bacteria is treated with the 810*nm fs*-laser, but not at all when the 532*nm ns*-laser is used. The succeeding results and discussions make all reference to treatment at 810*nm*. Figure 42(a) is an example of a plate where an irradiated sample (right) and its control (left) were inoculated, and where a partial inactivation is evident because of the smaller number of colonies on the treatment plate.

On the other hand, total inactivation is declared when there is not even a colony on the treatment plate. This is illustrated in Figure 42(b), where 100μL of a sample and its control were inoculated. Figure 42(c) shows the result of inoculating 10μL of the same sample and control but diluted by a factor of 100. Dilutions by different factors help to demonstrate consistency of the results, while making cell counting easier and faster.

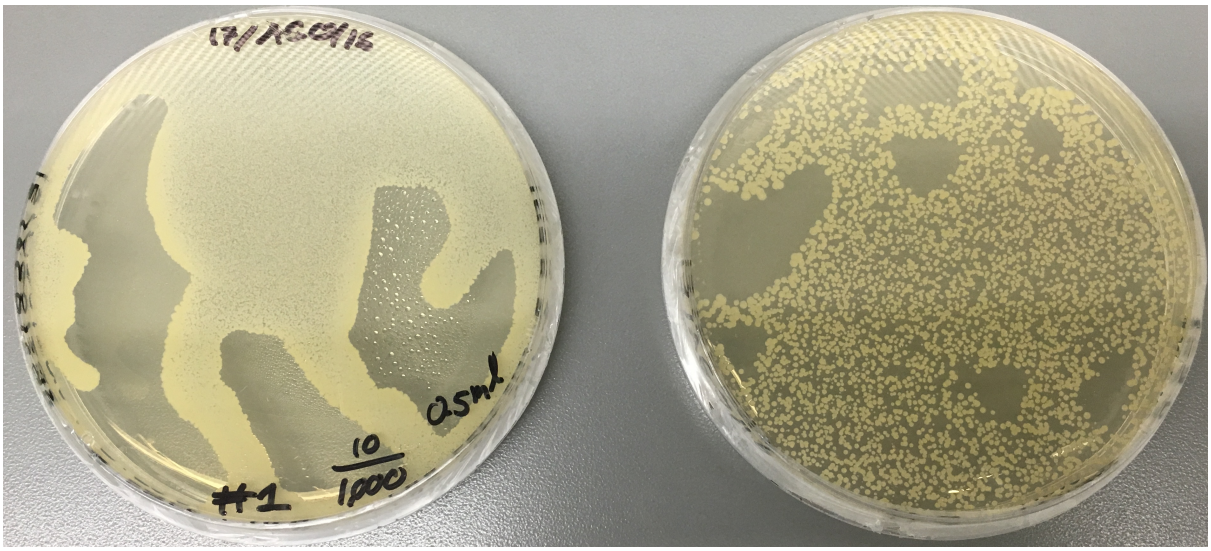

(a) Partial inactivation.

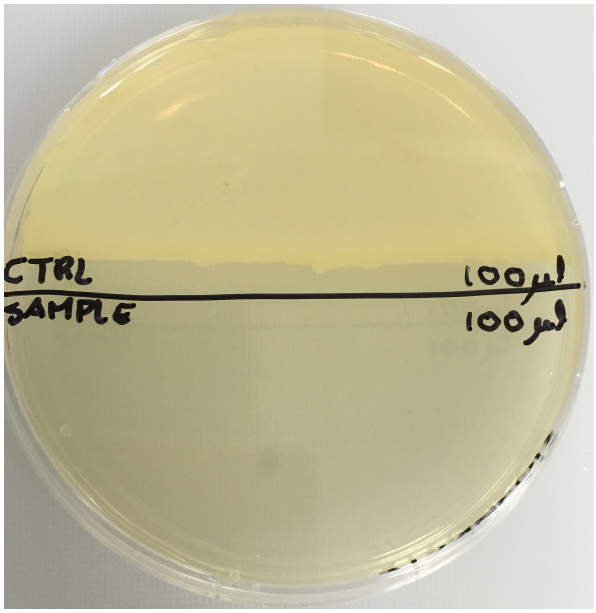

(b) Total inactivation.

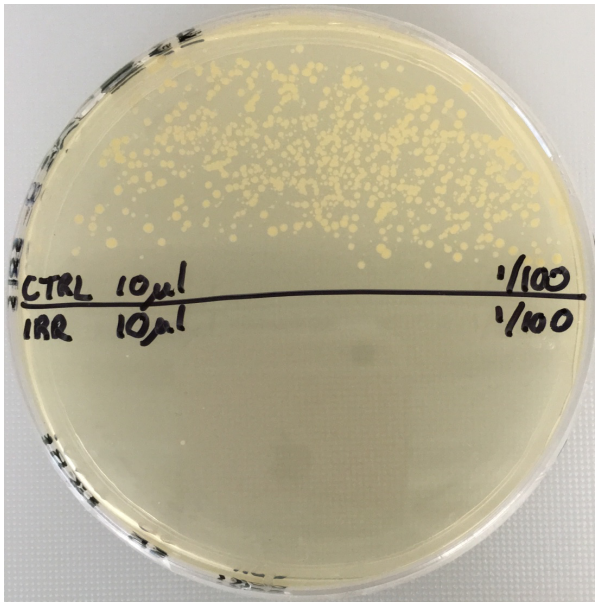

(c) Total inactivation diluted by a factor of 100.

Figure 42**.** Petri dishes for damage assessment of *E. coli* treated with 810*nm*.

For the laser treatment at $810nm$, a $7\log_{10} CFU$ reduction, which is by far more than the previously reported $\sim 2.5\log_{10} CFU$ with a similar technique (Tsen *et al.*, 2007), was observed when irradiations were performed using an average power of $350mW$ during $2.5hours$ but not less, as depicted in Figure 43; this is equivalent to a total inactivation of cells. It was also observed that the average power can be reduced down to $200mW$ whilst keeping such effectiveness; this can be seen in Figure 44.

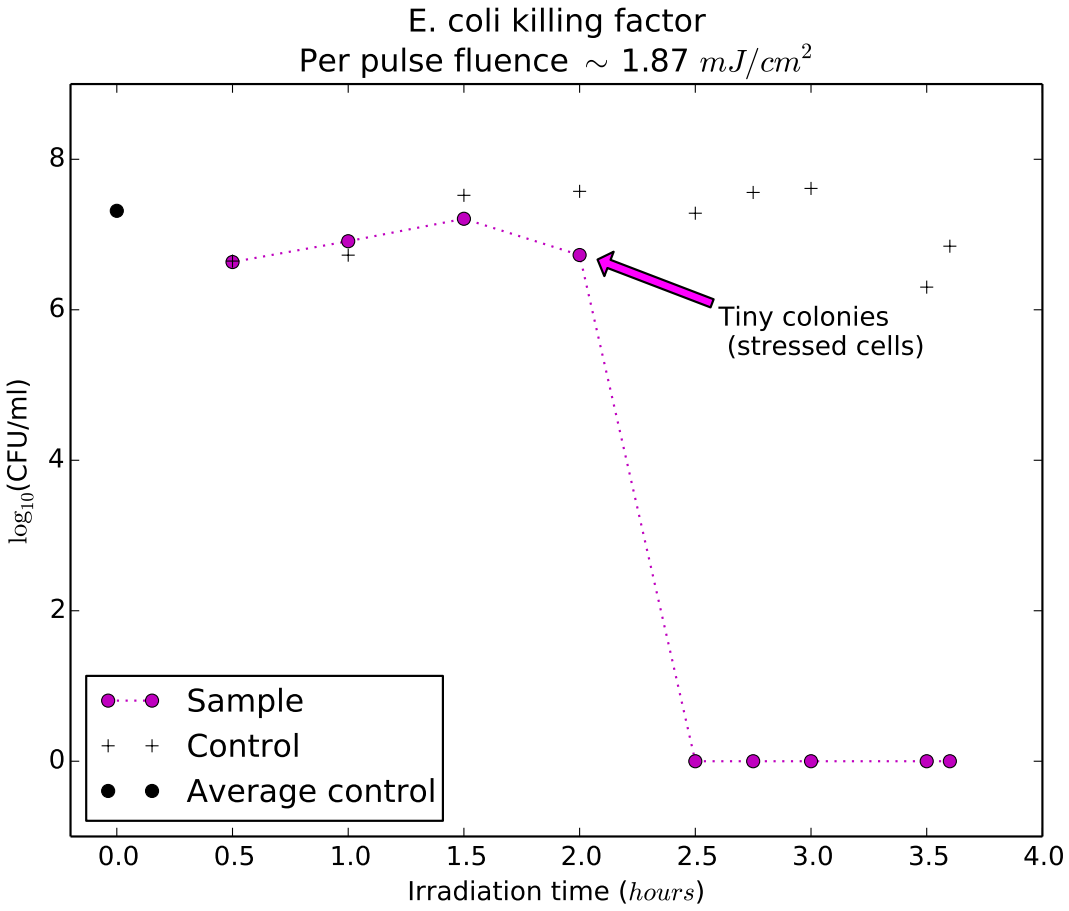

Figure 43**.** *E. coli* reduction in *CFU* as a function of irradiation time and constant fluence, corresponding to an average power of $350mW$. Colored dots indicate counted cells of samples irradiated different times; the plus signs are counted cells of their respective irradiation controls; and the black dot is the average of such controls.

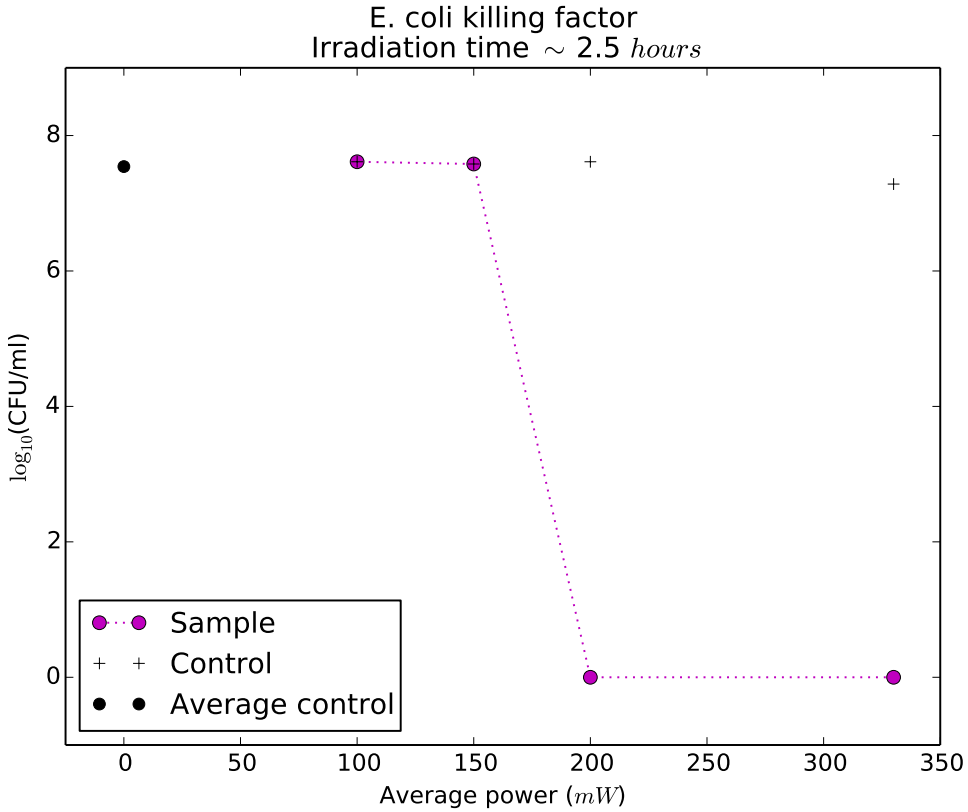

Figure 44**.** *E. coli* reduction in *CFU* as a function of average power and constant irradiation time. Colored dots indicate counted cells of samples irradiated different times; the plus signs are counted cells of their respective irradiation controls; and the black dot is the average of such controls.

In addition, macroscopic changes in colonies suggest that cells suffer from induced stress before being inactivated. Also, it is believe that the need of long treatment periods are related with the high cell population densities being used; this in view of the fact that inactivated cells have not been found without the use of a magnetic stirrer, which is added to the experiment to promote pulses-cells interactions.

Concerning the staining experiments, it can be said that although PI and AO are indicated to be combine with different type of cells, it was found that viable *E. coli* cells presented red fluorescence (PI) in the center and green (AO) in the outer zone (Figure 45(a)), making easy to identify intact cell membranes. Non-viable cells were mostly stained by PI, and AO was hardly integrated as shown in Figure 45(b); for this analysis, samples were fixed by heat (and therefore killed) on purposed to identify changes in the adhesion of the dyes.

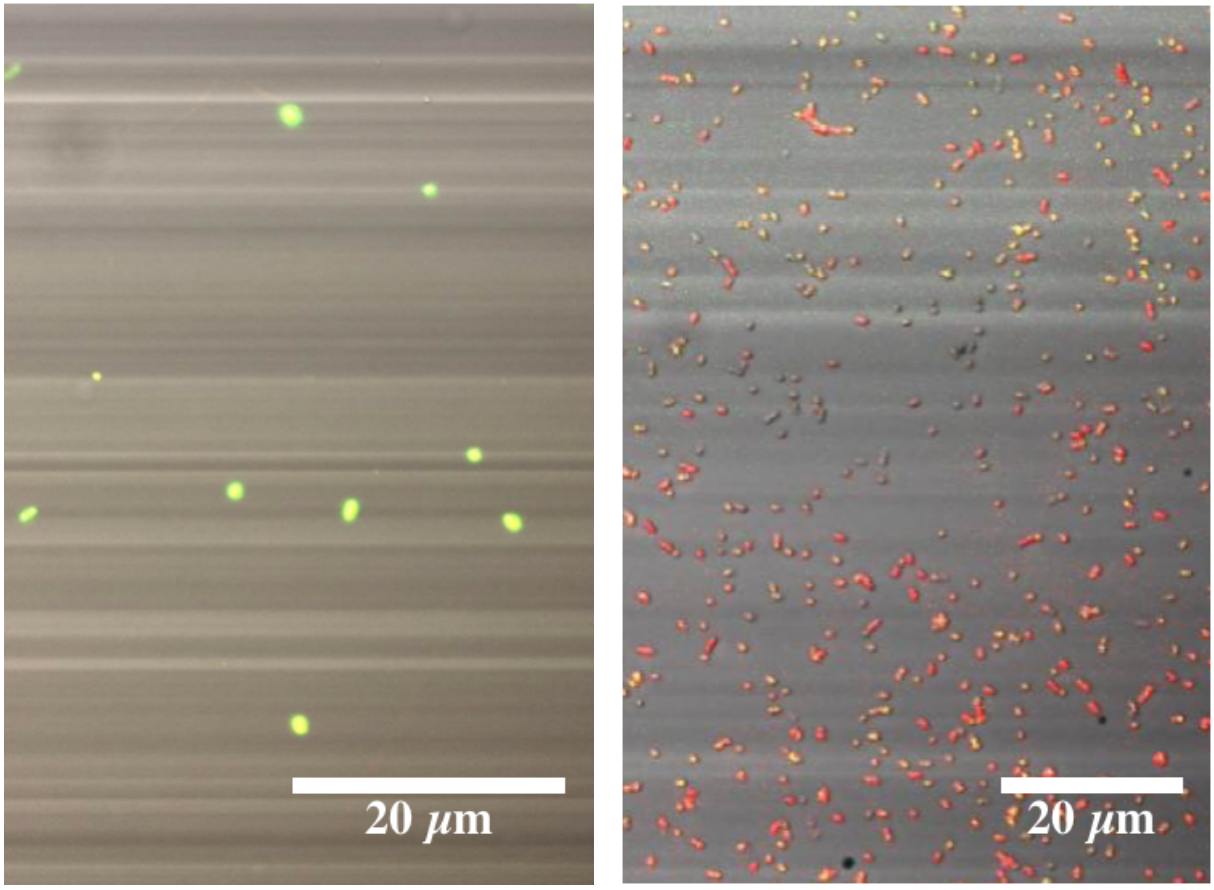

(a) Viable sample. (b) Negative control.

Figure 45. Acridine Orange and Propidium Iodide stained *E. coli*. Observation were made with fluorescence microscopy under 488*nm* and 532*nm* lights simultaneously.

For the purpose of these experiments, viable and non-viable terms are used to designate the capability and inability of cell division. In other words, a cell might be alive after being irradiated but with significant damage so it cannot replicate itself anymore. When this is the case, after 24*hours* of incubation, there are no living cells because those who were inoculated have already naturally died.

To compare these findings, the staining experiments were repeated but applied to an irradiated sample and its irradiation control. In this occasion, bacteria were observed using the confocal microscopy technique. Confocal microscopy was chosen because of its capability to observe multiple planes of a cell, which are then used for a three dimensional reconstruction. Moreover, this would enable identification of possible cell membrane damage.

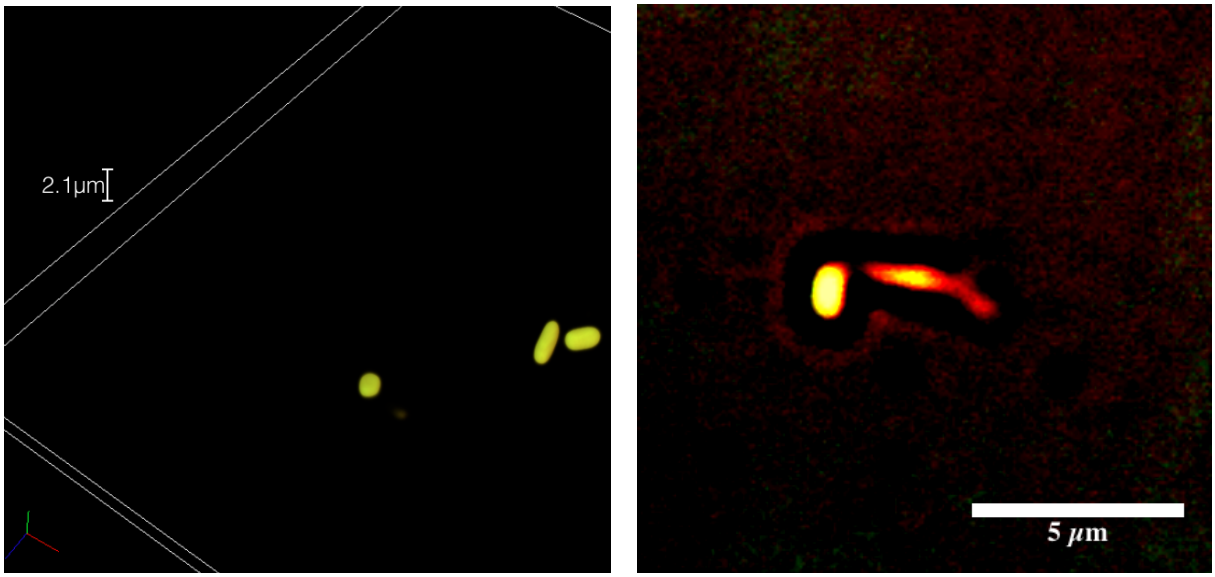

(a) Irradiation control. (b) Irradiated sample.

Figure 46. Acridine Orange and Propidium Iodide stained *E. coli*. Observations were made with fluorescence confocal microscopy.

Figure 46(a) portraits a group of the irradiation control bacteria. As illustrated before for viable cells, these are stained green in the outer region but a red center cannot be perceived. A contrasting result is that on Figure 46(b), where an irradiated *E. coli* cell looks green in the outer region but a red content appears to be leaving the cell structure. It is worth notice that the surrounding medium (distilled water) became noticeable red.

Analysis of both images advocates the conjecture that non-viable cells integrate PI. It is proposed the outer cell membrane can only integrate AO, impeding to see the red stained interior if the membrane is intact. On top of that, visible PI would indicate a damaged cell membrane that allows the interior flow out. This would also explain the surrounding medium change of color.

Unfortunately, when the sample and its irradiation control in Figure 46 were incubated to assess the laser-induced damage by cell counting, the results were inconclusive. Consequently, it cannot be assure they were viable and non-viable cells, respectively.

Chapter 4. Conclusions

Three methods for inscribing different configurations of waveguides in transparent nc-YSZ ceramics were demonstrated. The laser source was an Yb fiber laser (Satsuma HP2, Amplitude Systèmes) producing 270fs pulses at a central wavelength of 1030nm with variable repetition rate.

A different laser repetition rate regime was selected for each type of waveguide being written, showing different mechanisms of laser interaction can lead to waveguides fabrication. Per pulse energy, and processing optics were also carefully selected.

The present results indicate that waveguide propagation features are strongly dependent on inherent oxygen vacancies in the nc-YSZ ceramic and on the waveguides configurations.

4.1 Channel waveguides

An alternative method of inscribing Type II waveguides in such material, where samples are irradiated above the ablation threshold ($\sim 2.6\mu J$) to create two parallel channels of varying separation (15, 20, and 30μm). Optical characterization of the channel waveguides indicates that the waveguide propagation features are strongly dependent on several material and laser irradiation conditions such as inherent oxygen vacancies in the nc-YSZ and pulse repetition rate, respectively. The measured insertion losses indicate this type of waveguides are the most inefficient among the three configurations written in this work.

4.2 Planar waveguides

Two thermally resilient planar waveguides written by direct fs-laser inscription have been demonstrated in nc-YSZ ceramics with a simulated refractive index contrast of 10^{-4}. It was found that the waveguides can be excited to propagate in mono-mode or multi-mode for TE and TM polarized incident light at 633 and 810nm, but that the polarization of the guided light is not preserved. μ-Raman analysis of the waveguide and bulk material reveals that chemical phase changes are not induced during waveguide

fabrication. Finally, we conclude that planar waveguide structures in optical grade nc-YSZ posses a promising potential use in harsh and high temperature demanding photonic environments.

4.3 Depressed cladding waveguides

Depressed cladding waveguides written by direct *fs*-laser inscription have been demonstrated in nc-YSZ ceramics with a measured and simulated refractive index contrast of nearly 10^{-2}. The waveguides consist of two different structures and sizes, written also in two different samples. It was found that propagating modes are dependent on the cladding structure and waveguide diameter. A discrete cladding results in a striped pattern mode profile while a high-order mode propagation is preferred in the continuous scheme at $633nm$ and $1568nm$. In all cases the waveguiding is polarization independent due to the circular waveguide geometry and isotropic optical properties of nc-YSZ.

μ-Raman analysis of the waveguide core and laser processed cladding reveals that chemical phase changes are not induced during waveguide fabrication and indicates that the obtained index contrast is likely a result of a combination of induced residual stresses, microvoid/crack formation, and a decrease in crystallinity. Ultimately, it is concluded that continuous depressed cladding waveguide structures in optical grade nc-YSZ are a superior technology for unconventional/extreme environment applications such as biomedical photonics, where a combination of optical, chemical, mechanical, and biocompatible properties are required.

4.4 Bacterial inactivation

The methodology described in this work eliminates the requirement to supply cells with therapeutic agents while still achieving remarkable pathogen reduction. Total inactivation of distilled water and *E. coli* solutions with a density of $10^7 cell/mL$ was achieved with direct *fs*-laser irradiations using an average power of $350mW$ during $2.5hours$.

Fluorescence microscopy demonstrated to be a viable technique to identify the type of damage being caused to the cells by either individual high peak power density or by incubation effects due to the high repetition rate delivery of pulses.

4.5 Future work

4.5.1 Waveguide writing

Inscription of cladding waveguides in nc-YSZ ceramics of varying Y_2O_3 concentration, grain sizes, and annealing times to find the optimum parameters that reduce propagation losses.

Design and inscription of cladding waveguides in nc-YSZ ceramics with different configurations, such as helicoidal or curved cylinders.

4.5.2 Bacterial inactivation

Replication of bacterial inactivation experiments to retrieve more data. This will enable analysis of the possible non-linear phenomena induced by direct *fs*-laser irradiation that inactivates the cells.

Observation of *fs*-laser treated cells under fluorescence microscopy to identify the type of damage being caused.

Inactivation of different types of cells, specially those belonging to the Gram positive group. Treating cells with different morphology might also give an insight of the *fs*-laser induced type of damage to the cells.

Long term bacterial inactivation experiments. Culturing and monitoring treated cells for longer periods of time ($> 24 hours$) could lead to new findings regarding cellular response to *fs*-laser irradiation.

Direct *fs*-laser treatment on daily basis applied to the same group of cells. Repeating *fs*-laser treatment to non inactivated cells would improve the treatment success rate, possible to an extent of a few $\log_{10} CFU$ in cell reduction.

Chapter 5. Publications

Publications

- C. Guerra-Olvera, G. R. Castillo, E. H. Penilla, G. Uahengo, J. E. Garay, and S. Camacho-Lopez, “Circular Depressed Cladding Waveguides in Mechanically Robust, Biocompatible nc-YSZ Transparent Ceramics by fs Laser Pulses,” J. Light. Technol., vol. 37, no. 13, pp. 3119-3126, 2019.
- C. Guerra-Olvera, V. Pérez-Laguna, and S. Camacho-Lopez, “Direct fs-laser bacterial inactivation for a biomedical platform,” in Medical Laser Applications and Laser-Tissue Interactions VIII (2017), paper 104170I, 2017.
- C. Guerra-Olvera, G. R. Castillo, E. H. Penilla, G. Uahengo, Y. Esqueda-Baron, J. E. Garay, and S. Camacho-Lopez, “Thermally resilient planar waveguides in novel nc-YSZ transparent ceramic by *fs*-laser pulses”. **In progress.**

Presentations

- Escuela Latinoamericana de Óptica. Oral contribution: “Femtosecond laser inscription of waveguides in nanopolycrystalline ceramics”. October 2018, Gto., Mx.
- Congreso Regional de Óptica. Poster: “Femtosecond laser inscription of waveguides in nanopolycrystalline ceramics”. September 2018, B.C., Mx.
- IV Symposium of Nanoscience and Nanomaterials. Oral contribution: “Femtosecond laser inscription of waveguides in nanopolycrystalline ceramics”. April 2018, B.C., Mx.
- American Society for Laser Medicine and Surgery 2017. Poster: “Direct *fs*-laser bacterial inactivation”. April 2017, California, USA.
- Congreso Regional de Óptica. Poster: “Direct *fs*-laser bacterial inactivation”. September 2016, B.C., Mx.
- Congreso Regional de Óptica. Poster: “Windows to the Brain”. September 2015, B.C., Mx.

References

Alaniz, J. E., Perez-Gutierrez, F. G., Aguilar, G., and Garay, J. E. (2009). Optical properties of transparent nanocrystalline yttria stabilized zirconia. *Optical Materials*, **32**(1): 62–68.

Apostolopoulos, V., Laversenne, L., Colomb, T., Depeursinge, C., Salathé, R. P., Pollnau, M., Osellame, R., Cerullo, G., and Laporta, P. (2004). Femtosecond-irradiation-induced refractive-index changes and channel waveguiding in bulk Ti3+: Sapphire. *Applied Physics Letters*, **85**(7): 1122–1124.

Balzaretti, N. M. and da Jornada, J. A. H. (1995). Pressure dependence ofthe refractive index ofmonoclinic and yttria-stabilized cubic zirconia. *Physical Review B*, **52**(13): 9266–9269.

Benayas, A., Silva, W. F., Ródenas, A., Jacinto, C., Vázquez De Aldana, J., Chen, F., Tan, Y., Thomsom, R. R., Psaila, N. D., Reid, D. T., Torchia, G. A., Kar, A. K., and Jaque, D. (2011). Ultrafast laser writing of optical waveguides in ceramic Yb:YAG: A study of thermal and non-thermal regimes. *Applied Physics A: Materials Science and Processing*, **104**(1): 301–309.

Birks, T., Gris-Sánchez, I., Yerolatsitis, S., Leon-Saval, S. G., and Thomson, R. (2015). The photonic lantern. *Advances in Optics and Photonics*, **7**(2): 107–167.

Burghoff, J., Nolte, S., and Tünnermann, A. (2007). Origins of waveguiding in femtosecond laser-structured LiNbO3. *Applied Physics A*, **89**(1): 127–132.

Calmano, T., Paschke, A. G., Siebenmorgen, J., Fredrich-Thornton, S. T., Yagi, H., Petermann, K., and Huber, G. (2011). Characterization of an Yb:YAG ceramic waveguide laser, fabricated by the direct femtosecond-laser writing technique. *Applied Physics B: Lasers and Optics*, **103**(1): 1–4.

Casas, A., Di Venosa, G., Hasan, T., and Al Batlle (2011). Mechanisms of resistance to photodynamic therapy. *Current medicinal chemistry*, **18**(16): 2486–515.

Casolco, S. R., Xu, J., and Garay, J. E. (2008). Transparent/translucent polycrystalline nanostructured yttria stabilized zirconia with varying colors. *Scripta Materialia*, **58**(6): 516–519.

Castillo, G. R. (2017). *Ultrafast Laser Microprocessing of Transparent Dielectrics*. PhD thesis, Universidad de Salamanca.

Castillo, G. R., Labrador-Paez, L., Chen, F., Camacho-López, S., and De Aldana, J. (2017). Depressed-Cladding 3-D Waveguide Arrays Fabricated with Femtosecond Laser Pulses. *Journal of Lightwave Technology*, **35**(13): 2520–2525.

Castillo-Vega, G. R., Penilla, E. H., Camacho-López, S., Aguilar, G., and Garay, J. E. (2012). Waveguide-like structures written in transparent polycrystalline ceramics with an ultra-low fluence femtosecond laser. *Optical Materials Express*, **2**(10): 1416–1424.

Castillo-Vega, G. R., Romero, C., Lifante, G., Jaque, D., Chen, F., Varela, Ó., García-García, E., Méndez, C., Camacho-López, S., and Vázquez De Aldana, J. R. (2016). Stress-induced waveguides in Nd:YAG by simultaneous double-beam irradiation with femtosecond pulses. *Optical Materials*, **51**: 84–88.

Chartier, G. (2005). *Introduction to optics*. Springer. Grenoble, p. 595.

Chen, F. and de Aldana, J. R. (2014). Optical waveguides in crystalline dielectric materials produced by femtosecond-laser micromachining. *Laser and Photonics Reviews*, **8**(2): 251–275.

Damestani, Y., Reynolds, C. L., Szu, J., Hsu, M. S., Kodera, Y., Binder, D. K., Park, B. H., Garay, J. E., Rao, M. P., and Aguilar, G. (2013). Transparent nanocrystalline yttria-stabilized-zirconia calvarium prosthesis. *Nanomedicine: Nanotechnology, Biology, and Medicine*, **9**(8): 1135–1138.

Damestani, Y., Galan-Hoffman, D. E., Ortiz, D., Cabrales, P., and Aguilar, G. (2016). Inflammatory response to implantation of transparent nanocrystalline yttria-stabilized zirconia using a dorsal window chamber model. *Nanomedicine: Nanotechnology, Biology, and Medicine*, **12**(7): 1757–1763.

Davis, K. M., Miura, K., Sugimoto, N., and Hirao, K. (1996). Writing waveguides in glass with a femtosecond laser. *Optics Letters*, **21**(21): 1729.

Ding, L., Blackwell, R. I., Künzler, J. F., and Knox, W. H. (2008). Femtosecond laser micromachining of waveguides in silicone-based hydrogel polymers. *Applied Optics*, **47**(17): 3100.

Eaton, S., Zhang, H., Herman, P., Yoshino, F., Shah, L., Bovatsek, J., and Arai, A. (2005). Heat accumulation effects in femtosecond laser-written waveguides with variable repetition rate. *Optics express*, **13**(12): 4708–4716.

Eaton, S. M., Zhang, H., Ng, M. L., Li, J., Chen, W.-J., Ho, S., and Herman, P. R. (2008). Transition from thermal diffusion to heat accumulation in high repetition rate femtosecond laser writing of buried optical waveguides. *Optics Express*, **16**(13): 9443.

Fibich, G. and Gaeta, A. L. (2000). Critical power for self-focusing in bulk media and in hollow waveguides. *Optics Letters*, **25**(5): 335.

Flores-Romero, E., Vazquez, G. V., Marquez, H., Rangel-Rojo, R., Rickards, J., and Trejo-Luna, R. (2004). Planar waveguide lasers by proton implantation in Nd:YAG crystals. *Optics Express*, **12**(10): 2264.

Gattass, R. R. and Mazur, E. (2008). Femtosecond laser micromachining in transparent materials. *Nature Photonics*, **2**: 219.

Ghosh, S., Teweldebrhan, D., Morales, J. R., Garay, J. E., and Balandin, A. A. (2009). Thermal properties of the optically transparent pore-free nanostructured yttria-stabilized zirconia. *Journal of Applied Physics*, **106**(11): 113507.

Gorelik, T., Will, M., Nolte, S., Tuennermann, A., and Glatzel, U. (2003). Transmission electron microscopy studies of femtosecond laser induced modifications in quartz. *Applied Physics A: Materials Science and Processing*, **76**(3): 309–311.

Gross, S., Dubov, M., and Withford, M. J. (2015). On the use of the Type I and II scheme for classifying ultrafast laser direct-write photonics. *Optics Express*, **23**(6): 7767.

Gunter, P. (1978). *Metallographic etching*. American Society for Metals, first edition. p. 131.

Hardin, C. L., Kodera, Y., Basun, S. A., Evans, D. R., and Garay, J. E. (2013). Transparent, luminescent terbium doped zirconia: development of optical-structural ceramics with integrated temperature measurement functionalities. *Optical Materials Express*, **3**(6): 893.

He, R., An, Q., Jia, Y., Castillo-Vega, G. R., Vázquez de Aldana, J. R., and Chen, F. (2013a). Femtosecond laser micromachining of lithium niobate depressed cladding waveguides. *Optical Materials Express*, **3**(9): 1378.

He, R., An, Q., Vázquez de Aldana, J. R., Lu, Q., and Chen, F. (2013b). Femtosecond-laser micromachined optical waveguides in Bi 4 Ge 3 O 12 crystals. *Applied Optics*, **52**(16): 3713.

Hemberger, Y., Wichtner, N., Berthold, C., and Nickel, K. G. (2016). Quantification of yttria in stabilized zirconia by Raman spectroscopy. *International Journal of Applied Ceramic Technology*, **13**(1): 116–124.

Hench, L. L. (2013). *An Introduction to Bioceramics*. IMPERIAL COLLEGE PRESS, second edition. p. 620.

Hernández-Cordero, J., Ramos-García, R., Camacho-López, S., and Aguilar, G. (2018). A New Window for Photonics in the Brain. *IEEE Photonics Society Newsletter*, **32**(1): 4–8.

Ingel, R. P. and Lewis III, D. (1986). Lattice Parameters and Density for Y2O3-Stabilized ZrO2. *Journal of the American Ceramic Society*, **69**(4): 325–332.

Jenkins, M. H., Phillips, B. S., Zhao, Y., Holmes, M. R., Schmidt, H., and Hawkins, A. R. (2011). Optical Characterization of Optofluidic Waveguides Using Scattered Light Imaging. *Optical Communications*, **284**(16-17): 3980–3982.

Jia, Y., Chen, F., Vázquez de Aldana, J. R., Akhmadaliev, S., and Zhou, S. (2012). Femtosecond laser micromachining of Nd:GdCOB ridge waveguides for second harmonic generation. *Optical Materials*, **34**(11): 1913–1916.

Johnston, H. J., Hutchison, G., Christensen, F. M., Peters, S., Hankin, S., and Stone, V. (2010). A review of the in vivo and in vitro toxicity of silver and gold particulates: Particle attributes and biological mechanisms responsible for the observed toxicity. *Critical Reviews in Toxicology*, **40**(4): 328–346.

Kim, S., Kim, J., Lim, W., Jeon, S., Kim, O., Koh, J.-T., Kim, C.-S., Choi, H., and Kim, O. (2013). In vitro bactericidal effects of 625, 525, and 425 nm wavelength (red, green, and blue) light-emitting diode irradiation. *Photomedicine and laser surgery*, **31**(11): 554–562.

Kröger, F. A. and Vink, H. J. (1958). Relations between the concentrations of imperfections in solids. *Journal of Physics and Chemistry of Solids*, **5**(3): 307–435.

Lach, R., Gyeong-Man, K., Hannes-Michker, W., Grellmann, W., and Albrecht, K. (2006). ndentation fracture mechanics for toughness assessment of PMMA/SiO2 nanocomposites. *Macromolecular Materials and Engineering*, **291**(3): 263–271.

Li, L., Nie, W., Li, Z., Lu, Q., Romero, C., Vázquez de Aldana, J. R., and Chen, F. (2017). All-laser-micromachining of ridge waveguides in LiNbO3 crystal for mid-infrared band applications. *Scientific Reports*, **7**(1): 7034.

Liu, H., Jia, Y., Vázquez de Aldana, J. R., Jaque, D., and Chen, F. (2012). Femtosecond laser inscribed cladding waveguides in Nd:YAG ceramics: fabrication, fluorescence imaging and laser performance. *Optics Express*, **20**(17): 18620–18629.

Macdonald, J. R., Thomson, R. R., Beecher, S. J., Psaila, N. D., Bookey, H. T., and Kar, A. K. (2010). Ultrafast laser inscription of near-infrared waveguides in polycrystalline ZnSe. *Optics Letters*, **35**(23): 4036.

Martínez De Mendívil, J., Sola, D., Vázquez De Aldana, J. R., Lifante, G., De Aza, A. H., Pena, P., and Peña, J. I. (2015). Ultrafast direct laser writing of cladding waveguides in the 0.8CaSiO3-0.2Ca3(PO4)2 eutectic glass doped with Nd3+ ions. *Journal of Applied Physics*, **117**(4).

Nejadmalayeri, A. H. and Herman, P. R. (2007). Rapid thermal annealing in high repetition rate ultrafast laser waveguide writing in lithium niobate. *Optics Express*, **15**(17): 10842.

Nguyen, H.-D., Ródenas, A., Vázquez de Aldana, J. R., Martín, G., Martínez, J., Aguiló, M., Cinta Pujol, M., and DÍaz, F. (2017). Low-loss 3D-laser-written mid-infrared LiNbO3 depressed-index cladding waveguides for both TE and TM polarizations. *Optics Express*, **25**(4): 3722–3736.

Nussbaum, E. L., Lilge, L., and Mazzulli, T. (2003). Effects of low-level laser therapy (LLLT) of 810 nm upon in vitro growth of bacteria: relevance of irradiance and radiant exposure. *Journal of clinical laser medicine & surgery*, **21**(5): 283–290.

Okamoto, K. (2010). *Fundamentals of Optical Waveguides*. Elsevier Science.

Okhrimchuk, A. G., Shestakov, A. V., Khrushchev, I., and Mitchell, J. (2005). Depressed cladding, buried waveguide laser formed in a YAG:Nd3+ crystal by femtosecond laser writing. *Optics Letters*, **30**(17): 2248–2250.

Osellame, R., Cerullo, G., and Ramponi, R. (2012). *Femtosecond Laser Micromachining*. Springer-Verlag Berlin Heidelberg, first edition. p. 486.

Paschotta, R. (2008). *Field Guide to Lasers*. SPIE Press. Bellingham, WA, p. 152.

Peng, Y. P., Zou, X., Bai, Z., Leng, Y., Jiang, B., Jiang, X., and Zhang, L. (2015). Mid-infrared laser emission from Cr:ZnS channel waveguide fabricated by femtosecond laser helical writing. *Scientific Reports*, **5**(November): 1–6.

Piromjitpong, T., Dubov, M., and Boscolo, S. (2019). High-repetition-rate femtosecond-laser inscription of low-loss thermally stable waveguides in lithium niobate. *Applied Physics A*, **125**(5): 302.

Quigley, T. (2008). Monitoring the Growth of E. coli With Light Scattering. Technical report, BioTek Instruments, Inc., Vermont, USA.

Ramachandran, S., Nicholson, J. W., Ghalmi, S., Yan, M. F., Wisk, P., Monberg, E., and Dimarcello, F. V. (2006). Light propagation with ultralarge modal areas in optical fibers. *Optics Letters*, **31**(12): 1797.

Rangel, J. M., Sparling, P. H., Crowe, C., Griffin, P. M., and Swerdlow, D. L. (2005). Epidemiology of Escherichia coli O157:H7 outbreaks, United States, 1982-2002. *Emerging Infectious Diseases*, **11**(4): 603–609.

Righini, G. C. and Chiappini, A. (2014). Glass optical waveguides: a review of fabrication techniques. *Optical Engineering*, **53**: 1–15.

Ródenas, A., Torchia, G. A., Lifante, G., Cantelar, E., Lamela, J., Jaque, F., Roso, L., and Jaque, D. (2009). Refractive index change mechanisms in femtosecond laser written ceramic Nd:YAG waveguides: Micro-spectroscopy experiments and beam propagation calculations. *Applied Physics B: Lasers and Optics*, **95**(1): 85–96.

Saha, N. and Kumar, A. (2018). Highly sensitive temperature sensor based on a long period waveguide grating with polymer upper cladding and metal under cladding. In: *CLEO Pacific Rim Conference 2018*. Optical Society of America, p. Th1L.5.

Salamu, G., Jipa, F., Zamfirescu, M., and Pavel, N. (2014a). Cladding waveguides realized in Nd:YAG ceramic by direct femtosecond-laser writing with a helical movement technique. *Optical Materials Express*, **4**(4): 790–797.

Salamu, G., Voicu, F., Jipa, F., Zamfirescu, M., Dascalu, T., and Pavel, N. (2014b). Laser emission from diode-pumped Nd:YAG cladding waveguides obtained by direct writing with a femtosecond-laser beam. *Laser Sources and Application II*, **9135**(5): 91351F.

Saleh, B. E. A. and Teich, M. C. (1991). *Fundamentals of Photonics*. John Wiley & Sons, Inc., first edition. pp. 0–471.

Schaffer, C. B., Brodeur, A., and Mazur, E. (2001). Laser-induced breakdown and damage in bulk transparent materials induced by tightly focused femtosecond laser pulses. *Measurement Science and Technology*, **12**(11): 1784–1794.

Sennhenn-Kirchner, S., Klaue, S., Wolff, N., Mergeryan, H., Borg von Zepelin, M., and Jacobs, H. G. (2007). Decontamination of rough titanium surfaces with diode lasers: microbiological findings on in vivo grown biofilms. *Clinical oral implants research*, **18**(1): 126–132.

Shane, E. M., De Marco, C., Martinez-Vazquez, R., Ramponi, R., Turri, S., Cerullo, G., and Osellame, R. (2012). Femtosecond laser microstructuring for polymeric lab-on-chips. *Journal of Biophotonics*, **5**(8-9): 687–702.

Siebenmorgen, J., Petermann, K., Huber, G., Rademaker, K., Nolte, S., and Tünnermann, A. (2009). Femtosecond laser written stress-induced Nd:Y3Al5O12 (Nd:YAG) channel waveguide laser. *Applied Physics B*, **97**(2): 251–255.

Silva, W. F., Jacinto, C., Benayas, A., Vazquez de Aldana, J. R., Torchia, G. A., Chen, F., Tan, Y., and Jaque, D. (2010). Femtosecond-laser-written, stress-induced Nd:YVO_4 waveguides preserving fluorescence and Raman gain. *Optics Letters*, **35**(7): 916.

Spetzger, U., Vougioukas, V., and Schipper, J. (2010). Materials and techniques for osseous skull reconstruction. *Minimally Invasive Therapy & Allied Technologies*, **19**(2): 110–121.

Stoian, R., D'Amico, C., Bhuyan, M. K., and Cheng, G. (2016). Ultrafast laser photoinscription of large-mode-area waveguiding structures in bulk dielectrics. *Optics and Laser Technology*, **80**: 98–103.

Teigell Benéitez, N., Missinne, J., Shi, Y., Chiesura, G., Luyckx, G., Degrieck, J., and Van Steenberge, G. (2016). Highly Sensitive Waveguide Bragg Grating Temperature Sensor Using Hybrid Polymers. *Photonics Technology Letters*, **28**(10): 1150–1153.

Ter Gabrielyan, N., Merkle, L. D., Ikesue, A., and Dubinskii, M. (2008). Ultralow quantum-defect eye-safe er:sc2o3 laser. *Opt. Lett.*, **33**(13): 1524–1526.

Thomson, R. R., Campbell, S., Blewett, I. J., Kar, A. K., and Reid, D. T. (2006). Optical waveguide fabrication in z-cut lithium niobate (LiNbO3) using femtosecond pulses in the low repetition rate regime. *Applied Physics Letters*, **88**(11): 1–4.

Torchia, G. A., Ródenas, A., Benayas, A., Cantelar, E., Roso, L., and Jaque, D. (2008). Highly efficient laser action in femtosecond-written Nd:yttrium aluminum garnet ceramic waveguides. *Applied Physics Letters*, **92**(11): 140–142.

Tsen, K. T., Tsen, S. W. D., Sankey, O. F., and Kiang, J. G. (2007). Selective inactivation of micro-organisms with near-infrared femtosecond laser pulses. *Journal of Physics Condensed Matter*, **19**(47): 1–7.

Tuller, H. L. (2000). Ionic conduction in nanocrystalline materials. *Solid State Ionics*, **131**(1): 143 – 157.

Wang, F., Liu, F., Chang, G.-K., and Adibi, A. (2008). Precision measurements for propagation properties of high-definition polymer waveguides by imaging of scattered light. *Optical Engineering*, **47**(2): 024602.

Zambrano, D., Barrios, A., Tobón, L., Serna, C., Gómez, P., Osorio, J., and Toro, A. (2018). Thermal properties and phase stability of yttria-stabilized zirconia (ysz) coating deposited by air plasma spray onto a ni-base superalloy. *Ceramics International*, **44**(4): 3625 – 3635.

Zhang, C., Dong, N., Yang, J., Chen, F., Vázquez de Aldana, J. R., and Lu, Q. (2011). Channel waveguide lasers in Nd:GGG crystals fabricated by femtosecond laser inscription. *Optics Express*, **19**(13): 12503–12508.

Zipperian, D. C. (2011). *Metallographic Handbook*. PACE Technologies, first edition. Tucson, AZ, p. 342.

Zwietering, M. H., Jongenburger, I., Rombouts, F. M., and van 't Riet, K. (1990). Modeling of the Bacterial Growth Curve. *Applied and Environmental Microbiology*, **56**(6): 1875 LP – 1881.

Appendix

A YSZ properties

Table 11. YSZ properties dependending on the degree of stabilizing dopant Y_2O_3.

Y_2O_3%	Phase	Type	Stability	Raman band[Hemberger *et al.* (2016)]
0%	single	monoclinic tetragonal cubic	room temperature $> 1100°C$ $> 2400°C$	$643.05cm^{-1}$
3%	single	tetragonal	PSZ	$643.03cm^{-1}$
6%	double	tetragonal cubic	PSZ	$642.42cm^{-1}$
8%	single	cubic	FSZ	$640.50cm^{-1}$

B Waveguide writing parameters

For the inscription of each type of waveguide configuration, a series of *fs*-laser parameters were carefully selected. These are listed in Table 12 and were chosen after several experiments on the nc-YSZ that allowed convergence of each parameter to find the optimum values for each type of waveguide been written.

Table 12. Direct *fs*-laser waveguide inscription parameters for different types of waveguides in nc-YSZ.

	Cladding	Channel	Planar
Repetition rate [kHz]	1	500	1000
Average power [mW]	3	1300	2000
Processing optics	50X objective	$f = 4mm$ lens	$f = 4mm$ lens
Beam FWHM [μm]	2	3.8	3.8
Energy [μJ]	3	2.6	2
Fluence [J/cm^2]	33	5.17	3.97
Interaction	lattice expansion	ablation	oxygenation

C Staining protocol

Acridine Orange (AO) and Propidium Iodide (PI) are standard reagents used for assessing cell viability. Both can be found commercially in solution format but if they are solids, a liquid stain ready to use can be easily prepared adding $10\mu g$ of the reagent for every $1ml$ of phosphate-buffered saline (PBS). Always store frozen and in the dark.

The following protocol will stain red (due to PI) with green traces (due to AO) all dead *E. coli* cells, whilst viable cells appear red in the center and green all over, producing the effect of yellow center with a green surrounding.

1. Prepare a bacterial solution (cells in distilled water) at $OD600 \sim 4.0$ as indicated in Section 2.6.1.
   (a) For the negative control: Put $\sim 37.5\mu l$ of the solution on a glass slit and heat it dry. This can be done using a Bunsen burner. Only a couple of heat exposure seconds are needed to kill bacteria.
   (b) For the sample: Dilute $\sim 37.5\mu l$ of the solution with $7.5\mu l$ of distilled water and put it on a glass slit.
2. Add $30\mu l$ of AO and $30\mu l$ of PI to the glass slit.
3. Vortex at moderate speed to avoid cell damage.
4. Incubate the slit for $15-30minutes$ at $37°C$.
5. Optionally, wash out the dyes on the control with distilled water and let naturally dry.
6. Cover up the slit with a glass cover slit and observe under $488nm$ and $532nm$ lights simultaneously.